Synthesis of metal-zeolite composite materials for bifunctional catalytic reactions

Débora Regina Strossi Pedrolo

Thesis for obtaining
a title of Doctor of Chemical Engineering of Federal University of Rio Grande do Sul
a title of Doctor of Université de Lille

Specialty:
Organic, Mineral and Industrial Chemistry
Molecules and Condensed Matter

SYNTHESIS OF METAL-ZEOLITE COMPOSITE MATERIALS FOR BIFUNCTIONAL CATALYTIC REACTIONS

Débora Regina Strossi Pedrolo

The PhD thesis defense took place on December 14th, 2021 in UFRGS, Porto Alegre, Brazil

Composition of the Jury:

Jury President	Prof. Juliana da Silveira Espindola, FURG (Brazil)
Reviewers	Prof. Juliana da Silveira Espindola, FURG (Brazil)
	Prof. Svetlana Mintova, ENSICAEN (France)
Thesis Directors	Prof. Vitaly Ordomsky, Université de Lille (France)
	Prof. Nilson Romeu Marcilio, UFRGS (Brazil)
Examiners	Prof. Andrei Khodakov, Université de Lille (France)
	Prof. Marcio Schwaab, UFRGS (Brazil)
	Prof. Ovidiu Ersen, Université de Strasbourg (France)

Thèse pour l'obtention d'un titre de Docteur en Génie Chimique de l'Université Fédérale de Rio Grande do Sul
un titre de Docteur de l'Université de Lille

Spécialité:
Chimie Organique, Minérale et Industrielle
Molécules et Matière Condensée

SYNTHESE DE MATERIAUX COMPOSITES METAL-ZEOLITE POUR DES REACTIONS CATALYTIQUES BIFONCTIONNELLES

Débora Regina Strossi Pedrolo

La soutenance de thèse a eu lieu le 14 décembre 2021 à l'UFRGS, Porto Alegre, Brésil

Composition du Jury:

President du Jury	Prof. Juliana da Silveira Espindola, FURG (Brazil)
Rapporteurs	Prof. Juliana da Silveira Espindola, FURG (Brazil)
	Prof. Svetlana Mintova, ENSICAEN (France)
Directeurs de Thèse	Prof. Vitaly Ordomsky, Université de Lille (France)
	Prof. Nilson Romeu Marcilio, UFRGS (Brazil)
Examiners	Prof. Andrei Khodakov, Université de Lille (France)
	Prof. Marcio Schwaab, UFRGS (Brazil)
	Prof. Ovidiu Ersen, Université de Strasbourg (France)

CONTENTS

Acknowledgments

I am gratefully thankful to my supervisors, Dr. Nilson Romeu Marcílio, Dr. Vitaly Ordomsky, and Dr. Marcio Schwaab, and the contributor Dr. Andrei Khodakov, for the guidance and support.

I thank to Dr. Valentin Valtchev, Dr. Jan Přech for the kind suggestions and guidance. Dr. Bang Gu, Dr. Deizi Peron and Dr. Camila Flores for their great contributions in the development of this research. I would like to thank the colleagues and friends I met in the group membership in France, UCCS, LPR, UFRGS and Lille University.

I would also like to thank the jury members of my thesis, Dr. Juliana Espindola and Dr. Svetlana Mintova for the reading and the examination of this manuscript.

To CAPES, and CAPES/Cofecub for their financial support and ANR project DIRECTSYNBIOFUEL.

To the Postgraduate Program in Chemical Engineering from UFRGS.

To the members of the jury for accepting to contribute, review, and examination of this Thesis.

Finally, I would like to thank my family for their care, understanding and unconditional love.

Abstract

Bifunctional zeolite-metal catalysts have been widely used in modern chemistry. The existing conventional preparation procedure such as impregnation usually leads to the deposition of large metal particles on the external surface of zeolite due to the small size of the pores in zeolites. It results in the low contact between metal and acid sites in the catalyst and low yields of the target products.

The purpose of this PhD Thesis was elaboration of new strategies for the design of metal-zeolite nanocomposite catalysts containing ruthenium nanoparticles uniformly distributed in the hierarchical BEA and ZSM-5 zeolites. The new route for the synthesis of Ru-zeolite composite material has been proposed in Chapter 3 by using carbon nanotubes with supported metal oxide nanoparticles playing a role of sacrificial template, which allows creating mesoporosity and bringing metallic functionality inside the zeolite matrix. Compared to the conventional zeolite-supported metal catalysts, the synthesized hierarchical ruthenium-zeolites exhibited much higher activity and lower methane selectivity in Fischer-Tropsch synthesis.

In Chapter 4, a new synthetic strategy was developed for the preparation of hierarchical metal-zeolite nanocomposite catalysts for the direct synthesis of iso-paraffins from syngas. The nanocomposites are synthesized in three steps. In the first step, the parent (core) zeolite is etched with an ammonium fluoride solution. The etching creates small mesopores inside the zeolite crystals. In the second step, the Ru nanoparticles prepared using water-in-oil microemulsion are deposited in the mesopores of the zeolite. In the third step, a zeolite shell of MFI-type zeolites (silicalite-1 or ZSM-5) is grown on the parent zeolite crystals coating both the etched surface and metallic nanoparticles. Thus, the metal

nanoparticles become entirely encapsulated inside the zeolite matrix. Most important parameters such as ruthenium content, zeolite mesoporosity, and more particularly, the acidity of the catalyst shell, which affect the catalytic performance of the synthesized nanocomposite materials in low-temperature Fischer−Tropsch synthesis were identified in this work. A higher relative amount of iso-paraffins was observed on the catalysts containing a shell of ZSM-5. The proximity between metal and acid sites in the zeolite shell of the nanocomposite catalysts is a crucial parameter for the design of efficient metal zeolite bifunctional catalysts for selective synthesis of gasoline-type fuels via Fischer−Tropsch synthesis, while the acidity of the catalyst core has only a limited impact on the catalytic performance.

Additionally, we have discovered that the growth of the new layer of zeolite on the surface of Ru nanoparticles leads to their decomposition with an increase in the dispersion of the metal.

Keywords: hierarchical zeolites, ruthenium, Fischer-Tropsch synthesis, nanoparticles, bifunctional catalyst.

Résumé

Les catalyseurs bifonctionnels zéolite-métal sont largement utilisés dans la chimie moderne. La procédure de préparation conventionnelle existante telle que l'imprégnation conduit généralement au dépôt des grosses particules métalliques à la surface externe de la zéolithe en raison d'une petite taille des pores dans les zéolithes. Il en résulte en un faible contact entre les sites métalliques et acides dans le catalyseur et de faibles rendements en produits cibles.

Le but de cette thèse était l'élaboration des nouvelles stratégies pour la conception de catalyseurs nanocomposites métal-zéolithe qui contiennent des nanoparticules de ruthénium uniformément réparties dans les zéolithes hiérarchisées BEA et ZSM-5. Une nouvelle voie de synthèse du matériau composite Ru-zéolithe a été proposée dans le chapitre 3 en utilisant des nanotubes de carbone avec des nanoparticules d'oxyde métallique supportées jouant un rôle de matrice sacrificielle, ce qui permet de créer une mésoporosité et d'apporter une fonctionnalité métallique à l'intérieur de la matrice zéolithique. Par rapport aux catalyseurs métalliques conventionnels supportés par de la zéolithe, les zéolithes ruthénium hiérarchisées synthétisées présentaient une activité beaucoup plus élevée et une sélectivité en méthane plus faible dans la synthèse Fischer-Tropsch.

Dans le chapitre 4, une stratégie de synthèse a été développée pour la préparation de catalyseurs nanocomposites métal-zéolithe hiérarchisés pour la synthèse directe d'iso-paraffines à partir du gaz de synthèse. Les nanocomposites sont synthétisés en trois étapes. Dans la première étape, la zéolithe mère (noyau) est gravée avec une solution de fluorure d'ammonium. La gravure crée de petits mésopores à l'intérieur des cristaux de zéolithe. Dans la deuxième étape, les nanoparticules de Ru préparées à l'aide de microémulsion eau-dans-

huile sont déposées dans les mésopores de la zéolithe. Dans la troisième étape, une enveloppe de zéolithe de type MFI (silicalite-1 ou ZSM-5) est cultivée sur les cristaux de zéolithe parent recouvrant à la fois la surface gravée et les nanoparticules métalliques. Ainsi, les nanoparticules métalliques deviennent entièrement encapsulées à l'intérieur de la matrice zéolithique. Les paramètres les plus importants tels que la teneur en ruthénium, la mésoporosité de zéolithe, et plus particulièrement, l'acidité de l'enveloppe du catalyseur, qui affectent les performances catalytiques des matériaux nanocomposites synthétisés dans la synthèse Fischer-Tropsch à basse température ont été identifiés dans ce travail. Une quantité relative plus élevée d'iso-paraffines a été observée sur les catalyseurs contenant une enveloppe de ZSM-5. La proximité entre les sites métalliques et acides dans l'enveloppe zéolithique des catalyseurs nanocomposites est un paramètre crucial pour la conception de catalyseurs bifonctionnels zéolithiques métalliques efficaces pour la synthèse sélective de carburants de type essence via la synthèse Fischer-Tropsch, tandis que l'acidité du cœur du catalyseur n'a qu'un impact limité sur les performances catalytiques.

De plus, nous avons découvert que la croissance d'une nouvelle couche de zéolithe à la surface des nanoparticules de Ru conduit à leur décomposition avec une augmentation de dispersion du métal.

Mots-clés: zéolithes hiérarchisées, ruthénium, synthèse Fischer-Tropsch, nanoparticules, catalyseur bifonctionnel.

Resumo

Catalisadores bifuncionais zeólita-metal têm sido amplamente utilizados na química moderna. O procedimento de preparação convencional existente, como a impregnação, geralmente leva à deposição de grandes partículas metálicas na superfície externa da zeólita devido ao pequeno tamanho dos poros das zeólitas. Isso resulta no baixo contato entre os sítios metálicos e ácidos no catalisador e baixos rendimentos dos produtos desejados.

O objetivo desta Tese de Doutorado foi a elaboração de novas estratégias para o projeto de catalisadores nanocompostos metal-zeólita contendo nanopartículas de rutênio uniformemente distribuídas nas zeólitas hierárquicas BEA e ZSM-5. A nova rota para a síntese do material Ru-zeólita foi proposta no Capítulo 3 usando nanotubos de carbono com nanopartículas de óxido metálico suportadas, desempenhando um papel de template de sacrifício, o que permite criar mesoporosidade e trazer a funcionalidade metálica para dentro da matriz zeolítica. Em comparação com os catalisadores metálicos convencionais suportados por zeólitas, as zeólitas de rutênio hierárquicas sintetizadas exibiram atividade muito mais alta e menor seletividade de metano na síntese de Fischer-Tropsch.

No Capítulo 4, uma nova estratégia sintética foi desenvolvida para a preparação de catalisadores nanocompostos metal-zeólita hierárquicas para a síntese direta de isoparafinas a partir de syngas. Os nanocompostos são sintetizados em três etapas. Na primeira etapa, a zeólita pai (núcleo) é inserida em uma solução de fluoreto de amônio. A inserção cria pequenos mesoporos dentro dos cristais da zeólita. Na segunda etapa, as nanopartículas de Ru preparadas em microemulsão água-em-óleo são depositadas nos mesoporos da zeólita. Na terceira etapa, uma solução de zeólita do tipo MFI (silicalita-1 ou ZSM-5) é inserida nos cristais da zeólita pai que revestem os mesoporos criados pelo fluoreto de amônio e as

nanopartículas metálicas. Assim, as nanopartículas metálicas ficam totalmente encapsuladas dentro da matriz zeolítica. Parâmetros importantes como teor de rutênio, mesoporosidade da zeólita e, mais particularmente, a acidez do catalisador, que afetam o desempenho catalítico dos materiais nanocompostos sintetizados na síntese de Fischer-Tropsch em baixa temperatura foram identificados neste trabalho. Uma maior quantidade relativa de isoparafinas foi observada nos catalisadores contendo o revestimento de ZSM-5. A proximidade entre os sítios metálicos e ácidos no revestimento da zeólita dos catalisadores nanocompostos é um parâmetro crucial para o projeto de catalisadores bifuncionais de zeólitas metálicas eficientes para síntese seletiva de combustíveis do tipo gasolina via síntese de Fischer-Tropsch, enquanto a acidez do núcleo do catalisador tem apenas um impacto limitado no desempenho catalítico.

Além disso, descobrimos que o crescimento de uma nova camada de zeólita na superfície das nanopartículas de Ru leva à sua decomposição com o aumento da dispersão do metal.

Palavras-chave: zeólita hierárquicas, rutênio, síntese de Fischer-Tropch, nanopartículas, catalisadores bifuncionais.

Chapter 1. Literature Review

1.1 Zeolites: Structure and properties

Zeolites are microporous materials formed by AlO_4 and SiO_4 tetrahedra linked via their edges with regular pores and cavities of molecular dimensions (3-15 Å). Zeolites have important properties such as:

1. strong acidic sites,
2. large specific surface area,
3. high ion-exchange ability,
4. high thermal stability and
5. well defined system of micropores for shape-selective catalytic reactions,

making them unique for catalytic applications [1], [2].

Several mesoporous molecular sieves with adjustable pore sizes have been developed, presenting potential use in catalytic reactions. The accessibility of the active sites and the molecular traffic within the zeolite can be controlled by varying the size of pores and the number of different openings through which molecules can circulate. These physicochemical properties together with their high hydrothermal stability have allowed their wide application in the industry [2].

Replacing a Si^{+4} atom with an Al^{+3} atom causes an electronic imbalance in the structure, leaving it negatively charged. Thus, it is necessary for the presence of extra-structural compensation cations (usually Na^+, K^+ and Ca_2^+) that create a positive charge to neutralize the negative charge created by the substitution of each Al atom (Figure 1.1) [3], [4].

Figure 1.1. Ion exchange property of the zeolitic structure.

The unit cell of the zeolites can be represented by the formula below:

$$\left[M_{\frac{x}{y}}^{n+}(SiO_2)_y(AlO_2^-)_x\right].wH_2O$$

where M is the compensation cation (alkali metal or alkaline earth metal) with charge *n*, *x*+*y* is the number of tetrahedra per unit cell and *w* is the number of water molecules per unit cell. The *y*/*x* ratio is the Si/Al ratio. This ratio determines the acidity and the ion-exchange capacity since the extra framework cations are ion exchangeable.

The amount of Al within the framework can vary in a wide range (Si/Al = 1 to ∞) [3]. As the Si/Al ratio increases, the hydrothermal stability and hydrophobicity increase [5], [6]. Zeolites are usually classified into three classes:

1. Low Si/Al ratios (<5).
2. Medium Si/Al ratios (5 to 10).
3. High Si/Al ratios (>10).

Normally, zeolites are synthesized under hydrothermal conditions (100 °C to 200 °C) with synthesis gel containing framework atoms, solvents, templates or structural directing agents (SDAs), and mineralizers [7]. Water is generally used as a solvent. The mineralizer is used to increase the solubility of the silicate or aluminosilicate species using dissolution and precipitation. The OH^- is the most used mineralizing agent for the synthesis of zeolites [3].

The role of SDAs is the encapsulation within the microporous structure to provide pore structure architecture and stabilize the system by weak electrostatic interaction between the framework and the occluded organic species [8]. Depending on the experimental conditions, some organic molecules can lead to different zeolite structures [9]. When an organic structure-directing agent (OSDA), such as amine or quaternary ammonium salt, is introduced in the synthesis gel, the Si/Al ratio increases due to bulky organic molecules that occupy the zeolite channels volume providing less positive charges in the final solid, and therefore, fewer aluminum atoms in the framework are required [3].

Beta and ZSM-5 zeolites are well known aluminosilicates. Beta is formed by a three-dimensional large pore system (openings of 6.5-7 Å), and ZSM-5 is formed by a three-dimensional medium pore system (openings of 5-5.5 Å) (Figure 1.2) [10], [11].

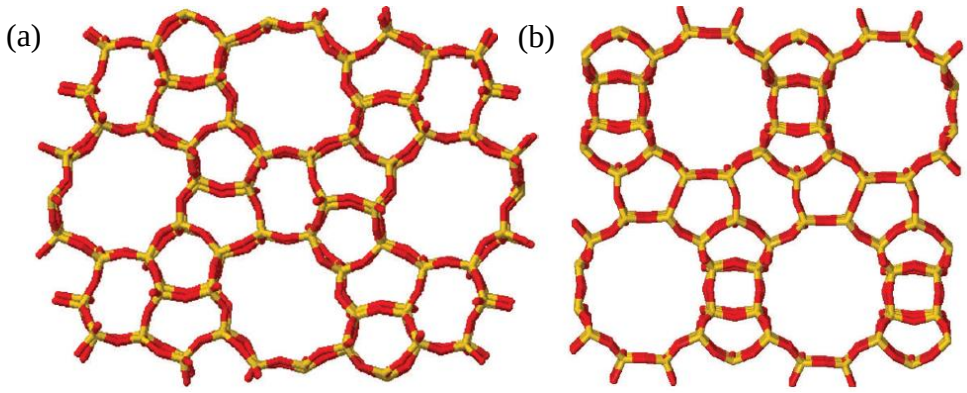

Figure 1.2. Structures of ZSM-5 (a) and beta zeolite (b).

Synthesis of well-structured microporous materials with larger pores can improve the accessibility towards the active sites [12], [13]. Another way is to create secondary mesoporous systems within the microporous zeolitic matrix by the preparation of hierarchical

materials containing micro- and mesoporosity [14], [15]. According to IUPAC, the classification of pore sizes is as follows [16]:

1. Micropores: pores with a diameter not exceeding 2 nm.
2. Mesopores: pores with a diameter between 2 and 50 nm.
3. Macropores: pores with a diameter greater than 50 nm.

1.1.1 Brönsted and Lewis acid sites

The strong intrinsic acidity makes zeolites unique materials with numerous industrial applications such as catalysts, adsorbents, and molecular sieves. The different acid properties should exert considerable effects on activity and product distribution in many reactions [17].

The acid sites are mostly localized inside the pores. Acidic properties of the zeolites are associated with the presence of Al tetrahedrally coordinated in the lattice. When Al substitutes for Si in a tetrahedral zeolite framework, a cation is required to compensate the Al tetrahedron. If this cation is a proton this leads to Brönsted acidic properties. The proton is attached to the oxygen atom connected to Si and Al atoms, resulting in the called bridged hydroxyl group (Si-O(H)-Al) which is responsible for the Brönsted acidity of zeolites [5].

In addition to Brönsted acid sites, zeolites can also possess Lewis acid sites. Structural Lewis sites can be generated by dehydration of zeolite structures at high temperatures, which leads to dehydroxylation of the Brønsted. Water is split off and Lewis acid sites are formed (Figure 1.3) [18]. Thus, increasing Si/Al ratio in the zeolite framework increases the number of acid sites if all cation sites are populated by protons [19], [20].

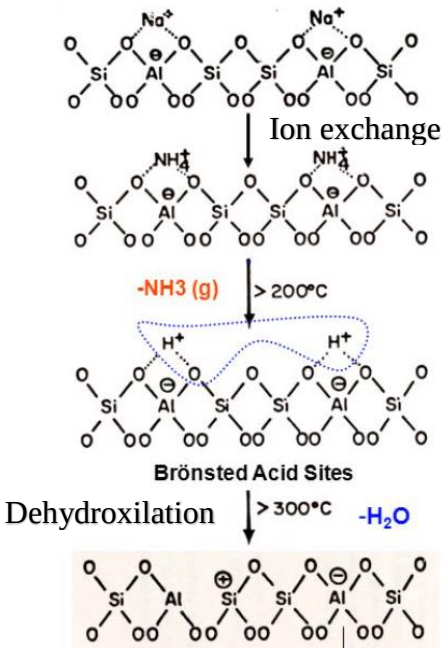

Figure 1.3. Formation of Brönsted acid sites and transformation in Lewis acid sites.

In general, the number of Lewis acid sites is much smaller in zeolites than the number of Brönsted ones [20]. The reactivity of the acid sites in the pores of zeolites depends on the composition, location and zeolite framework [21].

Acidity can be characterized by physical techniques, such as microcalorimetry of adsorbed probe molecules (ammonia, pyridine or other amines for acidity characterization and CO_2 or SO_2 for basicity characterization), temperature programmed desorption (TPD) (ammonia or any amine), magic angle spinning nuclear magnetic resonance (MAS-NMR) of Al, Si, H elements and of H, C, P, etc. of adsorbed probe molecules, infrared spectroscopy (IR) of hydroxyl groups, adsorption of several probe molecules (ammonia, pyridine, piperidine, amines, CO, H_2, etc.) and model catalytic reactions [18], [22], [23]. Infrared spectroscopy is the most used technique for measuring acidity in porous solids with pyridine

as the probe molecule. The interaction between pyridine and Brönsted and Lewis acid sites forms species correlated with the type and concentration of the acid sites [24]–[26].

1.1.2 Direct Preparation of Hierarchical Zeolites

Due to their unique structure, zeolites are widely used as catalysts. The major challenge is the diffusion limitation caused by the limited pore size (<1 nm) for the transformation of bulky reactants especially in catalytic applications related to the oil upgrade and synthesis of fine chemicals [8], [27]. This causes blocking of the micropores and deactivation of the catalyst. The rate of coke formation varies among the different zeolites used and the topology, as well as acid site density and strength, play major roles. As coke formation results in rapid deactivation of the catalyst, suppression of catalyst deactivation has been attempted by employing hierarchical zeolites prepared via different routes [28]. As shown by Hartmann *et. al.* (2016) (Figure 1.4), data obtained so far indicate that the shortening of the diffusion path length by reducing the crystal dimensions (preparation of either nanocrystals or zeolite nanosheets) results in enhanced catalyst lifetime. The introduction of additional (macro)porosity by different synthetic strategies also reduces the diffusion paths and, thus, potentially also catalyst deactivation. The mesoporosity increases the accessibility of large molecules to the micropores while simultaneously maintaining the acidity and crystallinity of zeolites [27], [28].

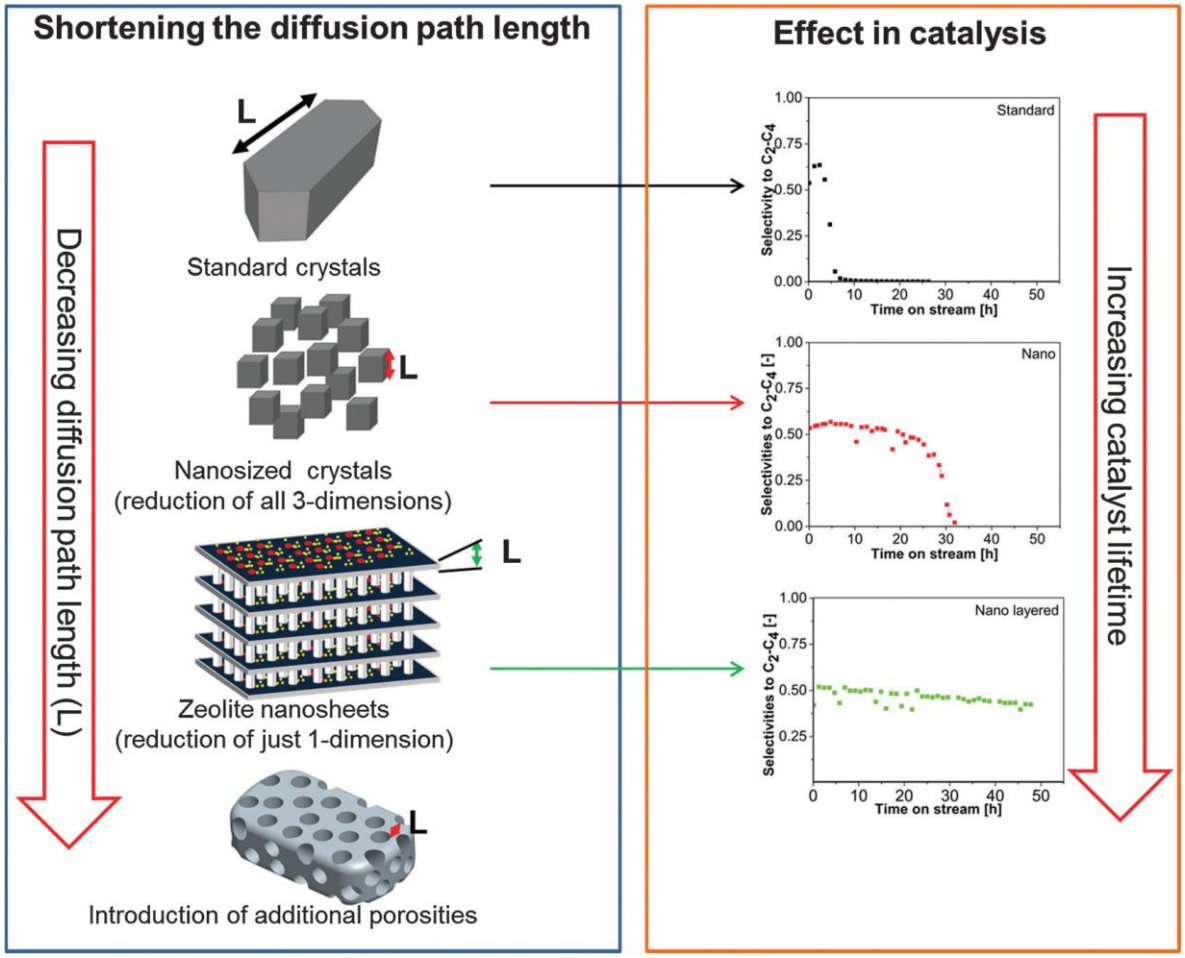

Figure 1. 4. Influence of the reduced diffusion path length. Left side: different strategies used to reduce the diffusion path lengths. Right side: impacts of different diffusion path lengths in catalysis [29].

The synthesis of mesoporous or hierarchical zeolites is one of the solutions to reduce diffusion limitations over zeolite catalysts. There are two major methods for the synthesis of hierarchical zeolites that can be divided into two main groups: Bottom-up and Top-down (Table 1.1) [29].

Table 1.1. Routes for secondary porosity generation [29].

HIERARCHICAL, MESOPOROUS ZEOLITES Routes for secondary porosity generation			
BOTTOM-UP		TOP-DOWN	
	Hard-templating methods	Dealumination	
	Soft-templating methods	Desilication	
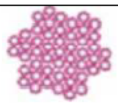	Assembly of nanosized zeolite	Irradiation	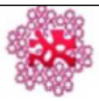
	Zeolitization of materials	Recrystalization	

1. Bottom-up: the bottom-up methodology includes hard templating, soft templating and non-templating. The template is introduced in the synthesis of the zeolite or by the modification of the synthesis condition (non-templating methods).
2. Top-down: top-down comprise strategies like demetallation, dealumination and recrystallization. The top-down approaches introduce secondary porosity on already existing crystalline zeolitic materials via post-synthetic modifications.

One of the most common methods to create mesoporosity is removing framework atoms (Al and Si) by demetallation, which includes dealumination and desilication. The changes which take place in the zeolite structure in desilication and dealumination processes are shown in Figure 1.5.

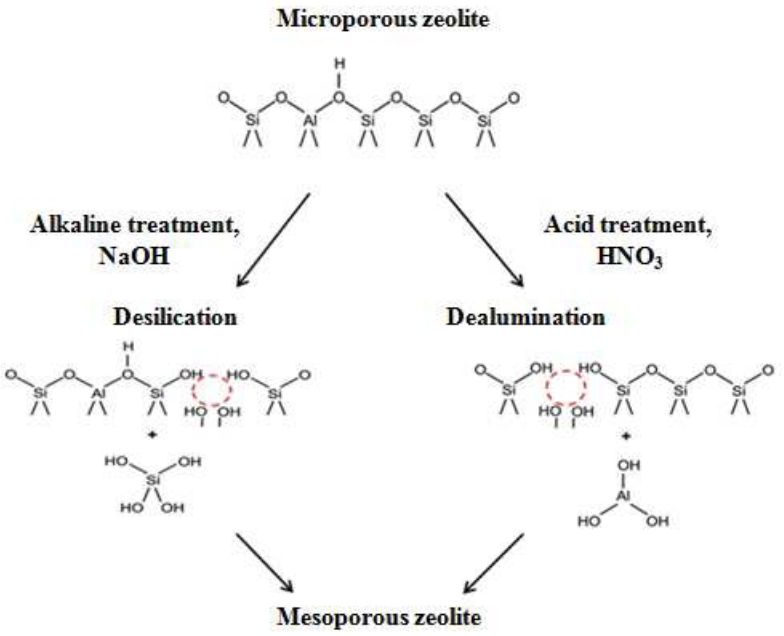

Figure 1.5. Desilication and dealumination method [29].

Desilication is based on silicon extraction from the zeolite structure in an alkaline environment (NaOH). An alkaline environment allows maintaining crystallinity with simultaneous reduction of micropores volume and considerably increases the mesopore volume. This method affects the structural and acidic properties of the materials, thus affecting the activity, selectivity, and life-span of zeolites [30], [31].

Dealumination is the removal of aluminum from the zeolite structure by the use of chemical agents or hydrothermal treatment. The most used method is the elution of aluminum with acid at high temperatures [32]. The extraction of the aluminum atom is accompanied by the partial breakdown of the zeolite structure and the formation of vacancies. These vacancies constitute additional porosity, mainly in the range of mesopores in the microporous structure in the zeolite. However, one must also take into account the fact that extraction of aluminum atoms may be also a cause of serious changes in the acidic properties of the zeolite. The

dealumination process was one of the pioneering methods in introducing porosity into zeolites. However, the poor connection and depth of the generated pores coupled with serious damage to micropores and crystalline properties in adverse processing conditions necessitated searching for new methods of mesoporosity generation. The major disadvantage of the "top-down" methodology is the partial destruction of the zeolite structure during the processing [28].

Mesoporosity can be effectively introduced into the structure of a material by recrystallization of microporous zeolites to micro/mesoporous or mesoporous materials. The process uses cation surfactants such as cetyltrimethylammonium bromide (CTABr) or cetyltrimethylammonium chloride (CTACl) and mild conditions of synthesis, which prevent dissolution of crystals by providing interaction between the surfactant and zeolite and enable achieving almost total reorganization of the zeolite network around surfactant micelles [28], [29].

"Bottom-up" approaches are based on the addition of secondary templates to the synthesis mixture of microporous zeolites. The dual template strategy combines a structure-directing agent for the synthesis of the zeolite and a surfactant template for the preparation of the meso-phase added in the starting synthesis mixture. The surfactant would generate micelles, which serve as a template for the mesostructure and the structure-directing agent leads to the crystallization of the zeolite entities in the pore walls of the mesostructure [33].

Hard templates like carbon nanotubes or nanoparticles, $CaCO_3$, metal oxide nanoparticles, aerogels, polymers and resin beads have been used to create meso- and macroporosity during the crystallization [33], [34]. Jacobsen and co-workers synthesized mesoporous zeolites using carbon nanoparticles in acidic or alkaline solutions as mesoporous

templates [35]. The ZSM-5 zeolite gel grows on the carbon particles and the mesopores were obtained via removing the carbonaceous matrix by calcination. Also, carbon nanotubes lead to obtaining simple and uniform mesoporous channels open to the external surface in zeolite crystals [36], [37]. The synthesis of hierarchical zeolites by carbonaceous matrices as a hard template is shown in Figure 1.6 [33].

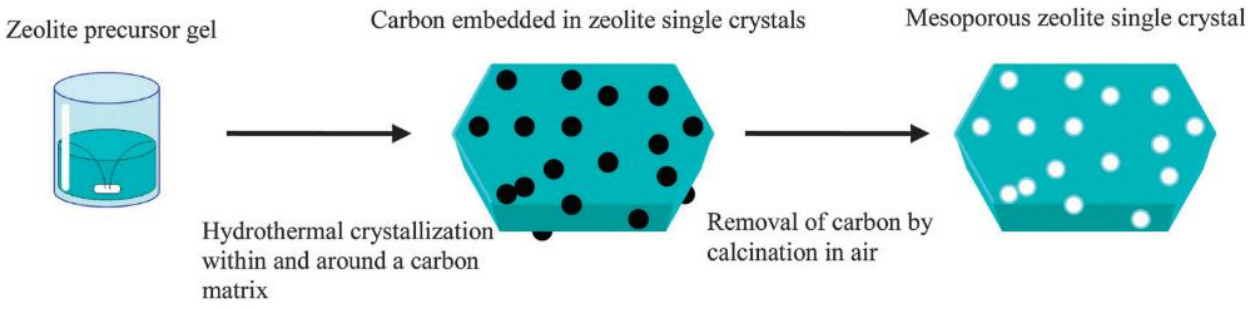

Figure 1.6. Carbonaceous templates: synthesis of hierarchical mesoporous zeolites using carbonaceous matrices as a hard template.

Hierarchical zeolites allow improving the accessibility of the pores which involves both less steric limitations for converting bulky molecules and an increase in the intracrystalline diffusion rate. Due to the mesoporosity, the residence time inside the pores avoids secondary reactions, decreasing deactivation effects of the coke and increase lifetime. Moreover, the secondary porosity offers a space for deposition of additional catalytic active phases (metal, metal oxides, sulphides, nitrides, etc.) controlling their size and achieving a high dispersion and strong interaction with the zeolite support. As a consequence of all these factors, hierarchical zeolites display a significant enhancement of the catalytic activity and stability in the reactions such as Fischer-Tropsch synthesis [33], [38].

1.1.3 Composite metal-zeolite catalysts

Catalytic materials exist in various forms and their preparation involves different protocols with several possible preparation schemes. The goal is to produce and reproduce a commercial product that can be used as a stable, active, and selective catalyst. To achieve this goal, the best preparation solution is sought, which results in sufficiently high surface area, good porosity, and suitable mechanical strength. The first of these, surface area, is an essential requirement in that reactants should be accessible to a maximum number of active sites [39].

The successful use of zeolites is based on their inherent shape-selective structures. However, although many excellent results have been obtained using zeolites in a wide range of reactions, they cannot work properly in the presence of bulky molecules, because such molecules cannot diffuse into the zeolite microporous structures. Only active sites close to the zeolite pore entrances or on their external surfaces, which represent at most 5% of the total number of active sites, are available for bulky molecules [45][46]. These constraints have stimulated research on zeolitic structures.

The hierarchical zeolites with larger pores systems enhance diffusion of bulky reactant molecules into the pores and of large product molecules out of the pores. This shortens the distance to the active sites and facilitates adsorption and catalytic reactions. Zeolitic acid catalysts are produced, when the cations present in the freshly synthesized material are replaced with protons. Ion exchange is normally accomplished using an aqueous ammonium salt, and the resulting material is calcined to produce the acid form [40].

Bifunctional catalysts present two types of active sites, usually metallic sites and acid sites. The association between the acid and metallic sites increases catalytic activity and

product yield. The function of metallic sites is dehydrogenation/hydrogenation and the function of the acid sites is to conduct acid-catalyzed reactions (e.g. cracking, isomerization and others) [25]. Several components may be responsible for hydro-dehydrogenation such as transition or noble metals with good dispersion (platinum (Pt), palladium (Pd) and other), metal sulphides and metal oxide (cobalt (Co), nickel (Ni), iron (Fe), copper (Cu)) supported on zeolite [41][42].

In bifunctional catalysis, the strength of acid sites and distribution of metal and acid sites are important parameters. The kinetic steps of the reactions are coupled to each other through the processes of diffusion of the intermediates from one type of sites to another. Therefore, the two types of active sites should be as closer as possible for attaining higher catalytic activity and selectivity [43].

The crystallization method is a preparation of homogeneous microporous solids in which the active phase is distributed uniformly into the monophase crystalline solid. These microporous crystalline solids are structurally based on frameworks formed by linked TO_4 tetrahedra with each oxygen shared between two T elements [39].

The most used methodology to introduce metals into zeolites is incipient wetness impregnation, also called capillary impregnation or dry impregnation. This method consists in adding to the catalytic support a solution containing metal precursor that fills the zeolite pores followed by drying, calcination/reduction steps. This technique is called “incipient wetness impregnation”, when the volume of solution is equal or smaller than the total pore volume of support [39].

When the interaction strength of the active precursor in solution with the support is weak, the method of incipient wetness impregnation followed by drying may be used to apply

high loadings of precursors; the maximum loading is limited by the solubility of the precursor in the pore filling solution. On the other hand, increasing the weight loading requires higher concentrations which, for reagents such as $Ni(NO_3)_2$, results in lower solution pH and, may cause support disruption and substitution of ions into the support lattice. However, in the absence of sufficiently strong interactions, the drying step usually results in severe redistribution of the impregnated species, and the support can become non-uniformly covered by the active material in the final catalyst [39], [44].

Normally, two routes lead to the isomorphous substitution of transition metal ions for Si and/or Al ions in zeolite frameworks: one is the direct hydrothermal crystallization, and the other is the post-synthesis of zeolite. The direct hydrothermal synthesis is considered to be more effective than the post-synthesis. However, in most of works, cobalt-substituted zeolites were prepared by post-synthesis methodology, with the disadvantage of forming the irregularly distributed extra-framework cobalt species [45].

Zeolites are cationic exchangers. They combine the unique features of high ion exchange capacity, crystalline structure, and uniform pore sizes. The catalytic properties of noble and transition metals and steric constraints imposed by the zeolite structure have provided a strong incentive for developing reliable procedures to prepare highly selective supported-metal catalysts with narrow particle size distributions [46], [47].

The method of ion exchange allows introduction, in a controlled way, of a precursor from aqueous solution onto the support. The term ion exchange has been used to describe all processes, where ionic species from aqueous solution are attracted electrostatically by charged sites on the support surface. Zeolites are ideal ion exchangers because the crystalline lattice bears electric charges. Compensation of electric charges is a prerequisite for stability

of the crystalline structure. As a consequence, the lattice charge is compensated by oppositely charged ions bound electrostatically in extra-lattice positions. These ions are readily exchanged by ions bearing an equivalent charge from aqueous solutions [45], [48].

Complications arise from side phenomena that accompany the calcination and reduction steps: migration of metal ions into smaller zeolite cages where their reduction requires higher temperature; autoreduction of metal ions by decomposing NH_3, which causes agglomeration of larger particles; proton generation during metal reduction which changes the acidity of the catalyst [49] .

Flores *el al*. (2019) controlled both the cobalt distribution between the external surface and micropores and acidity of the large pore BEA zeolite by choosing the sequence of impregnation and ion exchange procedures. Cobalt ions, introduced during impregnation, can occupy cation exchange positions in the zeolite micropores decreasing the number of acid sites available and, the isolated Co ions in the cationic positions can be very difficult to reduce to the metallic state, thus decreasing the amount of available metal active phase. Moreover, the metal particles in the narrow zeolite micropores are more susceptible to suffer from diffusion limitations due to the small pores of the zeolite in the presence of larger compensation cations. In addition, the use of larger compensation cations during impregnation can restrain diffusion of Co ions inside the zeolite pores during the ion exchange and thus affect cobalt distribution between the zeolite external surface and micropores (Figure 1.7) [48].

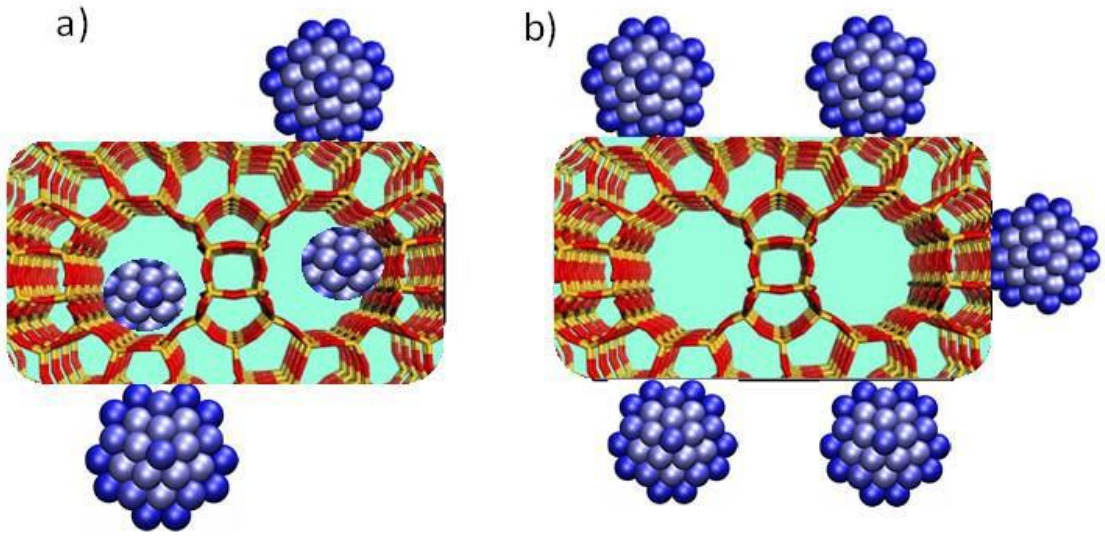

Figure 1.7. Localization of cobalt species in the CoH/HBEA (a) and CoH/NaBEA zeolite (b) [48].

A higher concentration of ion exchangeable cobalt was observed in the catalyst prepared by ion exchange of the zeolite proton form. The presence of Na^+ instead of H^+ ions in the exchange positions of zeolite favored the deposition of cobalt on the external surface. The acid sites in the zeolite micropores were then restored by subsequent ion exchange of sodium with ammonium nitrate and calcination [48].

Using zeolites with micrometer-scale crystallites can hinder the diffusion of bulky molecules, because the extensive surface areas of the internal parts of the framework can only be accessed by the molecules with kinetic diameters less than 1.5 nm, and most natural and synthetic zeolites consist of micrometer-sized crystallites [50].

Increasing the exposure at metallic and acid sites with enhanced specific surface areas can be achieved by reducing the solid particle size or introducing an open pore system (Figure 1.8). An attractive procedure for zeolite synthesis involves the use of a combination of an inert porous matrix such as carbon black or carbon nanotubes – hard templates - and a

conventional synthesis gel, resulting in growth into the enclosed spaces of voids with nanoparticle dimensions and creating mesoporosity [50].

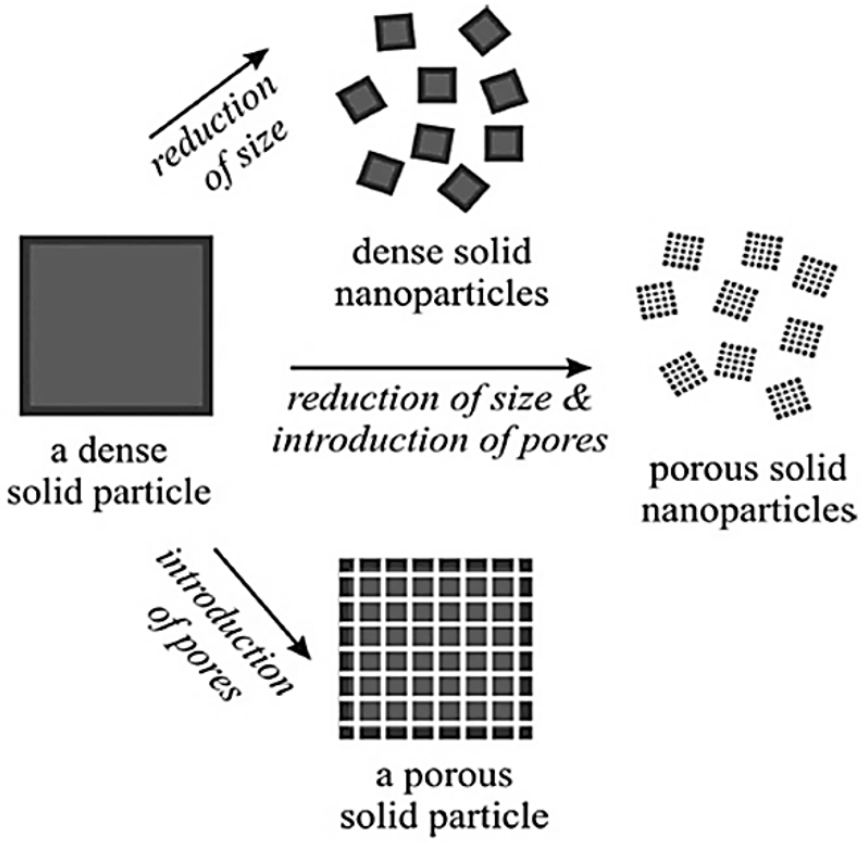

Figure 1.8. Increasing surface areas of dense solids [50].

The use of hard templates in conventional zeolite synthesis gels can induce additional porous systems in the zeolite framework structure. After zeolite crystal formation, combustion in air is conducted to remove the carbon template and obtain mesopores comparable to the carbon particle size. The hydrothermal stability of the template under the reaction conditions also is an important issue because it must not be damaged during the zeolite synthesis [35].

Mesoporosity enhances the zeolite surface area. Hierarchical - micro and mesoporous - structures also promote homogeneous dispersion of active components such as metals or oxides on the catalyst surfaces. Because of these improved properties and their intrinsic hydrothermal stabilities and strong acidities, hierarchical zeolites are important commercial catalysts [51].

The strategy of using metal-carbon nanotubes as a secondary template is a new single-pot synthesis strategy for the design of metal-zeolite nanocomposites. This methodology allows to the creation of a specific shape, enhanced mesoporosity, and uniform distribution of highly dispersed metals such as ruthenium, cobalt, nickel, and magnesium within the zeolite crystals. The presence of the carbon nanotubes in the zeolite synthesis serves as a replica to create zeolites with specific fibrous morphology. They fulfill the role of a mesoporogen, markedly increase the zeolite secondary porosity and act as a vehicle to uniformly introduce the metal functions inside the mesoporous zeolites [52].

The concentration, intrinsic activity, and the localization of the metals within the zeolite structure are of utmost importance for the catalyst activity, selectivity, and stability [49], [53]. Among the hard templates to create the hierarchical structures, the carbon nanotubes (CNT) are very versatile materials [54][55]. Addition of CNT with metal oxides to the zeolite synthesis gel results in excellent hierarchical catalysts. The metal−CNT acts as mesoporogen and strongly enhances the zeolite mesoporous volume. The zeolite synthesis in the presence of metal−CNT offers an opportunity to simultaneously introduce new catalytic functions leading to bifunctional metal−zeolite nanocomposites. The zeolite crystallites obtained in the presence of metal CNT templates exhibit a rather irregular fibrous morphology leading to the development of zeolite mesoporosity. This morphology arises

from CNT partially encapsulated inside the zeolite crystals during the zeolite synthesis (Figure 1.9). After calcination, the introduced metals are uniformly distributed within the zeolite crystals and the CNT is removed [52].

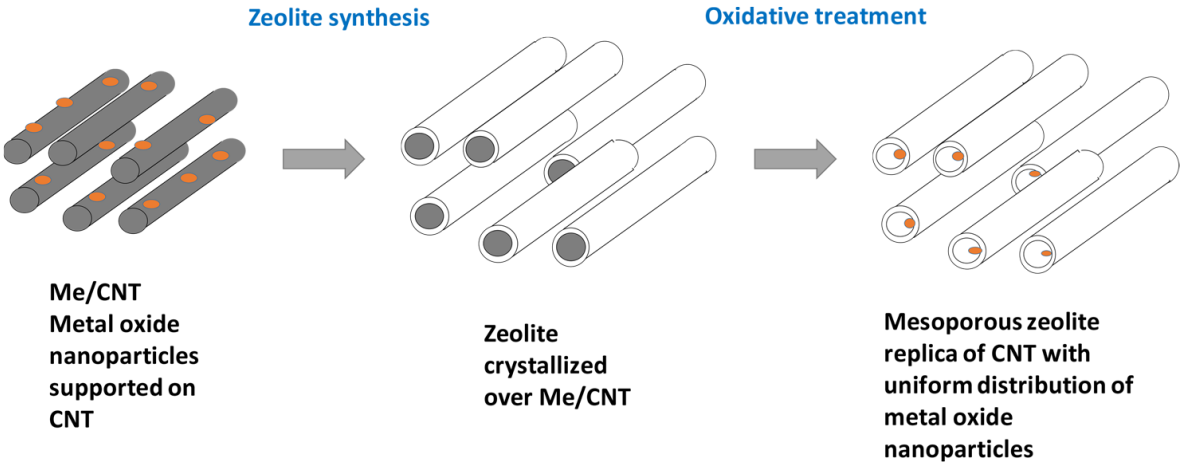

Figure 1.9. Synthesis of metal-zeolite nanocomposites using metal/CNT as secondary hard templates [52].

1.2 Use of bifunctional catalysts in Fischer-Tropsch synthesis

1.2.1 Fischer-Tropsch synthesis

Fischer-Tropsch (FT) synthesis is a catalytic reaction in which hydrocarbons are produced from synthesis gas (syngas): a mixture of carbon monoxide (CO) and hydrogen (H_2) [56]. The syngas is obtained from coal, natural gas, or biomass. FT synthesis is used for producing chemicals and fuels (Figure 1.10). The actual interest in FT synthesis has grown up in consequence of environmental demands, technological developments and changes in fossil energy reserves. This process is an alternative source environmentally-sound

production of chemicals and fuels from biomass, coal and natural gas to supply the world energy demand, as petroleum reserves are depleting [57]–[60].

Figure 1.10. Conversion of non-petroleum sources into liquid fuels and chemicals via syngas [61].

The main products of the Fischer-Tropsch synthesis are paraffins and olefins, whose reactions are shown respectively in the equations below:

Paraffins: $nCO + (2n + 1)H_2 \rightarrow C_nH_{2n+2} + nH_2O$

Olefins: $nCO + 2nH_2 \rightarrow C_nH_{2n} + nH_2O$

The FT synthesis is a reaction that consists of many elementary main and side reactions depending on the operational conditions, such as temperature, composition of the gas (H_2/CO ratio) and type of catalysts [60], [62]. Below are presented the side reaction.

Water Gas Shift (WGS): $CO + H_2O \rightarrow H_2 + CO_2$

Alcohols: $nCO + 2nH_2 \rightarrow C_nH_{2n+1}OH + (n-1)H_2O$

Boudouard reaction (coke): $2CO \rightarrow C + CO_2$

Oxidation of metal: $xM + H_2O \rightarrow H_2 + MO_x$

The Fischer-Tropsch process can be performed at low or high temperatures. The low-temperature Fischer-Tropsch (LTFT) is operated at temperatures between 220 ºC and 250 ºC and uses cobalt or iron-based catalysts. LTFT reactors are operated at high chain growth probability conditions, at which heavy paraffinic hydrocarbons are produced with high selectivities. Indeed, the LTFT synthesis will produce preferably middle distillates, which are used for the formulation of diesel fuels. Lower hydrocarbons are expected in processes based on high-temperature Fischer-Tropsch (HTFT), which generates olefins, oxygenates and paraffin of gasoline range. HTFT is operated at temperatures between 330°C and 350 °C and uses an iron-based catalyst [63]–[65].

The performance of the FT synthesis depends strongly on temperature. Increasing temperature favors the formation of methane, deposition of carbon (coke) and thereby deactivation of the catalyst (particularly with iron) and reduces the average chain length of the products, which is undesirable when the maximum ultimate diesel yields are desired in a process combination with hydrocracking [60].

The reaction mechanism of FT synthesis is a surface polymerization that yields a product distribution with different molecular weights. The mechanism of the reaction has been studied until the present day, because the synthesis of hydrocarbons from biomass is a complex catalytic process involving many consecutive and parallel transformations [66], [67]. In general, the mechanism involves six reaction steps shown [68]:

1. Reactant adsorption
2. Chain initiation
3. Chain growth
4. Chain termination

5. Product desorption

6. Re-adsorption and further reaction

In most cases, steps 2 through 4, are accurately described by the Anderson–Schulz–Flory (ASF) kinetic model [69]. The ASF model assumes the hydrocarbon chain length distribution with a probability factor, α. This model provides the α constant for all propagation steps, but this value may change due to location in the reactor, temperature and concentration differences [70], [71]. The model can be described as:

$$m_n = (1-\alpha)\alpha^{n-1} \quad (1)$$

where m_n is the probability of producing a molecule with n carbon and is equal to the instantaneous molar fractions m_n produced. The distribution of hydrocarbons products is defined as:

$$\alpha = \frac{r_p}{r_p + r_t} \quad (2)$$

where r_p is the rate of propagation and r_t is the rate of termination [68]. The chain growth towards olefins and paraffins according to ASF distribution is between 0.77 and 0.93 [72]. The relation between the growth chain and wieght fraction of a hydrocarbon is defined by Equation 3.

$$w_n = n(1-\alpha)^2\alpha^{n-1} \quad (3)$$

where w_n is the weight fraction of a hydrocarbon with carbon number n [73]. The calculated ASF distribution of several ranges of hydrocarbon chains is shown in Figure 1.11. As the

Figure 1.11 shows for the production of transportation fuels (C_{12}–C_{18} diesel) the optimal value is 0.87 [68].

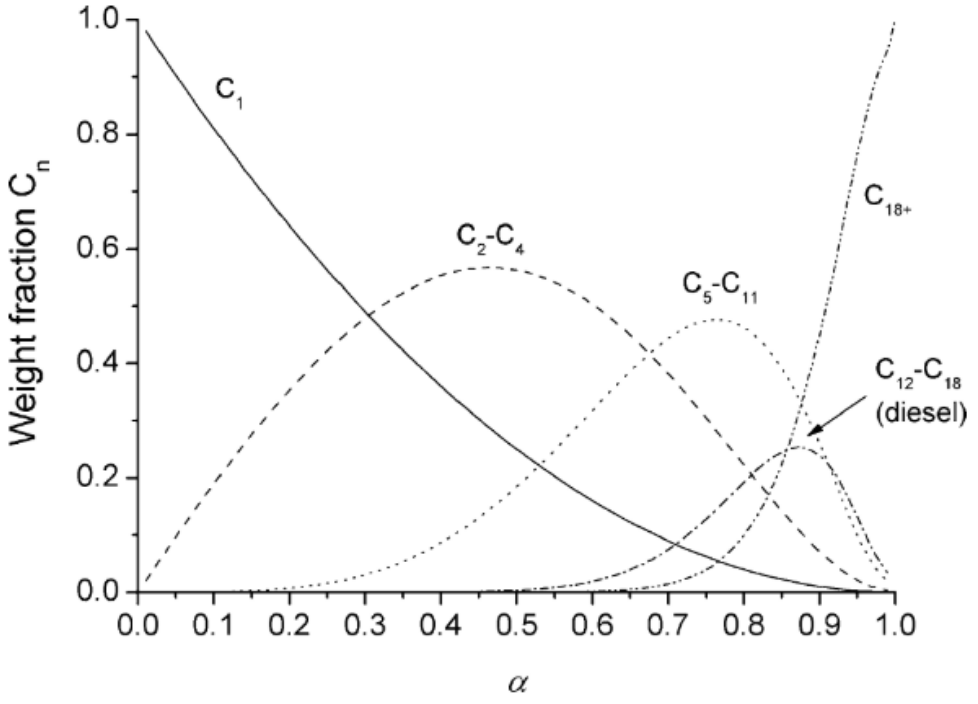

Figure 1.11. Weight fraction of hydrocarbon chains of length *n* as a function of the growth probability factor α.

Different mechanisms based on different intermediates were proposed to govern the FT product composition. Carbide mechanism, CO insertion and hydroxycarbene mechanism are the main polymerization schemes that have been proposed within the three major steps (initiation, propagation and chain termination steps).

1. The carbide mechanism involves dissociative adsorption of CO and H_2. Firstly, the metal surface is carbidized by gaseous carbon monoxide. CO is chemisorbed in a bridge mode involving two surface sites of the catalyst and also is equilibrated with a linear mode involving only one site of the metal surface. The C-O bond is dissociated into C and O

surface species. Hydrogen is also chemisorbed and dissociated on the metal surface. The carbide reacts with the hydrogen forming intermediates such as CH, CH_2 and/or CH_3 due to chemisorbed surface hydrogen atoms. The hydrogenation of surface C atoms of metal carbides to surface CH_2 (methylene species) removes the oxygen as water [74].

Another possibility to form monomers is the formation of enol groups during the reaction of adsorbed CO with surface hydrogen. The hydrogenation of surface enol groups results in the formation of methyl groups and eliminates the oxygen as water (Figure 1.12).

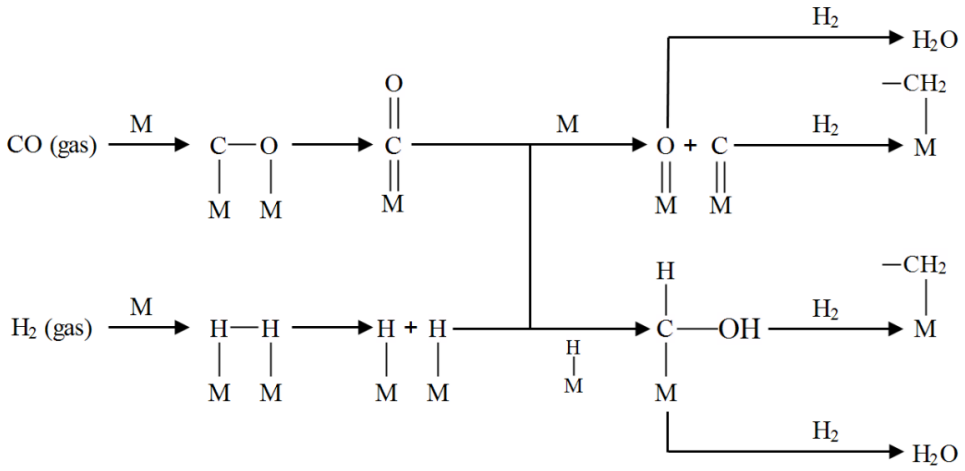

Figure 1.12. Initiation step in carbide mechanism during Fischer Tropsch synthesis reaction.

Different routes could govern the propagation and chain termination in the synthesis process to produce hydrocarbon molecules. A high-temperature FT reaction condition favors the reaction to follow the first path and a lower FT reaction temperature causes the oxygenation of the enol groups with a further reaction [74]. The insertion of CH_x groups into the metal-carbon bonds leads to the synthesis of long chain hydrocarbons [75]. The propagation of monomer units is shown in Figure 1.13.

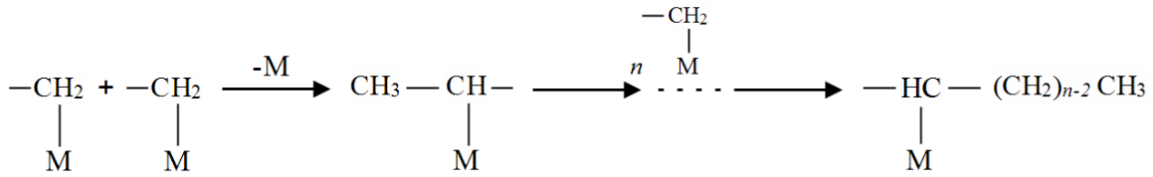

Figure 1.13. Chain propagation of monomer units in carbide mechanism during FT synthesis reaction.

The chain termination is followed by: (i) dehydrogenation/desorption of a grown chain to olefin, (ii) hydrogenation of a C_xH_y intermediates to paraffin or (iii) disproportional growth of C_xH_y intermediates to paraffins or olefins. The methylene (CH_2 adsorbed) is the key intermediate species [74]–[77].

2. The CO insertion mechanism is the CO insertion into the metal-carbon bonds what summarizes the general chain growth pattern in the FT synthesis process. The chains are grown by the insertion of carbon monoxide into the metal-alkyl bonds in homogeneous catalysis followed by reduction of the acyl group. The hydrogenation of the resulting acyl groups governs the termination to oxygenates or different hydrocarbons [78]. This mechanism is demonstrated in Figure 1.14.

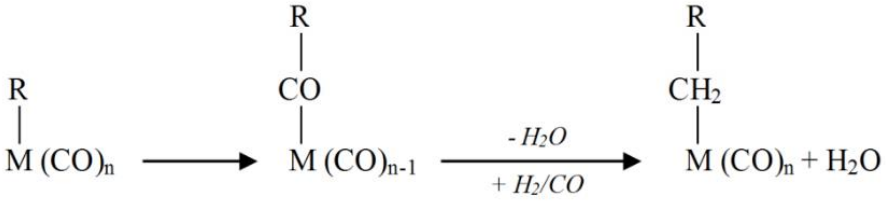

Figure 1.14. General chain growth pattern in CO insertion mechanism, R represents H or alkyl group.

This mechanism is supposed to happen in the case of the reaction over ruthenium or iron catalysts [79].

3. Hydroxycarbene mechanism is based on the formation of hydroxycarbene (CHOH) intermediates (Figure 1.15). Hydrogenation of chemisorbed carbon monoxides on the metal surface by chemisorbed atomic hydrogen form hydroxycarbene. The water elimination through the condensation of two hydroxymethylene groups forms the C-C bonds. The chain is grown by the co-operation of oxygenated surface intermediates [77].

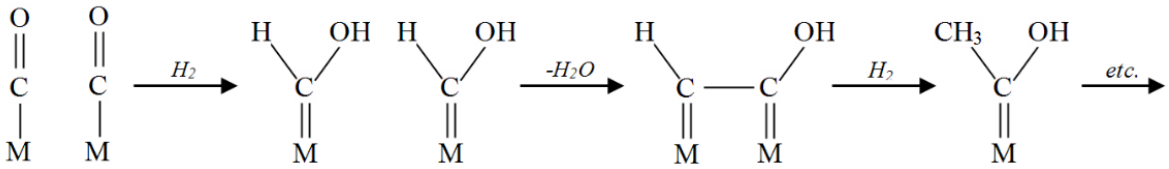

Figure 1.15. Chain growth pattern in CO insertion mechanism, R represents H or alkyl group.

The production of products with the desired carbon number is a highly desirable in the development of catalysts for FT synthesis. This remains a huge challenge for future research [58], [61]. Due to the wide product distribution, FT products must be subjected to further refining to produce high-quality liquid fuels such as gasoline, jet fuel and diesel fuel. For that, it is necessary to increase the selectivity to C_{5+} hydrocarbons and to decrease the selectivity to CH_4 and C_2-C_4 paraffins at high CO conversion [80]. On the other hand, the direct production of high-quality liquid fuels from syngas without refining stage would be more energy- and cost-efficient, and could increase the competitiveness of FT technology for the production of liquid fuels. This requires the design of novel FT catalysts with high selectivities to a desired range of hydrocarbons [80]–[84].

The bifunctional catalysts for FT synthesis are composed of metal active sites for the hydrogenation of CO to form hydrocarbon chains (FT functionality) and acid sites where hydrocracking and isomerization reactions occur immediately after chain formation (Figure 1.16). The ideal FT active site has to favor both C−H and C−C coupling; if only C−H coupling occurs, the main product would be CH_4 [85].

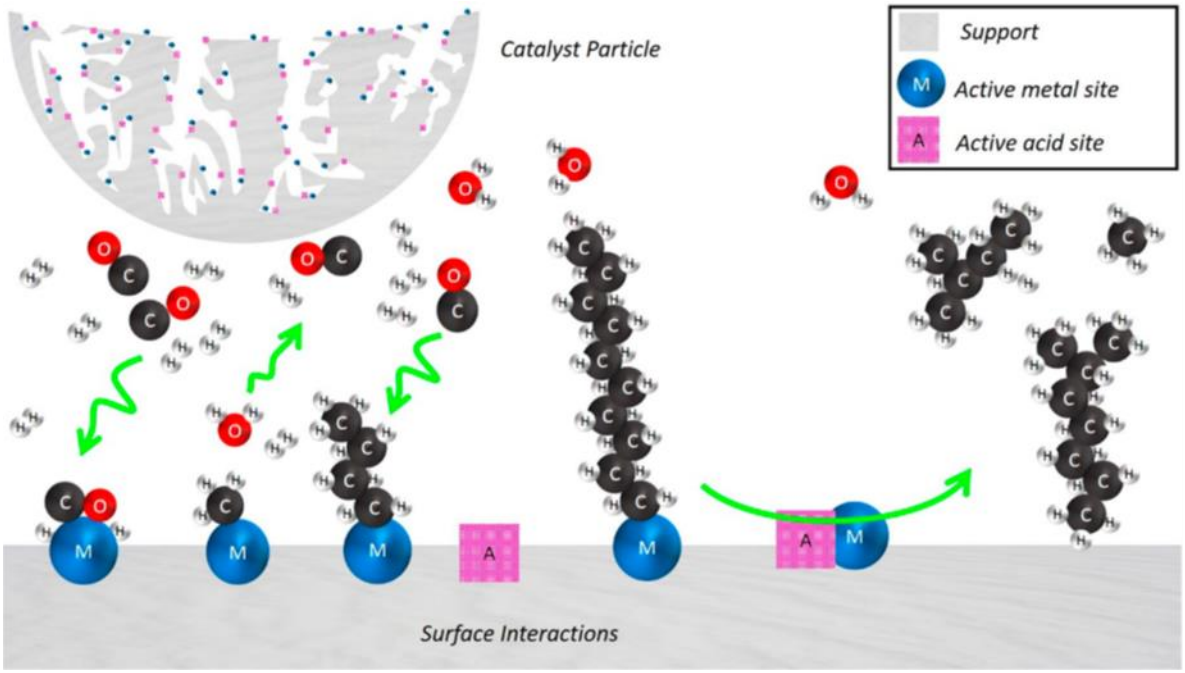

Figure 1.16. Schematic illustration of the one-stage FT process: hydrocarbon chain growth followed by hydrocracking and isomerization [85].

The support material may be used to modify the Fischer-Tropsch reaction by providing another conversion pathway. The bifunctional catalysts containing an active FT component, e.g. Co or Ru, and acid active sites for cracking and isomerization can provide directly the valuable products from syngas. The acidity of zeolites and other acidic materials has been employed to modify the carbon number distribution and degree of branching by

acid catalysis in parallel with Fischer-Tropsch synthesis by using acidic supports [86], [87]. Two methods for hydrocarbon selectivity control were proposed recently, nanoreactors [88], which consist of a core, commonly the active phase, surrounded by a porous shell [89], and microemulsion [90]. In these methods, the carbon chain length is limited by steric and diffusion limitations [91].

Several methods have been proposed for the selectivity control in FT synthesis. First, catalytic cracking/isomerization of FT hydrocarbons can upgrade the reaction products to a specific fuel. The combination of FT synthesis process with hydrocracking and isomerization of long chain hydrocarbons restricts the hydrocarbon distribution to a more convenient range [92]. The isomerization and cracking of FT hydrocarbons would lead to iso-paraffins or diesel fuels constituted by the C_{10}-C_{20} hydrocarbons. This multistage process, however, significantly reduces the efficiency of synthetic fuel production.

Isomerization is a reaction leading to the production of isomers (same molecular size, type and atoms number but with a different molecular arrangement) [85]. The hydrocarbon isomerization is conducted for obtaining branched isomers, because they are chemical compounds with a high commercial value. The octane number of the branched hydrocarbons is higher than that for linear compounds.

Olefin isomerization is a fast reaction, while isomerization of paraffins is slower and requires very high temperatures. The paraffin isomerization reaction occurs on a bifunctional catalyst with acid sites for isomerization by carbenium ions produced from olefins and metallic sites for dehydrogenation/hydrogenation from paraffins to olefins and vice versa. Assuming the classical mechanism, the paraffins dehydrogenate first on the metal sites and the protonated olefins are produced over the Brönsted acid sites [93], [94].

Cracking is a reaction, which involves a rupture of the C-C bonds of hydrocarbons. It occurs upon acid active sites of solid surfaces after the formation of carbocations [95].

1.2.2 Catalysts

Fischer-Tropsch selectivity can be manipulated by the catalyst formulation, operating conditions, and reaction engineering. High Fischer-Tropsch activity requires metals that allow dissociative CO and H_2 adsorption. The catalysts must be active, selective and stable in order to obtain high productivity. The metals most often studied are Fe, Co, Ni and Ru. By selecting the Fischer-Tropsch active metal that forms the basis for the catalyst formulation, many of the important catalyst properties are determined [96].

Cobalt and iron are metals proposed for Fischer-Tropsch catalysts for syngas conversion. Both metal catalysts have been used in the industry for hydrocarbon synthesis. The general perception is that Fe-based Fischer-Tropsch catalysts deactivate at a higher rate than their Co-based counterparts. Ni catalysts under practical conditions produce too much methane, at elevated pressure, the nickel tends to form nickel carbonyl. With increasing reaction temperature, the selectivity changes to mainly methane with nickel. This tendency is observed also with cobalt and ruthenium, but less excessive. [60], [75].

Cobalt -based catalysts are used in the LTFT process, at higher temperatures an excess of CH_4 is produced. Ruthenium is the most active catalyst for Fischer-Tropsch synthesis [97], [98]. This metal possesses several advantages compared to Co and Fe [99]. These advantages are high catalytic activity, high selectivity to long-chain hydrocarbons, high stability compared to any other FT metal [98], [100]–[103]. Because of the high prices of Co and Ru,

maximizing the available surface area of the metals is desirable. For that, the metal is dispersed on stable supports with the high available area such as Al_2O_3, SiO_2, TiO_2 and zeolites [104]–[108].

Impregnation is an effective method for the preparation of bifunctional metal-zeolite catalysts for the direct production of fuels from syngas. However, the introduction of metal ions to the zeolite may result in the neutralization of the zeolite acid sites. This represents a major drawback of this method. Metals ions, introduced during impregnation, can occupy cation exchange positions in the zeolite micropores decreasing the number of acid sites available for hydrocarbon isomerization and cracking. In addition, the isolated metal ions in the cationic positions can be very difficult to reduce to the metallic state, thus decreasing the amount of available metal active phase for FT synthesis [48].

Hierarchical zeolites suggest better accessibility and dispersion of both acid and metal sites. The strategy for the synthesis of hierarchical zeolites using metal supported CNT as secondary hard templates seems promising. It produces hierarchical zeolites replicating the shape of CNT. The metal oxide species seem to be nucleation sites and crystallization modifiers leading to the fibrous zeolite morphology, which largely replicates the CNT. This leads to an enhanced mesoporosity and highly dispersed, accessible, and uniformly distributed metal nanoparticles and acid sites [52].

1.3 Challenge and goals of the thesis

The interest in alternative, clean synthetic fuels and fine chemicals has been steadily growing in recent years. Zeolites offer the basis of many technological solutions for the production of clean synthetic fuels and chemicals.

The present PhD thesis focuses on the design of the new synthetic strategies for the preparation of the catalysts based on the specific interaction between metal oxides and zeolite. Nanocomposites of metal and hierarchically structured zeolites were synthesized and applied in the Fischer-Tropsch reaction. The goal was to create mesoporosity by introducing carbon nanotubes (CNT) with supported metal oxide nanoparticles as hard template in ZSM-5 and Beta synthesis. Another strategy is based on the synthesis of composite material by etching of mesopores in the zeolite with subsequent deposition of Ru nanoparticles inside of these mesopores and recrystallization to encapsulate the nanoparticles inside of zeolite crystals.

The strong interaction of metal oxide with zeolite has been used for the development of the method to increase the dispersion of the Ru metal in the catalyst. The metal nanoparticles have been impregnated over ZSM-5 with subsequent secondary crystallization. Our results show significant re-dispersion of embedded metal nanoparticles and an increase of activity.

1.4 References

[1] F.-G. Agnieszka, “Hierarchical zeolites: Synthesis and catalytic properties,” *Microporous Mesoporous Mater.*, vol. 15, pp. 33–45, 2018.

[2] M. Moliner, “Direct Synthesis of Functional Zeolitic Materials,” vol. 2012, 2012.

[3] A. Kharchenko, “Properties of copper species stabilized in zeolite nanocrystals,” Normandie Université, 2017.

[4] R. D. A. Bessa, “Síntese e caracterização de compósitos de zeólitas magnéticas utilizando caulim para abrandamento de águas,” Federal University of Parana, 2016.

[5] J. Weitkamp, “Zeolites and catalysis,” *Solid State Ionics*, vol. 131, pp. 175–188, 2000.

[6] P. K. D. Scott M. Auerbach, Kathleen A. Carrado, *Handbook of Zeolite Science and Technology*. 2003.

[7] J. Li, A. Corma, and J. Yu, “Synthesis of new zeolite structures,” *Chem. Soc. Rev.*, 2015.

[8] C. Martínez and A. Corma, “Inorganic molecular sieves: Preparation, modification and industrial application in catalytic processes,” *Coord. Chem. Rev.*, vol. 255, pp. 1558–1580, 2011.

[9] M. E. Davis and R. F. Lobo, “Zeolite and Molecular Sieve Synthesis,” *Chem. Mater.*, vol. 4, no. 4, pp. 756–768, 1992.

[10] M. M. J. Treacy and J. M. Newsam, “Two new threedimensional twelve-ring zeolite frameworks of which zeolite beta is a disordered intergrowth,” *Nature*, vol. 332, no. 17, pp. 249–251, 1988.

[11] and W. M. M. G. T. Kokotailo, S. L. Lawton, D. H. Olson, “Structure of synthetic zeolite ZSM-5,” *Nature*, vol. 272, no. 30, pp. 437–438, 1978.

[12] M. M. A. Corma, María J. Díaz-Cabañas, José Luis Jordá, Cristina Martínez, “High-throughput synthesis and catalytic properties of a molecular sieve with 18- and 10-member rings,” *Nature*, vol. 443, no. 7113, pp. 842–845, 2006.

[13] A. C. C. Freyhardt, M. Tsapatsis, R. F. Lobo, K. J. Balkus and M. E. Davis, “A high-silica zeolite with a 14-tetrahedral-atom pore opening,” *Nature*, vol. 381, no. 6580, pp. 295–298, 1996.

[14] S. Van Donk, A. H. Janssen, J. H. Bitter, and K. P. De Jong, “Generation, Characterization, and Impact of Mesopores in Zeolite Catalysts,” *Catal. Rev.*, vol. 45, no. 2, pp. 297–319, 2003.

[15] R. Chal, C. Gørardin, M. Bulut, and S. Van Donk, “Overview and Industrial Assessment of Synthesis Strategies towards Zeolites with Mesopores,” *ChemCatChem*, vol. 3, pp. 67–81, 2011.

[16] R. IUPAC, “Reporting physisorptiondatafor gas/solid systems with special reference to the determination of surface area and porosity,” *Pure Appl. Chem.*, vol. 57, no. 4, pp. 603–619, 1985.

[17] C. Xing *et al.*, “Tunable isoparaffin and olefin synthesis in Fischer–Tropsch synthesis achieved by composite catalyst,” *Fuel Process. Technol.*, vol. 136, pp. 68–72, 2015.

[18] E. G. Derouane *et al.*, “The Acidity of Zeolites: Concepts, Measurements and Relation to Catalysis: A Review on Experimental and Theoretical Methods for the Study of Zeolite Acidity,” *Catal. Rev. Sci. Eng.*, vol. 4, no. September, pp. 454–515, 2013.

[19] A. Corma, “Inorganic Solid Acids and Their Use in Acid-Catalyzed Hydrocarbon Reactions,” *Chem. Rev.*, vol. 95, no. 3, pp. 559–614, 1995.

[20] J. C. Groen, J. A. Moulijn, and J. Pérez-Rramirez, “Decoupling mesoporosity formation and acidity modification in ZSM-5 zeolites by sequential desilication – dealumination,” *Microporous Mesoporous Mater.*, vol. 87, no. 2, pp. 153–161, 2005.

[21] R. A. Van Santen, *Theory of Bronsted Acidity in Zeolites*, vol. 85. 1994.

[22] M. Gackowski, Ł. Kuterasi, J. Podobinski, B. Sulikowski, and J. Datka, “IR and NMR studies of hierarchical material obtained by the treatment of zeolite Y by ammonia solution,” *Spectrochim. Acta Part A Mol. Biomol. Spectrosc.*, vol. 193, pp. 440–446, 2018.

[23] W. Zhang and P. G. Smirniotis, “Effect of Zeolite Structure and Acidity on the Product Selectivity and Reaction Mechanism for n-Octane Hydroisomerization and Hydrocracking,” *J. Catal.*, vol. 182, no. 2, pp. 400–416, 1999.

[24] W. E. Farneth, “Methods for Characterizing Zeolite Acidity,” *Chem. Rev*, vol. 95, no. 3, pp. 615–635, 1995.

[25] Y.-Q. Song *et al.*, “Effect of variations in pore structure and acidity of alkali treated ZSM-5 on the isomerization performance,” *J. Mol. Catal. A Chem.*, vol. 310, no. 1–2, pp. 130–137, 2009.

[26] S. C. L. Dias and J. A. Dias, “Effects of the dealumination methodology on the FER zeolite acidity: A study with fractional factorial design,” *Mol. Catal.*, vol. 458, no. Part B, pp. 139–144, 2018.

[27] A. Corma, “From Microporous to Mesoporous Molecular Sieve Materials and Their Use in Catalysis,” *Chem. Rev.*, vol. 97, no. 6, pp. 2373–2419, 1997.

[28] M. Hartmann, G. Machoke, W. Schwieger, and M. Hartmann, “Catalytic test reactions for the evaluation of hierarchical zeolites,” *Chem. Soc. Rev.*, 2016.

[29] A. Feliczak-Guzik, “Hierarchical zeolites: Synthesis and catalytic properties,” *Microporous Mesoporous Mater.*, vol. 259, pp. 33–45, 2018.

[30] C. Tropp and M. Anbia, “Nanosized and hierarchical zeolites: A short review,” *Chinese J. Catal.*, vol. 37, no. 4, pp. 447–467, 2016.

[31] H. G. Karge and J. Weitkamp, *Molecular Sieves Science and Technology*, Springer-. 2006.

[32] Y. Wei, T. E. Parmentier, K. P. De Jong, and J. Zecevic, "Tailoring and visualizing the pore architecture of hierarchical zeolites," *Chem Son Rev*, vol. 44, pp. 7234–7261, 2015.

[33] D. P. Serrano, J. M. Escola, and P. Pizarro, "Synthesis strategies in the search for hierarchical zeolites," *Chem. Soc. Rev.*, vol. 42, pp. 4004–4035, 2013.

[34] J. Vernimmen, V. Meynen, and P. Cool, "Synthesis and catalytic applications of combined zeolitic/mesoporous materials," *Beilstein J. nanaotechnology*, vol. 2, pp. 785–801, 2011.

[35] C. J. H. Jacobsen, C. Madsen, J. Houzvicka, I. Schmidt, A. Carlsson, and D.- Lyngby, "Mesoporous Zeolite Single Crystals," *J. Am. Chem. Soc.*, vol. 122, no. 29, pp. 7116–7117, 2000.

[36] I. Schmidt, A. Boisen, E. Gustavsson, K. Ståhl, S. Pehrson, and S. Dahl, "Carbon Nanotube Templated Growth of Mesoporous Zeolite Single Crystals," *Chem. Mater*, vol. 13, no. 12, pp. 4416–4418, 2001.

[37] A. Boisen, I. Schmidt, A. Carlsson, S. Dalh, M. Brorson, and C. J. H. Jacobsen, "TEM stereo-imaging of mesoporous zeolite single crystals," *ChemComm*, pp. 958–959, 2003.

[38] C. Xing *et al.*, "A hierarchically spherical Co-based zeolite catalyst with aggregated nanorods structure for improved Fischer-Tropsch synthesis reaction activity and isoparaffin selectivity," *Microporous Mesoporous Mater.*, vol. 233, pp. 62–69, 2015.

[39] J. A. Schwarz, C. Contescu, and A. Contescu, "Methods for Preparation of Catalytic

Materials," *Chem. Rev.*, vol. 95, no. 3, pp. 477–510, 1995.

[40] S. T. F. Grecco, M. do C. Rangel, and ernesto A. Urquieta-Gonzalez, "Zeolitas Hierarquicamente Estruturadas," vol. 36, no. 1, pp. 131–142, 2013.

[41] Z. B. Wang, A. Kamo, T. Yonedaa, T. Komatsu, and T. Yashima, "Isomerization of n-heptane over Pt-loaded zeolite β catalysts," *Appl. Catal. A Gen.*, vol. 159, no. 1–2, pp. 119–132, 1997.

[42] J. Bao, G. Yang, C. Okada, Y. Yoneyama, and N. Tsubaki, "H-type zeolite coated iron-based multiple-functional catalyst for direct synthesis of middle isoparaffins from syngas," *Appl. Catal. A Gen.*, vol. 394, no. 1–2, pp. 195–200, 2011.

[43] A. Carvalho, M. Marinova, N. Batalha, N. R. Marcilio, A. Y. Khodakov, and V. V. Ordomsky, "Design of nanocomposites with cobalt encapsulated in the zeolite micropores for selective synthesis of isoparaffins in Fischer-Tropsch reaction," *Catal. Sci. Technol.*, vol. 7, no. 21, pp. 5019–5027, 2017.

[44] X. Meng, F. Nawaz, and F. S. Xiao, "Templating route for synthesizing mesoporous zeolites with improved catalytic properties," *Nano Today*, vol. 4, no. 4, pp. 292–301, 2009.

[45] Y. Yao, F. Cao, J. Gu, Y. Wu, Y. Zhou, and J. Wang, "Direct hydrothermal synthesis and characterization of framework-substituted Co(Mn)-Beta zeolites," *J. Porous Mater.*, vol. 20, no. 4, pp. 891–896, 2013.

[46] D. Farrusseng and A. Tuel, "Zeolite-Encapsulated Catalysts," in *Encapsulated Catalysts*, Elsevier, 2017, pp. 335–386.

[47] K. Zhang and M. L. Ostraat, "Innovations in hierarchical zeolite synthesis," *Catal. Today*, vol. 264, pp. 3–15, 2016.

[48] C. Flores, N. Batalha, N. R. Marcilio, V. V Ordomsky, and A. Y. Khodakov, "Influence of Impregnation and Ion Exchange Sequence on Metal Localization, Acidity and Catalytic Performance of Cobalt BEA Zeolite Catalysts in Fischer-Tropsch Synthesis," *ChemCatChem*, vol. 11, no. 1, pp. 568–574, 2019.

[49] D. P. Serrano, J. M. Escola, and P. Pizarro, "Synthesis strategies in the search for hierarchical zeolites," *Chem. Soc. Rev.*, vol. 42, no. 9, pp. 4004–4035, 2013.

[50] E. Koohsaryan and M. Anbia, "Nanosized and hierarchical zeolites: A short review," *Chinese J. Catal.*, vol. 37, pp. 447–467, 2016.

[51] J. M. E. and P. P. D. P. Serrano, "Synthesis strategies in the search for hierarchical zeolites," *Chem Soc Rev*, vol. 42, pp. 4004–4035, 2013.

[52] C. Flores *et al.*, "Versatile Roles of Metal Species in Carbon Nanotube Templates for the Synthesis of Metal-Zeolite Nanocomposite Catalysts," *ACS Appl. Nano Mater.*, vol. 2, no. 7, pp. 4507–4517, 2019.

[53] V. Subramanian *et al.*, "The role of steric effects and acidity in the direct synthesis of iso-paraffins from syngas on cobalt zeolite catalysts," *ChemCatChem*, vol. 8, no. 2, pp. 380–389, 2016.

[54] W. W. Liu, S. P. Chai, A. R. Mohamed, and U. Hashim, *Synthesis and characterization of graphene and carbon nanotubes: A review on the past and recent developments*, vol. 20, no. 4. The Korean Society of Industrial and Engineering Chemistry, 2014.

[55] Y. Zhai, Z. Zhu, and S. Dong, "Carbon-Based Nanostructures for Advanced Catalysis," *ChemCatChem*, vol. 7, no. 18, pp. 2806–2815, 2015.

[56] H. Xiong, M. A. M. Motchelaho, M. Moyo, L. L. Jewell, and N. J. Coville,

"Correlating the preparation and performance of cobalt catalysts supported on carbon nanotubes and carbon spheres in the Fischer – Tropsch synthesis," *J. Catal.*, vol. 278, no. 1, pp. 26–40, 2011.

[57] V. V Ordomsky, A. Y. Khodakov, B. Legras, and C. Lancelot, "Fischer-Tropsch synthesis on a ruthenium catalyst in two-phase systems: an excellent opportunity for the control of reaction rate and selectivity," *Catal. Sci. Technol.*, vol. 4, no. 9, pp. 2896–2899, 2014.

[58] M. E. Dry, "Present and future applications of the Fischer – Tropsch process," *Aplied Catal. A Gen.*, vol. 276, pp. 1–3, 2004.

[59] M. E. Dry, "The Fischer–Tropsch process: 1950–2000," *Catal. Today*, vol. 71, pp. 227–241, 2002.

[60] H. Schulz, "Short history and present trends of Fischer–Tropsch synthesis," *Appl. Catal.*, vol. 186, no. 1–2, pp. 3–12, 1999.

[61] Q. Zhang, W. Deng, and Y. Wang, "Recent advances in understanding the key catalyst factors for Fischer-Tropsch synthesis," *J. Energy Chem.*, vol. 22, no. 1, pp. 27–38, 2013.

[62] B. Jager and R. Espinoza, "Advances in low temperature Fischer-Tropsch synthesis," *Catal. Today*, vol. 23, no. 1, pp. 17–28, 1995.

[63] S. Sartipi, "Bifunctional catalysts for the direct production of liquid fuels from syngas," Delft University of Technology, 2014.

[64] E. Iglesia, "Design, synthesis, and use of cobalt-based Fischer-Tropsch synthesis catalysts," *Appl. Catal.*, vol. 161, no. 1–2, pp. 59–78, 1997.

[65] G. Jacobs, P. M. Patterson, Y. Zhang, T. Das, J. Li, and B. H. Davis, "Fischer–Tropsch

synthesis: deactivation of noble metal-promoted Co/ Al2O3 catalysts," *Appl. Catal.*, vol. 233, no. 1–2, pp. 215–226, 2002.

[66] C. K. Rofer-DePoorter, "A Comprehensive Mechanism for the Fischer-Tropsch Synthesis," *Chem. Rev.*, vol. 81, no. 5, pp. 447–474, 1981.

[67] R. A. van Santen, A. J. Markvoort, I. A. W. Filot, M. M. Ghouri, and E. J. M. Hensen, "Mechanism and microkinetics of the Fischer–Tropsch reaction," *Phys. Chem.*, vol. 15, no. 40, pp. 17038–17063, 2013.

[68] E. De Smit and B. M. Weckhuysen, "The renaissance of iron-based Fischer – Tropsch synthesis: on the multifaceted catalyst deactivation behaviour," *Chem. Soc. Rev.*, vol. 37, no. 12, pp. 2758–2781, 2008.

[69] V. M. H. van Wechem and M. M. G. Senden, "Cconversion of natural gas to transportation fuels via the shell middle distillate synthesis process (SMDS)," *Surf. Sci. Catal.*, vol. 81, no. C, pp. 43–71, 1994.

[70] M. Hillestad, "Modeling the Fischer–Tropsch Product Distribution and Model Implementation," *Chem. Prod. Process Model*, vol. 10, no. 3, 2015.

[71] I. Puskas and R. S. Hurlbut, "Comments about the causes of deviations from the Anderson–Schulz–Flory distribution of the Fischer–Tropsch reaction products," *Catal. Today*, vol. 84, no. 1–2, pp. 99–109, 2003.

[72] A. Y. Khodakov, W. Chu, and P. Fongarland, "Advances in the Development of Novel Cobalt Fischer−Tropsch Catalysts for Synthesis of Long-Chain Hydrocarbons and Clean Fuels," *Chem. Rev.*, vol. 107, no. 5, pp. 1692–1744, 2007.

[73] and A. I. T. F. King, E. Shutt, "Ruthenium Catalyst Systems for the Production of Hydrocarbons from Coal," *Platin. Met. Rev.*, vol. 29, no. 4, pp. 146–154, 1985.

[74] X. Wang and M. Economides, *Advanced Natural Gas Engineering*. 2013.

[75] A. de Klerk, *Fischer–Tropsch Refinin*. Wiley-VCH, 2012.

[76] R. C. B. I. and R. P. Pettit, "On the Mechanism of the Fischer-Tropsch Reaction. The Chain Propagation Step," *J. Am. Chem.*, vol. 103, no. 5, pp. 1287–1289, 1981.

[77] B. G. Henrici-Olivé and S. Olivé, "The Fischer-Tropsch Synthesis: Molecular Weight Distribution of Primary Products and Reaction Mechanism," *Angen Chrm Int Ed Engl*, vol. 15, no. 3, pp. 136–141, 1976.

[78] S. A. de Oliveira, "Estudo de adsorção de metais pesados em zeólitas para fins de uso em barreira reativa," Universidade Federal do Rio de Janeiro, 2011.

[79] J. Yang, Y. Qi, J. Zhu, Y.-A. Zhu, D. Chen, and A. Holmen, "Reaction mechanism of CO activation and methane formation on Co Fischer–Tropsch catalyst: A combined DFT, transient, and steady-state kinetic modeling," *J. Catal.*, vol. 308, pp. 37–49, 2013.

[80] J. Bao, J. He, Y. Zhang, Y. Yoneyama, and N. Tsubaki, "A Core/Shell Catalyst Produces a Spatially Confined Effect and Shape Selectivity in a Consecutive Reaction," *Angew. Chemie*, vol. 47, no. 2, pp. 353–356, 2008.

[81] J. Kang, S. Zhang, Q. Zhang, and Y. Wang, "Ruthenium Nanoparticles Supported on Carbon Nanotubes as Efficient Catalysts for Selective Conversion of Synthesis Gas to Diesel Fuel," *Angew. Chemie - Int. Ed.*, vol. 48, no. 14, pp. 2565–2568, 2009.

[82] K. Cheng *et al.*, "Mesoporous Beta Zeolite-Supported Ruthenium Nanoparticles for Selective Conversion of Synthesis Gas to C 5−C11 Isoparaffins," *ACS Catal.*, vol. 2, no. 3, pp. 441–449, 2012.

[83] S. Chen, J. Li, Y. Zhang, D. Zhang, and J. Zhu, "Effect of preparation method on

halloysite supported cobalt catalysts for Fischer-Tropsch synthesis," *J. Nat. Gas Chem.*, vol. 21, no. 4, pp. 426–430, 2012.

[84] Z. Xiaofeng, C. Qingling, T. Yuewu, and W. Huixin, "Influence of Ultrasound Impregnation on the Performance of Co/Zr/SiO2 catalyst during Fischer-Tropsch Synthesis," *Chinese J. Catal.*, vol. 32, no. 7, pp. 1156–1165, 2011.

[85] D. X. Martínez-Vargas *et al.*, "Recent Advances in Bifunctional Catalysts for the Fischer-Tropsch Process: One-Stage Production of Liquid Hydrocarbons from Syngas," *Ind. Eng. Chem. Res.*, vol. 58, no. 35, pp. 15872–15901, 2019.

[86] N. Egiebor and W. C. Cooper, "Synthesis of Motor Fuels from HY-Zeolite Supported Fischer-Tropsch Iron Catalysts," *Appl. Catal.*, vol. 55, no. 1, pp. 47–64, 1989.

[87] R. O. Idem, S. P. R. Katikaneni, R. Sethuraman, and N. N. Brakhshi, "Production of C4 Hydrocarbons from Modified Fischer-Tropsch Synthesis over Co-Ni-ZrO2/Sulfated-ZrO2 Hybrid Catalysts," *Energy & Fuels*, vol. 14, pp. 1072–1082, 2000.

[88] V. Subramanian *et al.*, "Nanoreactors: An Efficient Tool to Control the Chain-Length Distribution in Fischer-Tropsch Synthesis," *ACS Catal.*, vol. 6, no. 3, pp. 1785–1792, 2016.

[89] V. Evangelista, B. Acosta, S. Miridonov, E. Smolentseva, S. Fuentes, and A. Simakov, "Highly active Au-CeO2@ZrO2 yolk–shell nanoreactors for the reduction of 4-nitrophenol to 4-aminophenol," *Appl. Catal. B Environ.*, vol. 166–167, pp. 518–528, 2015.

[90] Y. Chen *et al.*, "Ruthenium silica nanoreactors with varied metal–wall distance for efficient control of hydrocarbon distribution in Fischer–Tropsch synthesis," *J. Catal.*,

vol. 365, pp. 429–439, 2018.

[91] Z. Li, L. Wu, D. Han, and J. Wu, “Characterizations and product distribution of Co-based Fischer-Tropsch catalysts: A comparison of the incorporation manner,” *Fuel*, vol. 220, pp. 257–263, 2018.

[92] C. Bouchy, G. Hastoy, E. Guillon, and J. A. Martens, “Fischer-Tropsch Waxes Upgrading via Hydrocracking and Selective Hydroisomerization,” *Oil Gas Sci. Technol. – Rev. IFP*, vol. 64, no. 1, pp. 91–112, 2009.

[93] A. Miyaji, T. Echizen, L. Li, T. Suzuki, Y. Yoshinaga, and T. Okuhara, “Selectivity and mechanism for skeletal isomerization of alkanes over typical solid acids and their Pt-promoted catalysts,” *Catal. Today*, vol. 74, no. 3–4, pp. 291–297, 2002.

[94] M. Steijns and G. F. Froment, “Hydroisomerization and Hydrocracking. 3. Kinetic Analysis of Rate Data for n-Octane,” *Ind. Eng. Chem. Prod. Res. Dev.*, vol. 20, pp. 660–668, 1981.

[95] J. Weitkamp, “Catalytic Hydrocracking-Mechanisms and Versatility of the Process,” *ChemCatChem*, vol. 4, no. 3, pp. 292–306, 2012.

[96] S. Bessell, “Support effects in cobalt-based Fischer-Tropsch catalysis,” *Appl. Catal. A Gen.*, vol. 96, no. 2, pp. 253–268, 1993.

[97] T. N. Phaahlamohlaka, D. O. Kumi, M. W. Dlamini, L. L. Jewell, and N. J. Coville, “Ruthenium nanoparticles encapsulated inside porous hollow carbon spheres : A novel catalyst for Fische –Tropsch synthesis,” *Catal. Today*, vol. 275, pp. 76–83, 2016.

[98] J. Kang *et al.*, “Mesoporous Zeolite-Supported Ruthenium Nanoparticles as Highly Selective Fischer–Tropsch Catalysts for the Production of C5– C11,” *Angew. Chemie - Int. Ed.*, vol. 50, no. 22, pp. 5200–5203, 2011.

[99] V. V. Ordomsky, A. Y. Khodakov, B. Legras, and C. Lancelot, “Fischer-Tropsch synthesis on a ruthenium catalyst in two-phase systems: An excellent opportunity for the control of reaction rate and selectivity,” *Catal. Sci. Technol.*, vol. 4, no. 9, pp. 2896–2899, 2014.

[100] E. Iglesia, S. L. Soled, R. A. Fiato, and G. H. Via, “Bimetallic Synnergy in Cobalt-Ruthenium Fischer-Tropsch Synthesis Catslysts,” *J. Catal.*, vol. 143, no. 2, pp. 345–368, 1993.

[101] L. Fan, K. Yokota, and K. Fujimoto, “Supercritical Phase Fischer-Tropsch Synthesis: Catalyst Pore-Size Effect,” *AIChE J.*, vol. 38, no. 10, pp. 1639–1648, 1992.

[102] M. A. Vannice and R. L. Garten, “The Influence of the Support in CO/H, on the Catalytic Behavior Synthesis Reactions of Ruthenium,” *J. Catal.*, vol. 63, pp. 255–260, 1980.

[103] L. Liu *et al.*, “Aqueous phase Fischer – Tropsch synthesis in a continuous flow reactor,” *Catal. Today*, vol. 183, no. 1, pp. 136–142, 2012.

[104] C. Giorgio, E. Tronconi, L. Lietti, R. Zennaro, and P. Forzatti, “Development of a complete kinetic model for the Fischer–Tropsch synthesis over Co/Al2O3 catalysts,” *Chem. Eng. Sci.*, vol. 62, pp. 5338–5343, 2007.

[105] S. Sun, N. Tsubaki, and K. Fujimoto, “The reaction performances and characterization of Fischer–Tropsch synthesis Co/SiO2 catalysts prepared from mixed cobalt salts,” *Appl. Catal.*, vol. 202, pp. 121–131, 2000.

[106] J. Li, L. Xu, R. Keogh, and B. Davis, “Fischer -Tropsch synthesis. Effect of CO pretreatment on a ruthenium promoted Co/TiO2,” *Catal. Letters*, vol. 70, pp. 127–130, 2000.

[107] J. T. Miller, E. Glusker, R. Peddi, T. Zheng, and J. R. Regalbuto, “The role of acid sites in cobalt zeolite catalysts for selective catalytic reduction of NOx,” *Catal. Letters*, vol. 51, pp. 15–22, 1998.

[108] C. Flores *et al.*, “Direct Production of Iso-Paraffins from Syngas over Hierarchical Cobalt-ZSM-5 Nanocomposites Synthetized by using Carbon Nanotubes as Sacrificial Templates,” *ChemCatChem*, vol. 10, no. 10, pp. 2291–2299, 2018.

Chapter 2. Experiment Section

2.1 Catalyst preparation

2.1.1 CNT based catalysts

The treatment of CNT was according to previous literature [1], [2]. The carbon nanotubes (CNT, Iolite nanomaterial, 95%, outer diameter of 20-40 nm) were treated with nitric acid to remove contaminations with metal and to make CNT hydrophilic. The hydrophilicity of CNT makes it easier for impregnation in aqueous solutions. The oxygen-containing groups also help to anchor the cations in the surface of CNT and then to reduce sintering during the calcination. Firstly, 3 g of CNT were pretreated in concentrated HNO_3 (68%) in 210 mL during 10 h under reflux conditions. After, the samples were filtered, washed with distilled water until pH equal to 7 and dried at 100 ºC overnight.

The catalysts were prepared by incipient wetness impregnation of the CNT. Ruthenium (or cobalt) was introduced to CNT using respectively aqueous solutions of cobalt nitrate ($Co(NO_3)_2 \cdot 6H_2O$, Sigma-Aldrich, 98%) and ruthenium chloride ($RuCl_3 \cdot H_2O$, ACROS Organics, 35-40%). The precursor amount was estimated to obtain a final composition of 20 wt.% Co and 10 wt.% Ru. Typically, 50 mL of $Co(NO_3)_2$ or $RuCl_3$ solution were used per gram of CNT. The mixture was submitted to ultrasonic treatment overnight, keep for 4 h, dried 3 h under bath water at 70 °C and dried at 80 °C overnight. The aqueous solution was drawn into the CNT channels by capillary forces aided by ultrasonic treatment and stirring to obtain confined catalysts. The samples were calcined at 400 °C for 4 h under nitrogen flow (50 mL/min).

After calcination, the impregnated CNT were treated with H_2O_2 to restore the hydrophilic properties of the CNTs. 30 mL of 1:1 H_2O_2 (Sigma-Aldrich, 35%) and distilled water were added to the impregnated CNTs, sonicated for 30 min and dried at 80 °C.

The ZSM-5 zeolite was synthesized by using the following initial composition of the gel: $2.7NaCl:1Al_2O_3:12.5TPAOH:55.8SiO_2:7500H_2O$. 0.380 g of sodium chloride (Janssen Chimica, P.A.), 3.0 g of tetrapropylammonium hydroxide (Sigma-Aldrich, 1M in H_2O), 0.040 g of sodium aluminate (Sigma-Aldrich) and distilled water were mixed until a clear solution was obtained. Then, 0.240 g of Ru/CNT and 2.8 g of tetraethyl-orthosilicate (TEOS, Sigma-Aldrich, 99%) were added to the solution. After, the synthesis gel was aged for 1 h at room temperature under stirring. The synthesis gel was set inside a Teflon-lined autoclave (40 mL) and the ZSM-5 crystallization was performed under the static condition at 170°C for 24 h. After cooling down, the solid was recovered by filtration and washed until neutral pH [3].

BEA zeolite was synthesized by the initial composition of the gel: $1.970Na_2O:1.00K_2O:12.5(TEA)_20:Al_2O_3:50SiO_2:750H_2O:2.9HCl$. Typically, 59.4 g of water, 89.6 g of tetraethylammonium hydroxide (TEAOH, Sigma-Aldrich, 40%), 0.53 g of sodium chloride and 1.44 g of potassium chloride were stirred until dissolved. Then, 29.54 g of silica (Degussa Aerosil 200, 99+% SiO_2) were added. A second solution was prepared by add 20.0 g of water, 0.33 g of sodium hydroxide, 1.79 g of sodium aluminate and stirred until dissolved. The two solutions and Co/CNT or Ru/CNT were mixed for 10 minutes and a thick gel was obtained. The crystallization was performed in a Teflon-lined autoclave (40 mL) at 135 °C for 20 h. After cooling down, the solid was recovered by centrifugation, washed until pH ~9 and dried overnight at 77 °C [4]. The catalysts prepared using Ru/CNT and Co/CNT

as secondary templates, are designated as RuCNT/BEA, RuCNT/ZSM-5, and CoCNT/BEA.

The catalysts were calcined at 500 °C for 4 h under air in order to eliminate CNTs. The schema of synthesis of metal-zeolite nanocomposites is shown in Figure 2.1. Thermogravimetric analysis showed complete decomposition of carbon nanotubes at temperatures below 400 °C. This suggests that cobalt and ruthenium zeolite composites catalysts calcined at 500 °C in air did not contain any residual carbon species.

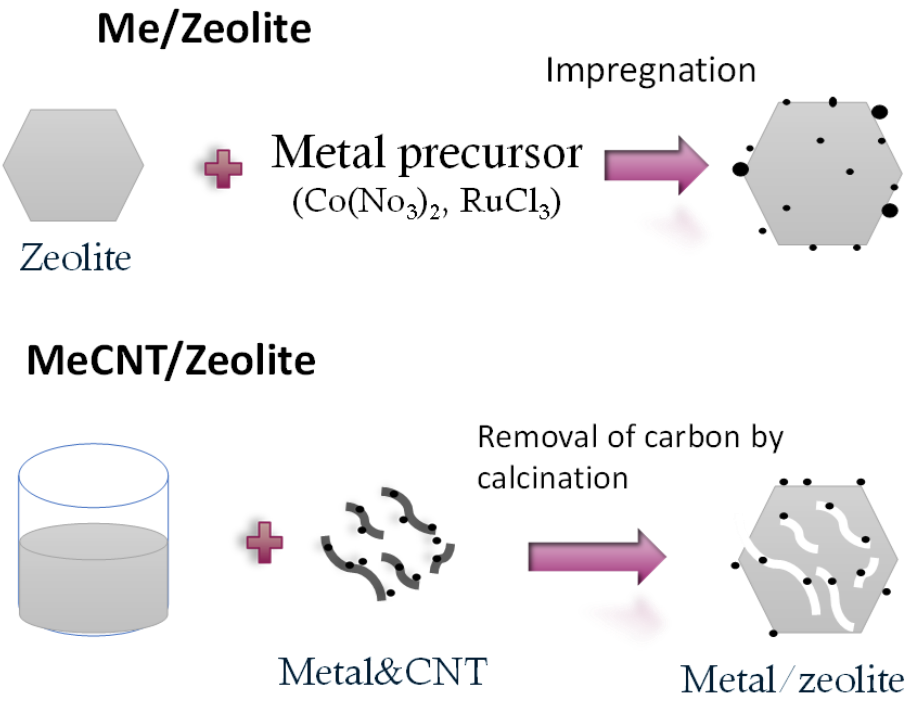

Figure 2.1. Schema of synthesis of metal zeolite catalysts.

To compare, zeolite syntheses without addition of metal/CNT were performed. The synthesized zeolites were impregnated with cobalt or ruthenium precursors in the final catalysts. In order to obtain the zeolite acid form, two successive exchanges using 2 M NH_4NO_3 aqueous solution at 80 °C for 1 h (1 g of catalyst per 50 mL of solution) were performed. The ammonium form was converted into the protonic form by calcination at

450 °C for 4 h under air [5]. The catalysts prepared using impregnation are labeled as Co/BEA, Ru/BEA, and Ru/ZSM- 5.

2.1.2 Catalytic tests

The catalytic performance of the samples was tested in FT synthesis. The experiments were performed in a milli-fixed bed reactor. Prior to testing, the samples were reduced in situ in pure H_2 gas flow (3 mL min^{-1}) at 400 °C for 4 h with a heating rate of 3 °C min^{-1}. Then, the reactor was cooled down to room temperature, the flow switched to syngas ($H_2/CO = 2$) and the pressure adjusted to 20 bar. The flow was adjusted to obtain a GHSV of 20-70 L/g_{Co} h. Nitrogen (2 cm^3 min^{-1}) was used has the internal standard. After achieving the desired pressure, the temperature was progressively increased to the reaction temperature, i.e. 250 °C, at a rate of 3 °C min^{-1}. The reaction was conducted at 250 °C in order to create in addition to FT synthesis, favorable conditions for the acid-catalyzed reactions, such as olefin cracking and isomerization. The gas hourly space velocity (GHSV) was expressed in cm^3 g_{cat}^{-1} h^{-1}. The units correspond to the volume of syngas, which passed through 1 g of catalyst per hour. The reaction products were analyzed using gas-chromatography (GC×FID/TCD, Scion, GC-456). FT reaction rates were calculated as moles of CO, converted per gram of catalyst per second.

2.1.3 Synthesis of core-shell metal zeolite composite catalysts

A different synthetic strategy for the preparation of hierarchical metal and zeolite nanocomposite catalysts was performed. The nanocomposites were synthesized in three

steps. In the first step, the parent (core) zeolite is etched with an ammonium fluoride solution. The etching creates small mesopores inside the zeolite crystals. In the second step, the Ru nanoparticles prepared using water-in-oil microemulsion are deposited in the mesopores of the zeolite. In the third step, a zeolite shell of MFI-type zeolites (silicalite-1 or ZSM-5) is grown on the parent zeolite crystals containing of both the etched surface and metallic nanoparticles.

Two different parent zeolites were used for the preparation of the metal zeolite composite catalysts. A sample of ZSM-5 zeolite (MFI structure) with Si/Al = 21 was obtained from Süd-Chemie in the NH_4^+ form, and silicalite-1 (S-1, purely siliceous MFI zeolite) was synthesized as follows: 114 mL of 1 M solution of tetrapropylammonium hydroxide (TPA−OH, Alfa Aesar) was diluted with 97.8 g of distilled water, and subsequently, 65.1 g of Ludox HS-30 colloidal silica (30 wt % of SiO_2, Sigma-Aldrich) was added dropwise under vigorous stirring.

For the etching, a 40 wt % solution of NH_4F was prepared from 80.0 g of NH_4F (98%, Sigma- Aldrich) and 120.0 g of distilled water [6]. The solution was preheated to 50 °C (± 2 °C) in the 40 kHz ultrasonic bath in an open vessel equipped with a mechanical stirrer. Then, 10 g of the parent zeolite was introduced into the solution under stirring and ultrasound radiation. The etching occurred for 30 min (ZSM-5) or 13 min (S-1) under the above conditions. After the given time, the suspension was quickly filtered on a Buchner funnel and washed several times with distilled water (about 500 mL all together). The solid product was dried at 90 °C.

Before use, the etched ZSM-5 was ion-exchanged into Na_+ form, using 1 M solution of $NaNO_3$ for 4 h at room temperature. The procedure was repeated 4 times as 100 mL of

solution per 1 g of zeolite was used. After the treatment, the zeolite was filtered, washed twice with 100 mL/g of water, and dried at room temperature. The etched S-1 was used without any further pretreatment. The Ru/ZSM-5 and Ru/S-1 labels correspond to the etched zeolites.

To prepare the Ru nanoparticles, a two microemulsion system was used [7]. Microemulsion I: 3.00 g of hexadecyltrimethylammonium bromide (CTABr, 96%, Sigma-Aldrich), 5.00 g of 1-hexanol (98%, Sigma-Aldrich), and 2 g of 0.5 M aqueous solution of $RuCl_3$ (Ru content 45−55%, Sigma-Aldrich). Microemulsion II: 3.00 g of CTABr, 5.00 g of 1-hexanol, and 2 g of 1.5 M aqueous solution of $NaBH_4$ (96%, Sigma-Aldrich). Both microemulsions were homogenized for 30 min, and subsequently, emulsion II was added dropwise into emulsion I under vigorous stirring (750 rpm). The combined emulsions were stirred for another 30 min to finish the reduction. Then 500 mg of the etched zeolite was added, and stirring was continued for another 2 h. After this time, the emulsion was diluted with about 20 mL of ethanol (96%) filtered and the solid black product was washed with ethanol and subsequently with water (about 200 mL of each). Finally, the product was dried at ambient temperature and subjected to the overgrowing or calcined in static air at 480 °C for 5 h with temperature ramp 2 °C/min.

The Ru-zeolite catalyst was then coated with the S-1 or ZSM-5 shell. For the preparation of S-1 shell, a coating solution with a molar composition of 12 TPA−OH: 100 SiO_2: 5800 H_2O was prepared from 1 M TPA−OH solution, tetraethyl orthosilicate (98%, Sigma-Aldrich), and distilled water. After mixing all the three components, the mixture was stirred overnight to obtain a clear homogeneous solution. This solution was combined with the non-calcined product of the insertion step using 25 g of

solution/1 g of the material after insertion. The overgrowing solution and etched zeolite were stirred together for 2 h and then subjected to the secondary zeolite crystallization in a tumbling Teflon-lined autoclave (50 rpm) at 150 °C for 15 h. After the given time, the crude product was filtered, washed with distilled water, dried at ambient temperature, and calcined in static air starting at 110 °C for 2 h and then at 480 °C for 5 h with a temperature ramp 2 °C/min.

The ZSM-5 shell was crystallized from a coating solution with a molar composition of 25 TPA-OH: 100 SiO_2:3.33 $Al(OH)_3$: 5800 H_2O (Si/Al = 30). It was prepared from 1 M TPA−OH solution, tetraethyl orthosilicate (98%, Sigma-Aldrich), aluminum hydroxide (Aldrich) and distilled water. The solution was stirred overnight to obtain clear homogeneous solution. The coating procedure was the same as described above for S-1 shell with the exception that crystallization of the shell occurred at 140 °C for 4 h. After workup of the coating mixtures, the samples were calcined in static air starting at 110 °C for 2 h and then at 480 °C for 5 h with a temperature ramp 2 °C/min.

The NH_4^+ form was obtained by four-stage treatment with 1 M NH_4NO_3 solution (100 mL/g of zeolite, 4 h each time) and converted into H^+ form by calcination at 450 °C for 2 h (ramp 2 °C/min).

2.1.4 Catalytic Testing

Carbon monoxide hydrogenation (Fischer−Tropsch reaction) was carried out on REALCAT platform in a Flowrence high-throughput unit (Avantium) equipped with 16 parallel milli-fixed-bed reactors (d = 2 mm) operating at the pressure of 20 bar, H_2/CO = 2 molar ratio, T = 220 °C and GHSV from 4.8−6.5 L h^{-1} $gcat^{-1}$. The catalyst loading was 50 mg

per reactor. Prior to the catalytic test, all the samples were activated in a flow of hydrogen at atmospheric pressure during 10 h at 400 °C. During the activation step, the temperature ramp was 3 °C/min. After the reduction, the catalysts were cooled down to 180 °C, and a flow of premixed syngas was gradually introduced to the catalysts. When the reactor attained required pressure, the temperature was slowly increased to the temperature of the reaction. The reaction has been conducted for 60 h at different GHSV of syngas. Gaseous reaction products were analyzed by online gas chromatography. The analysis of permanent gases was performed using a Molecular Sieve column and a thermal conductivity detector. The C_1−C_4 hydrocarbons were separated in a PPQ column and analyzed by a thermoconductivity detector. The C_5−C_{12} hydrocarbons were analyzed using a CP-Sil5 column and a flame-ionization detector. The carbon monoxide contained 5% of helium, which was used as an internal standard for calculating carbon monoxide conversion. The product selectivity (S) was reported as the percentage of CO converted into a given product and expressed on carbon basis.

2.1.5 Core-shell ZSM-5/Ru/ZSM-5 catalyst for dispersion study

A microemulsion system is a thermodynamically stable dispersion of two immiscible liquids, hexanol and water, stabilized by the surfactant CTAB. A water-in-oil microemulsion is formed when tiny water droplets are dispersed in a continuous phase of hexanol. The microemulsions exist in a certain compositional range in the phase diagram of hexanol-CTAB-water (Figure 2.2) [8]. It is possible to control the size of the microemulsions by controlling the amount of water [9], [10]. A decrease in the amount of aqueous phase in microemulsion leads to different sizes of micelle [11], [12]. Additionally, the less amount of

water present in the microemulsion leads to a smaller metal particle size [11]. Metal-zeolite composites have been produced using this strategy.

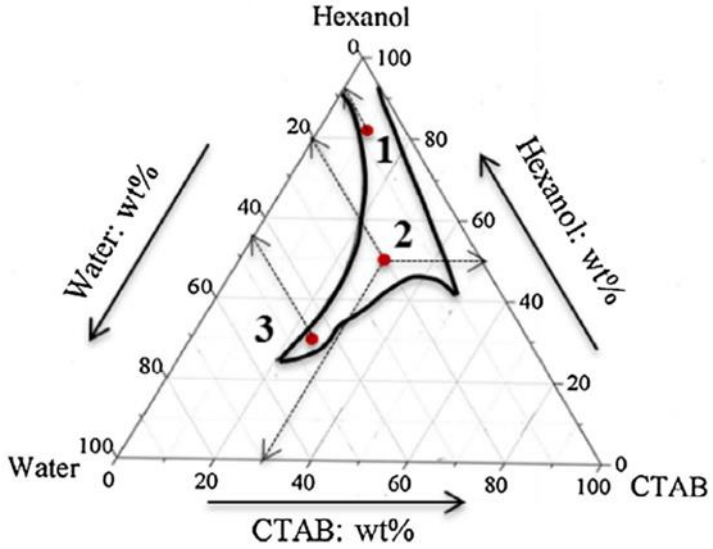

Figure 2.2. Phase diagram for CTAB/hexanol/water systems.

A Zeolyst parent zeolite has been used for synthesis of the zeolite composites catalysts. A sample of ZSM-5 zeolite (MFI structure) with SiO_2/Al_2O_3 = 23 was obtained from Zeolyst International in the NH_4^+ form. First of all, the conventional catalyst has been prepared by impregnation of $RuCl_3$ with subsequent calcination and reduction (Ru/ZSM-5). The synthesis of the composite catalysis by microemulsion is composed of 3 steps (Figure 2.3). The first step is the preparation of ruthenium nanoparticles by a microemulsion method as described in [13] and their insertion into the zeolite. Second step is the washing for micro-emulsion removal. The third step (overgrowing), the zeolite shell crystallize on the surface of parent crystals covering both parent zeolite and metallic nanoparticles which become trapped inside the zeolite matrix.

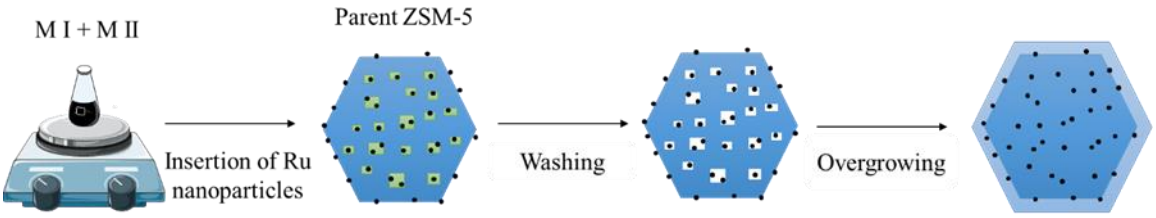

Figure 2.3. Synthesis of Ru-zeolite composite catalysts.

For comparison, impregnation by conventional method and an overgrowing were performed.

Ruthenium nanoparticles were prepared by a microemulsion method. Initially, two micro-emulsions were prepared. Micro-emulsion I was prepared from 1.00 g of hexadecyltrimethylammonium bromide (CTABr, 99%, Sigma-Aldrich), 8.2 g of 1-hexanol (98%, Sigma-Aldrich) and 0.8 g of 0.5 M aqueous solution of $RuCl_3$ (Ru content 35-40%, ACROS Organics). Micro-emulsion II was composed of 1.00 g of CTABr, 8.2 g of 1-hexanol and 0.8 g of 1.5 M aqueous solution of $NaBH_4$ (96%, Sigma-Aldrich). Both micro-emulsions were homogenized for 30 min and subsequently emulsion II was added dropwise into emulsion I under vigorous stirring (1000 rpm). The combined emulsions were stirred for another 30 min to finish the reduction and then 500 mg of zeolite in H^+ form was added and stirring continued for another 2 h. After this time the emulsion was diluted with about 50 ml of ethanol (96%) filtered and the solid black product was washed with ethanol and subsequently with water (about 500 ml of each). Finally, the product was dried at 120 °C and subjected to the overgrowing or calcined in air at 550 °C for 6 h with temperature ramp 3 °C/min.

The ZSM-5 shell was crystallized from an overgrowing solution with a molar composition of $2.7NaCl:1Al_2O_3:12.5TPAOH:55.8SiO_2:7500H_2O$. It was prepared 0.380 g of

sodium chloride (Janssen Chimica, P.A.), 3.0 g of tetrapropylammonium hydroxide (Sigma-Aldrich, 1M in H_2O), 0.040 g of sodium aluminate (Sigma-Aldrich) and distilled water mixed until a clear solution was obtained. Next, 2.8 g of tetraethyl-orthosilicate (TEOS, Sigma-Aldrich, 99%) were added to the solution and the synthesis gel was aged for 1 h at room temperature under stirring. This solution was combined with the non-calcined product of the insertion step in order to obtain 1:1 of solution/material after insertion, stirred for 2 h and subjected to the overgrowing in a Teflon-lined autoclave at 170°C for 24 h. After the given time, the crude product was filtered, washed with distilled water, dried at 120 °C and calcined in air at 550°C for 6 h.

In order to obtain the zeolite acid form, two successive exchanges using 2 M NH_4NO_3 aqueous solution at 80 °C for 1 h (1 g of catalyst per 50 mL of solution) were performed. The ammonium form was converted into the protonic form by calcination at 450 °C for 4 h under air [14].

2.2 Catalyst Characterization

The samples were characterized by X-ray diffraction (XRD) by using a D8 Advance diffractometer equipped with an energy dispersive type detector and a monochromatic CuKα radiation source. The samples were analyzed using a step of 0.02° with an acquisition time of 0.5 s. The crystalline phases were identified by comparing the diffraction patterns with those of the standard powder XRD files (JCPDS) published by the International Center for Diffraction Data. The average size of metal oxides crystallites was determined by the Scherrer equation. Scanning electron microscopy (SEM) images were collected on a MIRA

TESCAN microscope equipped with a field emission gun. The images were collected with an acceleration voltage of 30 kV.

The sample chemical composition was determined by X-ray fluorescence (XRF) on a spectrometer M4 TORNADO (Bruker). This instrument is equipped with two anodes: a rhodium X-ray tube 50 kV/600 mA (30 W) and a tungsten X-Ray tube 50 kV/700 mA (35 W). For sample characterization, the rhodium X-rays with a poly-capillary lens enabling excitation of an area of 200 μm were used. The detector used was a Silicon-Drift-Detector Si (Li) with <145 eV resolution at 100,000 cps (Mn Kα) and cooled with a Peltier cooling (253 K). The measurement was done under vacuum (20 mbar). The elements, that can be measured by this instrument unit range from sodium (Na) to uranium (U). Quantitative analysis was performed using a fundamental parameter (FP) (standardless).

The textural properties of the samples were determined by N_2 physisorption on a Micromeritics ASAP 2000 apparatus. Prior to analysis, the samples were degassed under vacuum (10 μm Hg) at 350 °C for 4 h. The total pore volume (TPV) was calculated from the amount of vapor adsorbed at a relative pressure $P/P_0 = 0.97$. The samples surface area was estimated by the BET method, while the micropore volume and external surface were calculated using the deBoer t-plot method.

The high-resolution transmission electron microscopy (HRTEM) was performed with two different machines. A part of the images was collected using a Tecnai instrument, equipped with a LaB6 crystal, operating at 200 kV. Prior to the analysis, the samples were dispersed by ultrasound in ethanol solution for 5 min, and a drop of solution was deposited onto a carbon membrane on a 300 mesh-copper grid. The other machine was a Jeol JEM-2011 microscope operating at the accelerating voltage of 200 kV. The HRTEM images were

recorded with a Gatan 794 CCD camera. The camera length, sample position, and magnification were calibrated using standard gold film methods.

The catalyst reducibility was studied using temperature-programmed reduction (TPR) system with an Autochem II (Micrometrics) apparatus. 0,05 g of the samples were reduced under a flow of 5 vol. % H_2 in argon (50 mL min-1) and heated up to 800 °C at a rate of 5 °C/min.

The concentration of acid sites was determined from pyridine titration using IR spectroscopy. The individual samples were diluted 3 times with silica (Aldrich) to maintain sufficient transparency, pressed into self-supporting wafers with a density of 8.0−12 mg/cm^2, and activated at 450 °C for 5 h with a temperature ramp 2 °C/min under vacuum of turbomolecular pump (final pressure 1.0−1.5 × 10^{-6} Torr). The amount of acid sites was determined from adsorption/desorption of pyridine (Py) at 150 °C. Adsorption occurred for 30 min at partial pressure 1 Torr, followed by desorption at 150 °C for 15 min under vacuum of turbomolecular pump. This time is sufficient to stabilize amount of adsorbed pyridine. The spectra were collected with a Thermo Scientific Nicolet 6700 FT-IR spectrometer at 4 cm^{-1} optical resolution by collecting 128 scans for a single spectrum. The spectra intensities were recalculated to a wafer density of 10 mg/cm^2. The concentrations of acid sites were determined from integral intensities of bands at 1454 cm^{-1} (Lewis) and at 1545 cm^{-1} (Brønsted acid sites) using extinction coefficients, ε(L) = 1.28 cm/μmol, and ε(B) = 1.13 cm/μmol [14].

2.3 References

[1] W. Chen, Z. Fan, X. Pan, and X. Bao, “Effect of confinement in carbon nanotubes on the activity of Fischer-Tropsch iron catalyst,” J. Am. Chem. Soc., vol. 130, no. 29, pp. 9414–9419, 2008.

[2] X. Pan, Z. Fan, W. Chen, Y. Ding, H. Luo, and X. Bao, “Enhanced ethanol production inside carbon-nanotube reactors containing catalytic particles,” Nat. Mater., vol. 6, no. 7, pp. 507–511, 2007.

[3] C. Flores et al., “Direct Production of Iso-Paraffins from Syngas over Hierarchical Cobalt-ZSM-5 Nanocomposites Synthetized by using Carbon Nanotubes as Sacrificial Templates,” ChemCatChem, vol. 10, no. 10, pp. 2291–2299, 2018.

[4] N. Mintova, S and Barrier, “Verified Syntheses of Zeolitic Materials, Synthesis Commission of IZA, Third. 2016.”

[5] C. Flores, N. Batalha, N. R. Marcilio, V. V Ordomsky, and A. Y. Khodakov, “Influence of Impregnation and Ion Exchange Sequence on Metal Localization, Acidity and Catalytic Performance of Cobalt BEA Zeolite Catalysts in Fischer-Tropsch Synthesis,” ChemCatChem, vol. 11, no. 1, pp. 568–574, 2019.

[6] Z. Qin et al., “The mosaic structure of zeolite crystals,” Angew. Chemie - Int. Ed., vol. 55, no. 48, pp. 15049–15052, 2016.

[7] V. Subramanian et al., “Nanoreactors: An Efficient Tool to Control the Chain-Length Distribution in Fischer-Tropsch Synthesis,” ACS Catal., vol. 6, no. 3, pp. 1785–1792, 2016.

[8] Y. Chen et al., “Ruthenium silica nanoreactors with varied metal–wall distance for efficient control of hydrocarbon distribution in Fischer–Tropsch synthesis,” J. Catal., vol. 365, pp. 429–439, 2018.

[9] S. A. Safran, L. A. Turkevich, and P. Pincus, “Cylindrical microemulsions: a

polymer-like phase?," J. Phys. Lettres, vol. 45, no. 2, pp. 69–74, 1984.

[10] M. P. Pileni and J. Tanori, "Colloidal assemblies used as templates to control the size, shape and self-organization of nanoparticles," Supramol. Sci., vol. 5, no. 3–4, pp. 321–329, 1998.

[11] Y. Chen et al., "Ruthenium silica nanoreactors with varied metal–wall distance for efficient control of hydrocarbon distribution in Fischer–Tropsch synthesis," J. Catal., vol. 365, pp. 429–439, 2018.

[12] B. K. Fontell, "Micellar behaviour in solutions of bile-acid salts," Kolloid-Z. u. Z. Polym., vol. 246, pp. 614–625, 1971.

[13] V. Subramanian et al., "Nanoreactors: An Efficient Tool to Control the Chain-Length Distribution in Fischer-Tropsch Synthesis," ACS Catal., vol. 6, no. 3, pp. 1785–1792, 2016.

[14] F. Ngoye et al., "Mitigating coking during methylcyclohexane transformation on HZSM-5 zeolites with additional porosity," J. Catal., vol. 320, no. 1, pp. 118–126, 2014.

Chapter 3. Design of ruthenium-zeolite nanocomposites for enhanced hydrocarbon synthesis from syngas

Abstract

The purpose of this work is the design of metal-zeolite nanocomposite catalysts for Fischer-Tropsch synthesis, containing ruthenium nanoparticles uniformly distributed in the hierarchical BEA zeolites. Use The use of ruthenium avoids the formation of inert hardly reducible inert metal silicates and metal aluminates. Carbon nanotubes with supported metal oxide nanoparticles play a role of sacrificial template, which allows creating mesoporosity and bringing metallic functionality inside the zeolite matrix. Both mesoporosity and larger micropores of the BEA zeolite facilitate the localization of metal nanoparticles within the zeolite structure and diffusion of the reacting molecules. Compared to the conventional zeolite supported metal catalysts, the synthesized hierarchical ruthenium-zeolites exhibited much higher activity and lower methane selectivity in Fischer-Tropsch synthesis.

3.1 Introduction

Metal-zeolite nanocomposite catalysts [1]–[5] have found numerous applications in heterogeneous catalysis: hydrocarbon hydrocracking, reforming, dewaxing, hydroisomerization of alkanes and aromatics, and biomass-related reactions. Recently, the zeolite nanocomposite catalysts were proposed for selective synthesis of light olefins from syngas via OX-ZEO approach [6]–[11]. The metal zeolite nanocomposites provide an opportunity for the synthesis of highly dispersed metal species, uniformly distributed within

the zeolite [1], [12]. Combining metal and acid functions allows conducting multiple catalytic reactions, which are unachievable on only zeolite and metal catalysts. The reaction rate and selectivity over metal-zeolite nanocomposites are functions of the number, localization, accessibility and proximity of metal and acid sites [13], [14]. Non-uniform distribution of metal species in zeolite, diffusion limitations due to the small zeolite pores, formation of barely reducibly metal silicates or metal aluminates, are major drawbacks for the design of efficient metal zeolite catalysts.

Fischer–Tropsch (FT) synthesis is a promising process for the environmental-friendly industrial production of ultraclean synthetic fuels from syngas [7], [15]–[18]. The syngas (H_2 + CO) obtained by gasification of biomass, organic or plastic wastes, enables valorization of sustainable feedstocks into valuable chemicals and fuels. FT reaction occurs on supported metals of VIII group, such as iron, nickel, cobalt or ruthenium, preferably dispersed as nanoparticles over porous supports. Cobalt shows high activity and selectivity for long-chain hydrocarbons, lower water gas shift reaction activity than iron [19], [20]. Nickel catalysts under practical conditions produce too much methane [17]. Ruthenium, although more expensive than cobalt and iron possesses several advantages for FT synthesis, as higher catalytic activity, higher selectivity to long-chain hydrocarbons, higher stability and capacity to operate in the presence of large amounts of water [21]. In particular, different to cobalt, nickel and iron, very few amounts of hardly reducible inert metal-support compounds such as silicate and aluminate [15], [22]–[24] are present in the ruthenium-containing catalysts.

Recently, we proposed [25], [26] a new method for the design of metal-zeolite hierarchical nanocomposites with specific shape, enhanced mesoporosity and uniform distribution of highly dispersed metals within the zeolite crystals. This method involves using

carbon nanotubes (CNT) containing metal oxide nanoparticles as a secondary hard template. We uncovered [26] multiple roles of these templates in the zeolite synthesis. First, metal-CNT create zeolites with specific fibrous morphology. Second, they markedly increase the zeolite secondary porosity. Finally, they uniformly introduce the metal nanoparticles inside the mesoporous zeolites. The possibilities of this new method have been demonstrated so far [26] using as secondary templates CNT with cobalt, nickel and magnesium oxide nanoparticles. Note that strong interaction and proximity of metal oxide species and zeolite under the hydrothermal conditions of zeolite synthesis have led to the occurrence of metal silicates or metal aluminates. These compounds have low reducibility and they are inactive in FT synthesis and many other metal-catalyzed reactions. The presence of a major fraction of irreducible metal silicate and aluminate species in the synthesized metal-zeolite nanocomposites prevented the most efficient use of this new method for the design of metal-zeolite catalysts with enhanced activity.

In this work, we synthetized highly dispersed ruthenium metallic species in the hierarchical BEA zeolite. Ruthenium is a noble metal; it has easier reducibility and does not tend to form inert and barely reducible aluminates and silicates compared to cobalt. The 12-member ring BEA zeolite has larger micropores (0.76×0.64 nm) compared to 10-membered ring ZSM-5 zeolite (dp~0.55 nm). In addition to mesoporosity, larger micropores of the BEA zeolite may facilitate the localization of metal nanoparticles within the zeolite and the diffusion of reacting molecules. Using both ruthenium and BEA zeolite may allow, therefore, achieving all benefits of metal zeolite hierarchical nanocomposites prepared using metal-CNT as templates and producing much more active catalysts for FT synthesis, compared to

previous reports. The synthesized nanocomposites were characterized using a combination of techniques. Their performance was evaluated in a fixed bed reactor and compared with the metal zeolite catalysts prepared by conventional impregnation.

3.2 Results and Discussion

3.2.1 Catalyst characterization

The nitrogen adsorption–desorption isotherms of the metal zeolite catalysts are shown in Figure 3.1. The isotherm of BEA zeolite is characteristic of microporous material (Figure 3.1a). The slight increase in the N_2 uptake at high P/P_0 may result from nitrogen adsorption in the voids between the BEA zeolite crystallites. A similar shape of the isotherm of BEA zeolite was observed in previous reports [14]. The nitrogen update at higher P/P_0 values, slightly increases for the Co/BEA and Ru/BEA zeolites, prepared by impregnation. This corresponds to the appearance on metal oxide nanoparticles in the zeolites and the contribution of nitrogen intraparticle adsorption. A major increase in adsorption at higher P/P_0 occurs for CoCNT/BEA and RuCNT/BEA samples. This increase probably corresponds to the creation of zeolite mesopores during the hydrothermal synthesis, using metal-CNT secondary templates. The CNT removal during catalyst calcination makes these mesopores available for N_2 adsorption. Similar phenomena are observed for ruthenium ZSM-5 catalysts (Figure 3.1b). The Ru/ZSM-5 sample prepared by impregnation remains to a larger extent, a microporous solid with very small contribution of mesoporosoity. The addition of Ru/CNT as secondary template during the zeolite synthesis, results in a major increase in the nitrogen update at higher P/P_0 which is indicating of the built-up of zeolite mesoporosity.

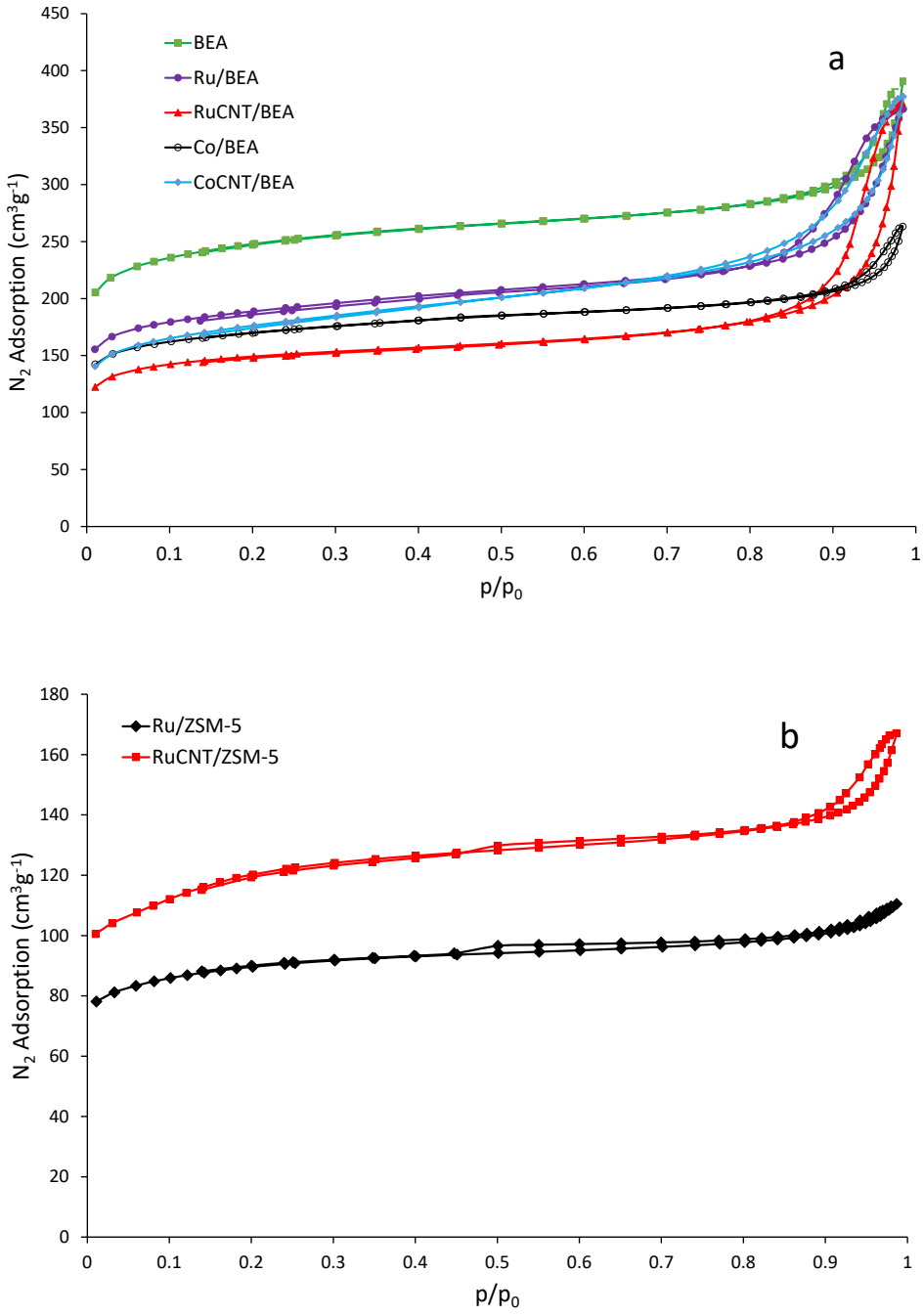

Figure 3.1. Low temperature nitrogen adsorption-desorption isotherms over metal zeolite catalysts.

The catalyst textural properties are summarized in Table 3.1. The introduction of Co/CNT during the BEA zeolite synthesis leads to an increase in the surface area, compared

with the Co/BEA catalyst, while the mesoporous volume increases almost twice. This variation is possibly due to creating mesoporosity via removal of CNTs incorporated inside the zeolite crystals during crystallization. The same effect is observed on RuCNT/ZSM-5, the mesoporous volume also increased twice, from 0.06 $cm^3\ g^{-1}$ to 0.13 $cm^3\ g^{-1}$. We observed [25] a similar impact of Co/CNT used as secondary templates on the porous structure of ZSM-5 zeolite. The catalyst mesoporous volume increased several times after addition of Co/CNT to the zeolite synthesis gel.

Table 3.1. Textural properties.

Sample	N_2 Adsorption				Particle size (nm)	Metal Content (wt.%)	SiO_2/Al_2O_3
	S_{BET} (m^2g^{-1})	V_{total} (cm^3g^{-1})	V_{mic} (cm^3g^{-1})	V_{meso} (cm^3g^{-1})			
BEA	937	0.53	0.27	0.26	-	0	25.0
Co/BEA	638	0.37	0.19	0.18	18	12.7	24.5
CoCNT/BEA	652	0.52	0.17	0.35	-	9.9	34.7
Ru/BEA	707	0.52	0.20	0.31	14	6.5	31.6
RuCNT/BEA	561	0.46	0.17	0.30	44	2.0	72.0
ZSM-5	425	0.19	0.12	0.07	-	-	24.0
Ru/ZSM-5	336	0.17	0.10	0.06	9	6.7	55.3
RuCNT/ZSM-5	440	0.24	0.11	0.13	48	1.4	63.4

The RuCNT/BEA catalyst shows a different behavior. After removal of CNT, a significant decrease in the sample surface area was observed, while the volume of mesopores was maintained. Note that addition of cobalt or ruthenium via impregnation or crystallization of BEA zeolite in the presence of Ru/CNT and Co/CNT results in a major decrease in the

zeolite microporous volume, relative to the conventionally synthesized zeolite. This decrease in the microporous volume can be attributed to the presence of small RuO_2 and Co_3O_4 particles inside the BEA zeolite microchannels. Note that we did not observe a major decrease in microporous volume, when cobalt or ruthenium were added to ZSM-5 zeolite via impregnation or with the secondary template. The results are consistent with our previous report [14]. We investigated distribution of cobalt ions between channel and external surface of BEA and ZSM-5 zeolites. We found that because of larger zeolite pores, metal ions could diffuse inside the micropores of BEA zeolite, while most of metal ions are located on the outer surface of ZSM-5 zeolite, which has a smaller diameter of micropores. The localization of ruthenium oxide nanoparticle in the micropores of BEA zeolite can therefore result in their partial plugging.

The XRD patterns of the prepared catalysts are displayed in Figure 3.2. All samples present characteristic peaks of MFI and BEA zeolites [27]. In the calcined Ru/ZSM-5, Ru/BEA and Co/ZSM-5 catalysts, the diffraction peaks match well with the characteristic peaks of RuO_2 and Co_3O_4 [25]. The introduction of Ru/CNT during the zeolite synthesis, led to narrowing the RuO_2 XRD characteristic peaks in the RuCNT/ZSM-5 and RuCNT/BEA samples. This can be attributed to the sintering effect during calcination, which leads to the formation of larger particles. Introduction of Co/CNT in BEA synthesis also leads to broadening XRD Co_3O_4 peaks. This indicates the formation of smaller Co_3O_4 particles, when Co/CNT was used for the zeolite synthesis, compared with the synthesis without CNT. The particle size of Co_3O_4 and RuO_3 calculated using the Scherrer equation (Table 3.1) was between 9 and 44 nm, indicating that at list a part of metal nanoparticles is located either in the mesopores or on the zeolite external surface.

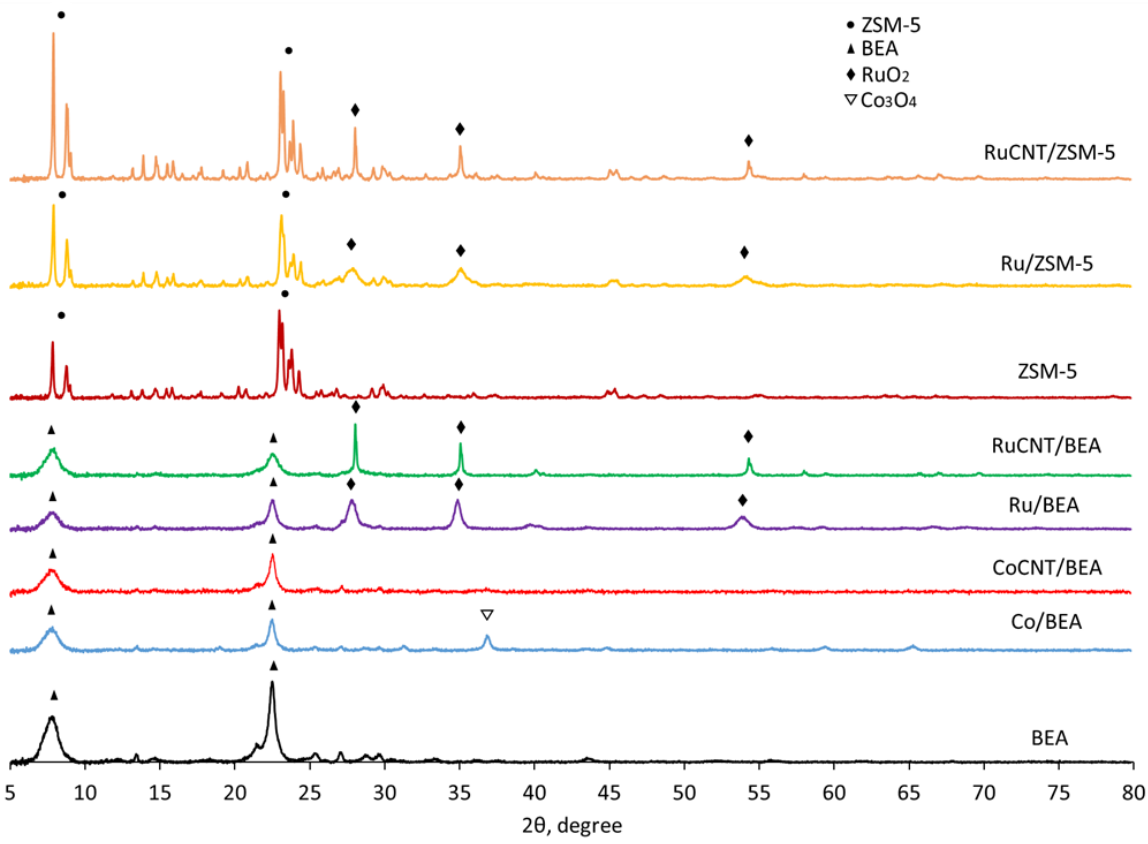

Figure 3.2. XRD patterns of the metal/CNT zeolite catalysts.

The impact of addition of metal-CNT during the zeolite synthesis on the zeolite morphology was investigated by TEM in the Ru/ZSM-5 and RuCNT/ZSM-5 catalysts (Figure 3.3). The zeolite crystallization in the presence of Ru/CNT leads to the formation of large pores in the zeolite crystals (Figure 3.3c). These pores are formed after calcination, when CNT is removed from the zeolite. The presence of regularly shaped pores is not observed in the zeolite crystallized in the presence of Ru/CNT, due to less regular shape of the zeolite crystals in the presence of CNT and consistent with the higher mesopore volumes observed for calcined RuCNT/ZSM-5 in comparison with Ru/ZSM-5 (Table 3.1). In agreement with our previous reports [25], [26], Figure 3.3d shows that the zeolite morphology replicates that of carbon nanotubes, containing ruthenium nanoparticles.

Figure 3.3c and Figure 3.3d show a large number of small RuO_2 particles with a diameter between 5 and 20 nm in RuCNT/ZSM-5. This suggests that the ruthenium particles are situated in the zeolite mesopores and on the outer surface, with only a very small fraction which can be possibly located inside the micropores.

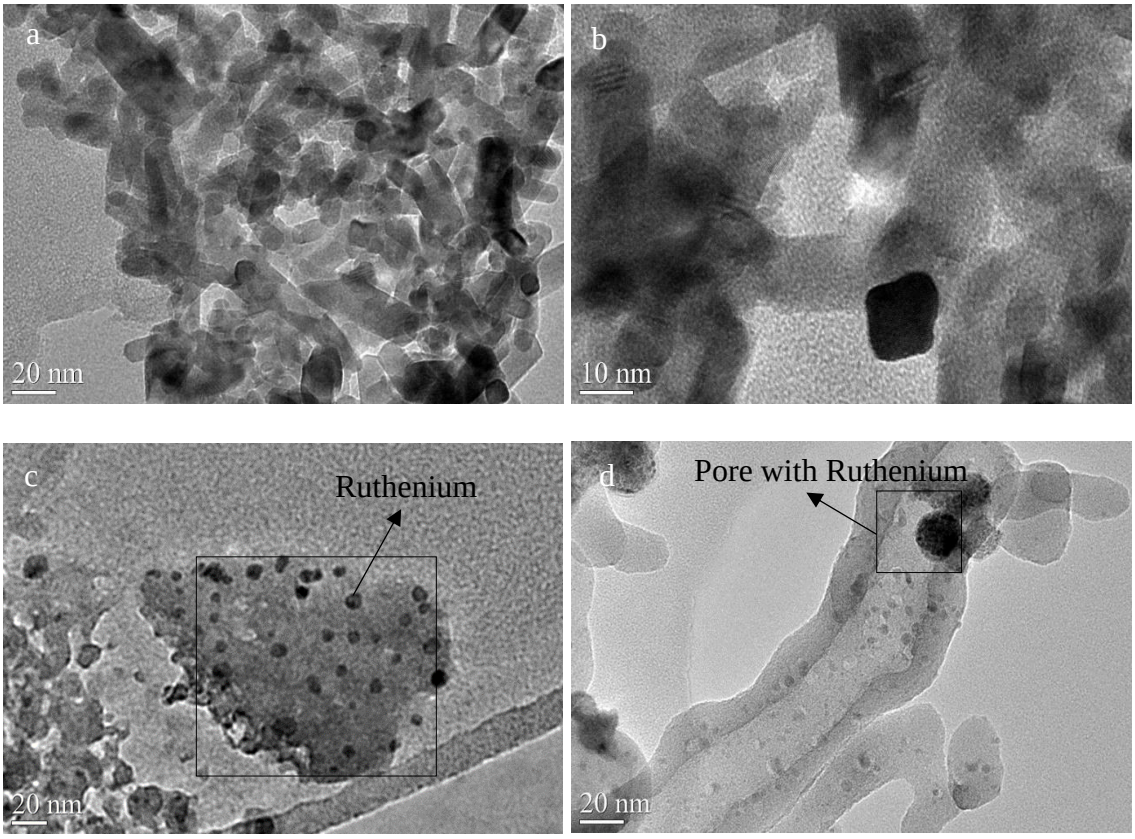

Figure 3.3. TEM images of catalysts Ru/ZSM-5 (a and b) and RuCNT/ZSM-5 (c and d).

The reducibility of ruthenium and cobalt in the catalysts has been studied by H_2 TPR **(**Figure 3.4).

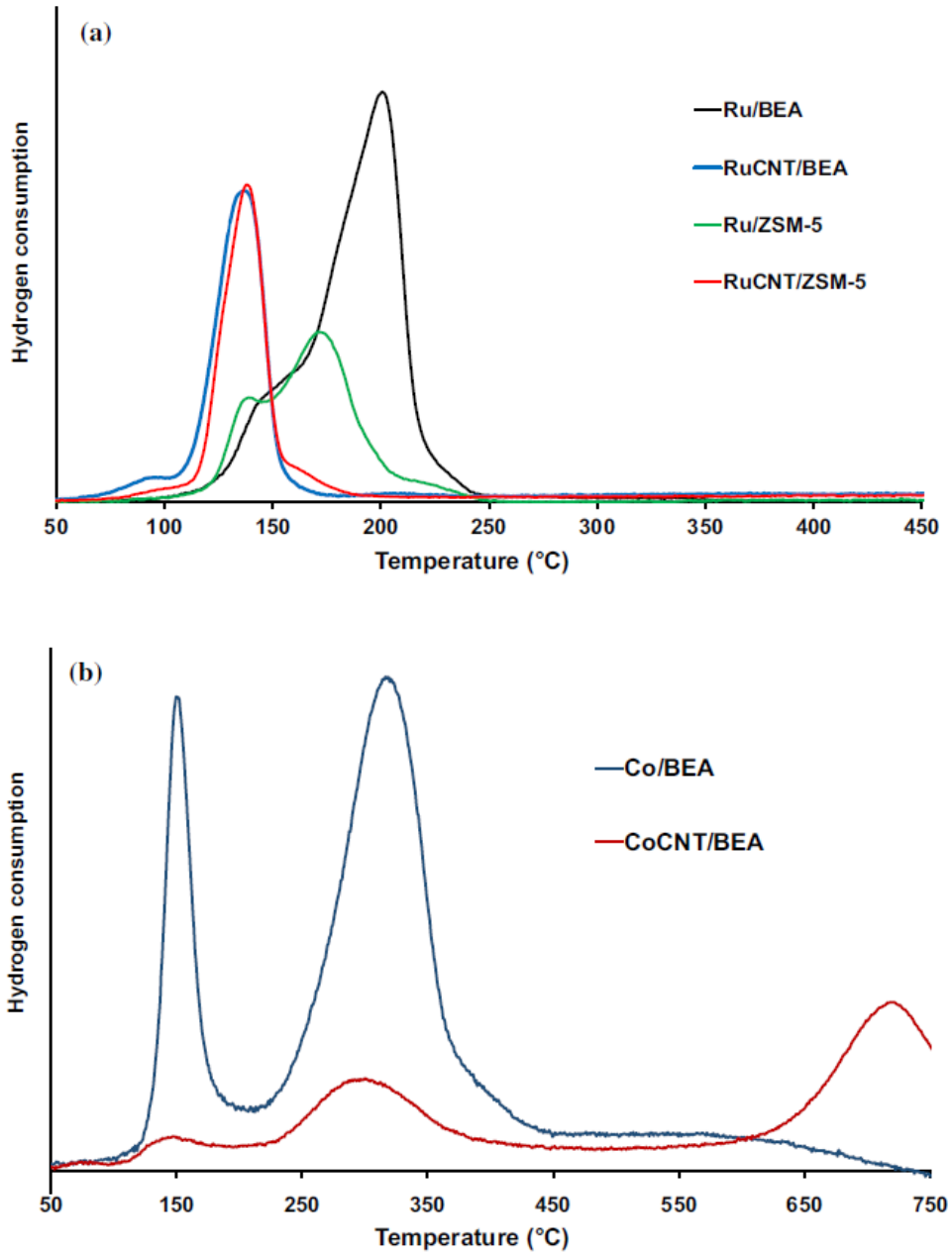

Figure 3.4. Temperature programmed reduction (TPR) profiles of ruthenium (a) and cobalt (b) catalysts.

The TPR profiles of the Ru/BEA and Ru/ZSM-5 catalysts (Figure 3.4a) exhibit two peaks at 150 °C and 200 °C, which were assigned [28], [29] to the consecutive reduction of RuO_2 to RuO and Ru, respectively. No TPR peaks with maximum at temperature higher than

250 °C were observed. A slight shift of TPR peaks to lower temperature is observed in the RuCNT/BEA and RuCNT/ZSM-5 samples. This is indicative of high accessibility of RuO_2 nanoparticles inside of mesopores created by Ru/CNT used as a secondary hard template. Important, the TPR profiles of ruthenium catalyst do not show high temperature peaks, which may be attributed to the mixed ruthenium-support compounds, such as silicates or aluminates. The TPR profiles of the ruthenium catalysts also suggest that all ruthenium oxide species can be reduced to metallic phase after the catalyst exposure to 400 °C and can, therefore, provide active sites for FT synthesis. Important, no barely reducible silicate and aluminate compounds were detected in the ruthenium-zeolite samples.

The catalysts prepared with cobalt exhibit different TPR profiles. In Co/BEA and CoCNT/BEA (Figure 3.4b), these profiles were consistent [30]–[32] with the two-step Co_3O_4 reduction to metallic Co. Co_3O_4 is first reduced to CoO, which is then reduced to metallic Co, thus leading to the formation of two H_2 consumption peaks [30]. In the samples prepared by impregnation, i.e. Co/BEA, the characteristic Co_3O_4 reduction presents a broad peak corresponding to the reduction of Co_3O_4 to CoO and then to metallic cobalt. No peaks at temperatures higher than 450 °C were observed in the TPR profile of Co/BEA, indicating the absence of barely reducible isolated exchanged cobalt ions or cobalt silicates/aluminate. However, in the CoCNT/BEA sample synthesized through the germination of zeolite in the presence of Co impregnated CNT, the second hydrogen consumption peak, observed at 700-730 °C, suggests the presence of a more refractory cobalt phase, such as amorphous cobalt silicates/aluminates [30], [33]. The incorporation of metal in the framework structure of the MFI and BEA zeolite can occur. Several authors have reported incorporation of transition metals into zeolite framework, when this metal was present during hydrothermal synthesis

[34], [35]. After the catalyst exposure to high temperature, these cobalt species form hardly reducible cobalt silicates and cobalt aluminates. A significant part of cobalt cannot be, therefore, reduced at the temperatures typical used for catalyst activation and does not provide active sites for FT synthesis.

3.2.2 Catalytic performance in FT synthesis

The catalytic data of the elaborated materials in a high pressure fixed bed reactor are shown in Table 3.2. The catalytic performance of the catalysts was tested for at least 40 h. The gas space velocities were adjusted to obtain the CO conversions between 20 and 35%. The FT reaction rates calculated as cobalt or ruthenium time yields, vary between 88 and 1380 $mmol_{CO}.h^{-1}g_{cat}^{-1}$. The catalyst activity decreases in the following order: RuCNT/BEA > Ru/BEA > Co/BEA > RuCNT/ZSM-5 > Ru/ZSM-5 > CoCNT/BEA.

Table 3.2. Activity and selectivity of the catalysts for the Fischer-Tropsch synthesis reaction (P = 2 MPa, GHSV = 39-120 $Lh^{-1}g_{cat}^{-1}$, T = 250 °C, $H_2/CO = 2$).

Catalyst	FT reaction rate ($mmol_{CO}\ h^{-1}\ g_{Catt}^{-1}$)	Conversion (%)	Selectivity					
			CH_4 (%)	C_2-C_4 (%)	C_2-C_4 (olefin)	C_2-C_4 (paraffin)	C_2-C_4 (O/P)	C_{5+} (%)
Co/BEA	379	30	55.2	24.1	7.6	16.5	0.45	20.7
CoCNT/BEA	88	28	17.5	15.6	6.0	9.5	0.64	67.1
Ru/BEA	697	28	61.2	24.2	8.7	15.4	0.58	14.5
RuCNT/BEA	1380	35	27.3	20.3	7.3	13.5	0.59	52.7
Ru/ZSM-5	264	22	21.6	34.5	13.7	20.7	0.66	43.9
RuCNT/ZSM-5	341	12	11.6	13.6	5.9	7.4	0.77	74.6

The hydrocarbon selectivities are also shown in Table 3.2. The methane selectivity varies between 11.6 and 61.2%. The samples synthesized by impregnation, i.e. Co/BEA, Ru/BEA and Ru/ZSM-5, display much higher selectivity towards methane formation when compared to CoCNT/BEA, RuCNT/BEA and RuCNT/ZSM-5. The methane selectivity was 3.1, 2.1 and 1.9 times lower when metal/CNT was present as a secondary template during zeolite synthesis. Similarly, the C_2-C_4 hydrocarbon selectivity was also lower in the samples obtained by insertion of metal/CNT in the crystallization.

3.2.3 Structure-performance correlations in ruthenium-hierarchical zeolite nanocomposites

The characterization data are indicative of a major increase in the mesoporous volume of BEA and ZSM-5 zeolite, when CNTs containing cobalt or ruthenium were used as hard templates for the zeolite synthesis. Interestingly, different to ZSM-5, the BEA zeolite microporous volume slightly decreases, when the zeolite synthesis has occurred in the presence of Co/CNT or Ru/CNT or when cobalt and ruthenium have been added to the BEA zeolite via impregnation. This could be indicative of the localization of a significant part of cobalt species inside the BEA micropores. Indeed, the micropores of BEA zeolite are large than those of ZSM-5. Previously, we already observed the phenomenon [14] for the cobalt zeolite catalysts prepared by impregnation.

Metal dispersion and reducibility are important parameters for FT synthesis, once the catalytic performance depends on the density of metallic active sites [15], [36]. The TPR profiles (Figure 3.4b) show that the CoCNT/BEA and, CoCNT/ZSM-5 from previous work [25], prepared by addition of Co/CNT during the zeolite synthesis contain a higher fraction

of cobalt silicate or aluminates, which are barely reducible and not active for the reaction. This explains the fact that no increase in the activity of ZSM-5 and BEA zeolites calculated per total amount of metal was observed (Table 3.2), when cobalt was added during the synthesis of these zeolites with the secondary hard template. At the same time, some increase in the activity calculated per amount of reducible cobalt was observed for CoCNT/ZSM-5 zeolite (from 244 to > 1800 mmol/g_{cat} h) [25]. Note that a high fraction of cobalt used in the synthesis of CoCNT/ZSM-5 catalysts, was lost for FT synthesis and transformed into inactive hardy reducible cobalt silicate.

The higher activity of the RuCNT/BEA and RuCNT/ZSM-5 samples prepared by introduction of RuCNT in BEA and ZSM-5 synthesis compared to the Ru/BEA and Ru/ZSM-5 catalysts prepared by impregnation (Table 3.2) can be linked to the combination of high ruthenium reducibility, uniform ruthenium distribution and zeolite enhanced mesoporous structure. On the one hand, Figure 3.3c and Figure 3.3d clearly show the presence of RuO_2 particles with the size between 5 and 10 nm, some of these nanoparticles are located in the zeolite micropores. In addition, the mesoporosity facilitates diffusion of the reagents and intermediates and removal of the reaction products. On the other hand, no mixed silicate or aluminate compounds, which can be reduced only at very high temperature were not observed in both RuCNT/ZSM-5 and RuCNT/BEA zeolites.

The zeolite pore structure, metal particle sizes, and their localization within the zeolite can explain the selectivity towards short carbon-chain products and methane observed on the metal-zeolite catalysts. The diffusion limitations due the localization of metal oxide nanoparticles in narrow pores of the Co/BEA, Ru/BEA, Ru/ZSM-5 and Co/ZSM-5 zeolites prepared without metal-CNT hard templates can result in higher methane and lower carbon-

chain products selectivities [15], [36]. The metal-zeolite catalysts prepared by impregnation do not show developed mesoporosity and the diffusion of reacting molecules, and intermediates principally occurs within zeolite micropores with diameters between 0.55 and 0.76 nm. Previously, higher methane selectivity over narrow pore catalysts was observed and explained by Iglesia [36], [37]. A much higher diffusivity of hydrogen compared to carbon monoxide, results in the enrichment of zeolite micropores with hydrogen and thus, higher rates of hydrogenation reactions and methane production. The presence of diffusion limitations and consequently higher H_2/CO ratio in zeolite micropores, also result in lower olefins/paraffins (O/P) ratios (Table 3.2) for the samples prepared by impregnation. Higher paraffin yields are linked to the higher rate of olefin secondary hydrogenation, which is favored when diffusion limitations and olefin residence time in the zeolite pores are more significant. In addition, the higher selectivity to the C_2-C_4 hydrocarbons, and consequent lower C_{5+} hydrocarbon yield, observed for the impregnated samples could be due to the cracking of larger olefin molecules. The cracking of the long chain olefins is enhanced by the longer residence time in the zeolite micropores and diffusion limitations [38], [39].

The CoCNT/BEA, RuCNT/BEA and RuCNT/ZSM-5 samples prepared using MeCNT as secondary templates have higher mesoporous volume, compared to the conventionally synthetized zeolites (Table 3.1). The diffusion of higher hydrocarbons is therefore enhanced in the hierarchical catalysts, which reduces their residence time inside the zeolite pores and slows down the cracking. This suggestion is consistent with higher selectivity to longer carbon chain hydrocarbons observed on CoCNT/BEA, RuCNT/BEA and RuCNT/ZSM-5 relative to Co/BEA, Ru/BEA and Ru/ZSM-5 counterparts (Table 3.2).

3.3 Conclusions

The synthesis of BEA and ZSM-5 zeolites in the presence of CNT containing ruthenium generates a complementary mesoporous structure, and results in the nanocomposites built of ruthenium nanoparticles and hierarchical zeolites. In the BEA zeolite prepared by both impregnation and synthesis in the presence of metal-CNT templates, a major fraction of metals species is located inside zeolite micropores. Ruthenium species exhibit much easier reducibility compared to cobalt, when introduced to the BEA and ZSM-5 zeolite with metal-CNT secondary templates. In Co/BEA, a significant amount of barely reducible cobalt silicate inactive in FT synthesis was observed, when cobalt was added with CNT to the BEA zeolite synthesis. The FT reaction rates were twice higher over the catalysts prepared using ruthenium CNT as secondary templates compared to the Ru zeolite catalyst prepared by impregnation or to cobalt counterparts. The synthesis of hierarchical zeolites using ruthenium CNT hard template leads to a uniform distribution of metal nanoparticles within the zeolite mesoporous structure, facilitates the diffusion and strongly enhances the catalytic performance in FT reaction.

[1] C. Gao, F. Lyu, and Y. Yin, "Encapsulated metal nanoparticles for catalysis," *Chem. Rev.*, vol. 121, no. 2, pp. 834–881, 2021.

[2] J. Liang, Z. Liang, R. Zou, and Y. Zhao, "Heterogeneous catalysis in zeolites, mesoporous silica, and metal–organic frameworks," *Adv. Mater.*, vol. 29, no. 30, pp. 1–21, 2017.

[3] C. Martínez and A. Corma, "Inorganic molecular sieves: Preparation, modification

and industrial application in catalytic processes," *Coord. Chem. Rev.*, vol. 255, pp. 1558–1580, 2011.

[4] A. Kostyniuk, D. Bajec, A. Prašnikar, and B. Likozar, "Catalytic hydrocracking, hydrogenation, and isomerization reactions of model biomass tar over (W/Ni)-zeolites," *J. Ind. Eng. Chem.*, vol. 101, pp. 293–306, 2021.

[5] R. Maghrebi, M. Buffi, P. Bondioli, and D. Chiaramonti, "Isomerization of long-chain fatty acids and long-chain hydrocarbons: A review," *Renew. Sustain. Energy Rev.*, vol. 149, no. July, p. 111264, 2021.

[6] G. Li *et al.*, "Role of SAPO-18 Acidity in Direct Syngas Conversion to Light Olefins," *ACS Catal.*, vol. 10, no. 21, pp. 12370–12375, 2020.

[7] W. Zhou *et al.*, "New horizon in C1 chemistry: Breaking the selectivity limitation in transformation of syngas and hydrogenation of CO2 into hydrocarbon chemicals and fuels," *Chemical Society Reviews*, vol. 48, no. 12. pp. 3193–3228, 2019.

[8] M. Wang *et al.*, "Effect of zeolite topology on the hydrocarbon distribution over bifunctional ZnAlO/SAPO catalysts in syngas conversion," *Catal. Today*, vol. 371, no. June 2020, pp. 85–92, 2021.

[9] F. Jiao *et al.*, "Selective conversion of syngas to light olefins," *Science (80-.).*, vol. 351, no. 6277, pp. 1065–1068, 2016.

[10] K. Cheng, B. Gu, X. Liu, J. Kang, Q. Zhang, and Y. Wang, "Direct and Highly Selective Conversion of Synthesis Gas into Lower Olefins: Design of a Bifunctional Catalyst Combining Methanol Synthesis and Carbon–Carbon Coupling," *Angew. Chemie*, vol. 128, no. 15, pp. 4803–4806, 2016.

[11] S. Lyu *et al.*, "Role of Residual CO Molecules in OX-ZEO Relay Catalysis for Syngas

Direct Conversion," *ACS Catal.*, vol. 11, no. 7, pp. 4278–4287, 2021.

[12] J. Přech *et al.*, "Core-shell metal zeolite composite catalysts for in-situ processing of Fischer-Tropsch hydrocarbons to gasoline type fuels," *ACS Catal.*, vol. 10, no. 4, pp. 2544–2555, 2020.

[13] C. Wang, W. Fang, L. Wang, and F. S. Xiao, "Fischer-Tropsch reaction within zeolite crystals for selective formation of gasoline-ranged hydrocarbons," *J. Energy Chem.*, vol. 54, pp. 429–433, 2021.

[14] V. Subramanian *et al.*, "The role of steric effects and acidity in the direct synthesis of iso-paraffins from syngas on cobalt zeolite catalysts," *ChemCatChem*, vol. 8, no. 2, pp. 380–389, 2016.

[15] A. Y. Khodakov, W. Chu, and P. Fongarland, "Advances in the Development of Novel Cobalt Fischer−Tropsch Catalysts for Synthesis of Long-Chain Hydrocarbons and Clean Fuels," *Chem. Rev.*, vol. 107, no. 5, pp. 1692–1744, 2007.

[16] A. Y. Khodakov, "Fischer-Tropsch synthesis: Relations between structure of cobalt catalysts and their catalytic performance," *Catal. Today*, vol. 144, no. 3–4, pp. 251–257, 2009.

[17] M. E. Dry, "The Fischer–Tropsch process: 1950–2000," *Catal. Today*, vol. 71, pp. 227–241, 2002.

[18] Q. Zhang, J. Kang, and Y. Wang, "Development of Novel Catalysts for Fischer-Tropsch Synthesis: Tuning the Product Selectivity," *ChemCatChem*, vol. 2, no. 9, pp. 1030–1058, Sep. 2010.

[19] A. Carvalho *et al.*, "Elucidation of deactivation phenomena in cobalt catalyst for Fischer-Tropsch synthesis using SSITKA," *J. Catal.*, vol. 344, pp. 669–679, 2016.

[20] A. Carvalho, M. Marinova, N. Batalha, N. R. Marcilio, A. Y. Khodakov, and V. V. Ordomsky, “Design of nanocomposites with cobalt encapsulated in the zeolite micropores for selective synthesis of isoparaffins in Fischer-Tropsch reaction,” *Catal. Sci. Technol.*, vol. 7, no. 21, pp. 5019–5027, 2017.

[21] E. Iglesia, S. L. Soled, R. A. Fiato, and G. H. Via, “Bimetallic Synergy in Cobalt-Ruthenium Fischer-Tropsch Synthesis Catalysts,” *J. Catal.*, vol. 143, pp. 345–368, 1993.

[22] X. Fang *et al.*, “Particle-Size-Dependent Methane Selectivity Evolution in Cobalt-Based Fischer–Tropsch Synthesis,” *ACS Catal.*, vol. 10, no. 4, pp. 2799–2816, Feb. 2020.

[23] V. Subramanian *et al.*, “Design of iron catalysts supported on carbon-silica composites with enhanced catalytic performance in high-temperature Fischer-Tropsch synthesis,” *Catal. Sci. Technol.*, vol. 6, no. 13, pp. 4953–4961, 2016.

[24] K. Cheng, V. Subramanian, A. Carvalho, V. V. Ordomsky, Y. Wang, and A. Y. Khodakov, “The role of carbon pre-coating for the synthesis of highly efficient cobalt catalysts for Fischer-Tropsch synthesis,” *J. Catal.*, vol. 337, pp. 260–271, 2016.

[25] C. Flores *et al.*, “Direct Production of Iso-Paraffins from Syngas over Hierarchical Cobalt-ZSM-5 Nanocomposites Synthetized by using Carbon Nanotubes as Sacrificial Templates,” *ChemCatChem*, vol. 10, no. 10, pp. 2291–2299, 2018.

[26] C. Flores *et al.*, “Versatile Roles of Metal Species in Carbon Nanotube Templates for the Synthesis of Metal-Zeolite Nanocomposite Catalysts,” *ACS Appl. Nano Mater.*, vol. 2, no. 7, pp. 4507–4517, 2019.

[27] N. Mintova, S and Barrier, “Verified Syntheses of Zeolitic Materials, Synthesis

Commission of IZA, Third. 2016."

[28] P. Koopman, "Characterization of ruthenium catalysts as studied by temperature programmed reduction," *J. Catal.*, vol. 69, no. 1, pp. 172–179, May 1981.

[29] P. Betancourt, A. Rives, R. Hubaut, C. . Scott, and J. Goldwasser, "A study of the ruthenium–alumina system," *Appl. Catal. A Gen.*, vol. 170, no. 2, pp. 307–314, Jun. 1998.

[30] E. van Steen *et al.*, "TPR Study on the Preparation of Impregnated Co/SiO2Catalysts," *J. Catal.*, vol. 162, no. 2, pp. 220–229, 1996.

[31] A. Y. Khodakov *et al.*, "Reducibility of cobalt species in silica-supported Fischer-Tropsch catalysts," *J. Catal.*, vol. 168, no. 1, pp. 16–25, 1997.

[32] A. Y. Khodakov, A. Griboval-Constant, R. Bechara, and F. Villain, "Pore-size control of cobalt dispersion and reducibility in mesoporous silicas," *J. Phys. Chem. B*, vol. 105, no. 40, pp. 9805–9811, 2001.

[33] S. J. Jong and S. Cheng, "Reduction behavior and catalytic properties of cobalt containing ZSM-5 zeolites," *Appl. Catal. A Gen.*, vol. 126, no. 1, pp. 51–66, 1995.

[34] Y. Yao, F. Cao, J. Gu, Y. Wu, Y. Zhou, and J. Wang, "Direct hydrothermal synthesis and characterization of framework-substituted Co(Mn)-Beta zeolites," *J. Porous Mater.*, vol. 20, no. 4, pp. 891–896, 2013.

[35] S. N. Azizi and S. Ehsani Tilami, "Framework-incorporated Mn and Co analcime zeolites: Synthesis and characterization," *J. Solid State Chem.*, vol. 198, pp. 138–142, 2013.

[36] E. Iglesia, "Design, synthesis, and use of cobalt-based Fischer-Tropsch synthesis catalysts," *Appl. Catal.*, vol. 161, no. 1–2, pp. 59–78, 1997.

[37] E. Iglesia, S. C. Reyes, R. J. Madon, and S. L. Soled, “Selectivity Control and Catalyst Design in the Fischer-Tropsch Synthesis: Sites, Pellets, and Reactors,” *Adv. Catal.*, vol. 39, no. C, pp. 221–302, 1993.

[38] A. Corma, P. J. Miguel, and A. V. Orchillés, “Can Macroscopic Parameters, Such as Conversion and Selectivity, Distinguish between Different Cracking Mechanisms on Acid Catalysts?,” *J. Catal.*, vol. 172, no. 2, pp. 355–369, Dec. 1997.

[39] S. Van Donk, A. H. Janssen, J. H. Bitter, and K. P. De Jong, “Generation, Characterization, and Impact of Mesopores in Zeolite Catalysts,” *Catal. Rev.*, vol. 45, no. 2, pp. 297–319, 2003.

Chapter 4. Core-shell metal zeolite composite catalysts for *in-situ* processing of Fischer-Tropsch hydrocarbons to gasoline type fuels

Abstract

Fischer−Tropsch synthesis has two main challenges related to direct production of gasoline fuels. First, the chain length distribution of the products follows a broad and unselective Anderson−Schulz−Flory distribution. Second, mostly linear hydrocarbons are formed in the Fischer−Tropsch reaction, thus requiring isomerization while manufacturing gasoline fuels. The present paper addresses a synthetic strategy for the preparation of hierarchical metal and zeolite nanocomposite catalysts for direct synthesis of iso-paraffins from syngas. The nanocomposites are synthesized in three steps. In the first step, the parent (core) zeolite is etched with an ammonium fluoride solution. The etching creates small mesopores inside the zeolite crystals. In the second step, the Ru nanoparticles prepared using water-in-oil microemulsion are deposited in the mesopores of the zeolite. In the third step, a zeolite shell of MFI-type zeolites (silicalite-1 or ZSM-5) is grown on the parent zeolite crystals coating both the etched surface and metallic nanoparticles. Thus, the metal nanoparticles become entirely encapsulated inside the zeolite matrix. Most important parameters such as ruthenium content, zeolite mesoporosity, and more particularly, the acidity of the catalyst shell, which affect the catalytic performance of the synthesized nanocomposite materials in low-temperature Fischer−Tropsch synthesis were identified in this work. The higher relative amount of iso-paraffins was observed on the catalysts containing a shell of ZSM-5. The

proximity between metal and acid sites in the zeolite shell of the nanocomposite catalysts is a crucial parameter for the design of efficient metal zeolite bifunctional catalysts for selective synthesis of gasoline-type fuels via Fischer−Tropsch synthesis, while the acidity of the catalyst core has only a limited impact on the catalytic performance.

4.1Introduction

The second-generation biofuels (gasoline, diesel, etc.) use all types of nonedible biomass, such as lignocellulosic biomass, organic residues, wastes, and so on. The biomass-to-liquid (BTL) thermochemical technology is based on the destruction of biomass by gasification and formation of syngas. Syngas might be further converted into paraffins, olefins, and alcohols by Fischer−Tropsch (FT) synthesis. In the FT synthesis, the catalyst active phase is usually made of VIII group transition metals; the choice of the active phase depends on various factors such as the target product (fuels or chemicals), operating conditions, and cost [1, 2].

The traditional FT technologies have two main challenges related to the direct production of gasoline. First, the chain length distribution of the products follows the statistical Anderson-Schulz−Flory distribution (ASF), which implies the same chain growth probability (α) for all hydrocarbons. Therefore, a specific range of the hydrocarbons cannot be produced with a significant yield. The yield of the C_5−C_9 hydrocarbons (gasoline fraction) is limited to less than 50% by the ASF polymerization statistics. Second, mostly linear hydrocarbons are formed, and thus, an isomerization of the crude FT hydrocarbons is required for production of highoctane gasoline fuels [3].

Because the temperature for low temperature FT synthesis and isomerization are rather similar, syngas can be also converted to iso-pararafins in a single process over bifunctional catalysts. The selectivity to the branched hydrocarbons in direct syngas conversion can be improved by adding an acid function to the FT catalysts [4, 5]. The acidic function is usually provided by a zeolite, such as ZSM-5, beta, and mordenite. In the bifunctional catalysts, the concentrations, intrinsic activities of the metal and acid sites, and in particular, their localization within the catalyst, are extremely important for the catalytic performance [6]. The close proximity, "site intimacy", between the metal and acid sites is required to attain maximum activity and selectivity in many reactions of bifunctional catalysis.

Several configurations of metallic and acid functions in the bifunctional catalysts and combining FT-isomerization process have been described in the literature [7-11]. Dual-bed reactors with an acidic zeolite downstream from a conventional FT catalyst and hybrid catalysts containing a physical mixture of the two components have mainly been utilized for the production of gasoline-range (C_5−C_{12}) hydrocarbons. However, the isomerization efficiency of these catalytic systems has been insufficient. Indeed, the transformation of the formed wax by hydrocracking over metal-free zeolites requires higher temperatures. The yield of gasoline products remains low ($C_{iso}/C_n < 0.2$) because of poor contact between the formed wax and acid sites in the zeolites. Addition of a metal to the zeolite, usually via impregnation or ion-exchange, is often the first step in the preparation of the composite catalyst [12]. However, metal ions partially participate in the ion exchange with the acid sites and thus neutralize the acidic function. In addition, significant diffusion limitations because of extremely small pore sizes of zeolites (typically 0.5−0.7 nm) lead to slow diffusion of

hydrocarbons inside the micropores of the zeolite. The use of mesoporous (hierarchical) zeolites for synthesis of bifunctional catalysts is a common approach to overcome the diffusional limitations and to increase carbon monoxide conversion [13].

Localization of metal nanoparticles inside the zeolite micropores also introduces shape-selectivity effects for the formed hydrocarbons [14, 15]. Recently, we found that FT reaction selectivity to short chain iso-paraffins was principally affected by the zeolite acidity, while the selectivity to slowly diffusing long-chain hydrocarbons mostly depended on the proximity between the metal and acid sites [16]. The use of cobalt zeolite nanocomposites with cobalt nanoparticles selectively located inside the zeolite pores led to significantly higher selectivity to the C_5–C_{12} branched hydrocarbons in FT synthesis [17]. However, the stability of the composite catalysts prepared by impregnation is a critical issue. In the presence of a reaction mixture and in particular water, metal nanoparticles can migrate out the zeolite pores and agglomerate on the zeolite outer surface. This results in formation of large metal nanoparticles on the zeolite surface and decrease in both reaction rate and selectivity to iso-paraffins. In addition, diffusion limitations result in higher selectivity to methane, which is a low cost product, and thus decreases the yield of the desired longer hydrocarbons [18]. To increase efficiency of the secondary (isomerization) reactions in the bifunctional process, Tsubaki and co-workers and Zhu and Bollas designed capsule core–shell catalytic systems, which contain conventional FT catalyst such as Co/SiO_2 or Co/Al_2O_3 in the core and an acidic zeolite membrane shell on the surface of the catalyst grains [19-21].

Another approach involves using Co/SiO_2 as precursor of Co-zeolite catalysts [22-24]. In principle, the SiO_2 carrier acts as a silica source for the zeolite (ZSM-5)

crystallization, while the Co_3O_4 nanoparticles become encapsulated in the formed zeolite. The developed bifunctional catalysts exhibit high selectivity to a gasoline range of hydrocarbons with a higher yield of isomers in comparison with hybrid and composite catalysts prepared by impregnation. Nevertheless, a thin layer of the zeolite on the surface of a metallic catalyst cannot provide high efficiency in isomerization of the produced hydrocarbons. An increase in the zeolite layer thickness increases diffusion limitations and thus methane production. Metal species can also be added directly into a conventional zeolite synthesis gel, but they often result in uncontrollable metal distribution within the zeolite crystals [25]. Recently, we proposed introduction of metal species to the zeolites during their synthesis using metal containing carbon nanotubes as secondary hard templates [26, 27]. The metal carbon nanotube templates play several roles [27]. First, they serve as a replica to create zeolites with specific fibrous morphology. Second, they markedly increase the zeolite secondary porosity. Finally, metal carbon nanotube templates introduce the metal nanoparticles uniformly inside the mesoporous zeolites, however, without their complete encapsulation.

In this manuscript, we propose a new strategy for the synthesis of efficient metal zeolite bifunctional catalysts for the direct synthesis of branched gasoline type hydrocarbons from syngas. This strategy addresses nanocasting of preformed ruthenium metallic nanoparticles in a secondary pore system of a mesoporous zeolite. The metal nanoparticles located in the mesopores of the zeolite are then entirely encapsulated by secondary grown zeolite structure. This new approach offers a number of advantages. First, the separate preparation of metal nanoparticles allows a fine control of their sizes, morphology, and chemical composition. In contrast to the in situ synthesis of metal nanoparticles inside of the

zeolites pores, the impact of the zeolite matrix on the size and shape of the nanoparticles is suppressed. Futhermore, the nanoparticles are stabilized in the encapsulated systems, thus suppressing the particle migration and sintering. Finally, the proximity between metal and zeolite active sites provides an unravelled synergy between the two types of the sites in the catalyst. The zeolite performance in hydrocarbon isomerization is mostly affected by the composition of the zeolite shell. The prepared catalysts were characterized using a wide range of techniques, which provide information on their morphology, structure, texture, and chemical composition. Their catalytic performance in the FT reaction was evaluated under high pressure in a fixed bed microreactor using a high-throughput catalytic setup.

4.2 Results and Discussion

4.2.1 Strategy for the Synthesis of Zeolite Catalysts with Encapsulated Metal Nanoparticles

The synthesis of the metal-zeolite composite catalysis with encapsulated metal nanoparticles is composed of 3 major steps (Scheme 4.1). In the first step (etching), the parent (core) zeolite is treated with a 40% NH_4F solution [28]. The etching creates small mesopores inside the zeolite crystals and sort of cups on the surface of the crystals, which accommodate metallic nanoparticles in the second step (insertion) and serves as nucleation sites in the third step (coating). The Ru nanoparticles were prepared using water-in-oil microemulsion following the procedure and then deposited in the mesopores of the zeolite [29]. Ruthenium nanoparticles are introduced in the second step (insertion) into the etched zeolite. In the third step (coating), the zeolite shell crystallizes on the surface of parent crystals covering both

etched surface and metallic nanoparticles, which become trapped inside the zeolite matrix. The resulting composite samples are denoted as shell/metal/core (e.g., ZSM-5/Ru/S-1 means the sample has a core (parent) crystal of S-1, ruthenium nanoparticles and it was coated by a ZSM-5 shell).

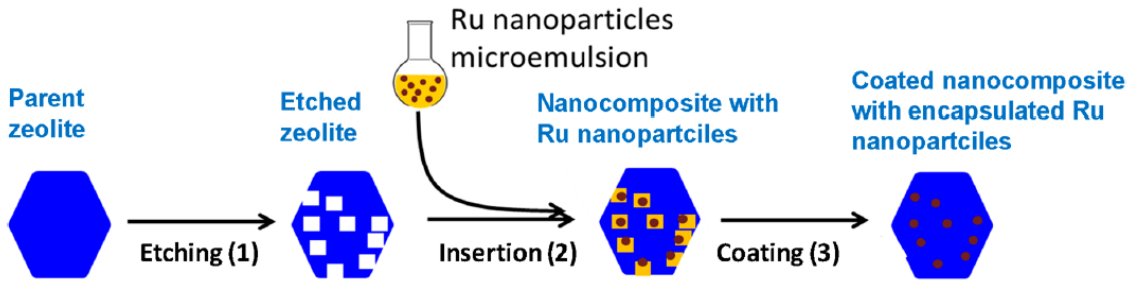

Scheme 4.1. Synthesis of the zeolite catalysts with encapsulated ruthenium nanoparticles.

In the present study, the Ru-zeolite composites with various combination of core and shell materials (either acidic ZSM-5 or inert S-1) were prepared. In addition, the noncoated composites Ru/ZSM-5, Ru/S-1, Ru/nonetched-ZSM-5, and Ru/nonetched-S-1 have been also tested.

4.2.2 Catalyst Structure

The prepared catalysts were characterized by a combination of techniques. Figure 4.1 presents the SEM images of the ZSM-5/Ru/ZSM-5 and ZSM-5/Ru/S-1 catalysts at different stages of the synthesis. The parent ZSM-5 zeolite (Figure 4.1A) has regular coffinshaped crystals sometimes forming twins with a size of approximately 3−4 μm in the longest dimension. Parent S-1 (Figure 4.1F) is composed of irregular crystals having 3−5 μm in diameter. Upon the fluoride etching, the crystal twins are separated, leaving regular holes in

the crystals and creating crystals were in contact (Figure 4.1B, G). These rough surfaces are ideal places to accommodate the Ru nanoparticles. They can also act as seeds for the crystallization of the new (coating) zeolite phase in the catalyst shell. After the insertion, some of the nanoparticles agglomerate, while the rest is dispersed on the surface and accommodated in the etched mesopores (cf. TEM image Ru/ZSM-5) images collected using BSE (backscattering electron) detector highlights the presence of dense metallic phase (Figure 4.1D, I).

Upon subsequent crystallization (coating), a thin layer of small ZSM-5 crystals is formed and encapsulates the Ru nanoparticles inside the zeolitic phase (Figure 4.1E, J). Note that the original shape of the parent crystals can be clearly identified by SEM and TEM through all characteristic rough surfaces on the planes, where the two the stages. The S-1 shell crystallizes in slightly different morphology. The formed phase appears better connected to the parent crystals (Figure 4.2) and it has more uniform surface.

Moreover, formation of some larger (200−500 nm) secondary S-1 crystals occurred, however their amount was relatively low. The catalyst synthesis was followed by powder XRD. Figure 4.3 shows representative XRD patterns for ZSM-5/Ru/ZSM-5 in the final stages of the synthesis. The patterns for the other catalysts did not differ significantly. After the Ru insertion (data not presented) and coating (Figure 4.3, ZSM-5/Ru/ZSM-5 as-synthesized), the XRD patterns of the as-synthesized catalyst contained only the patterns of MFI zeolite.

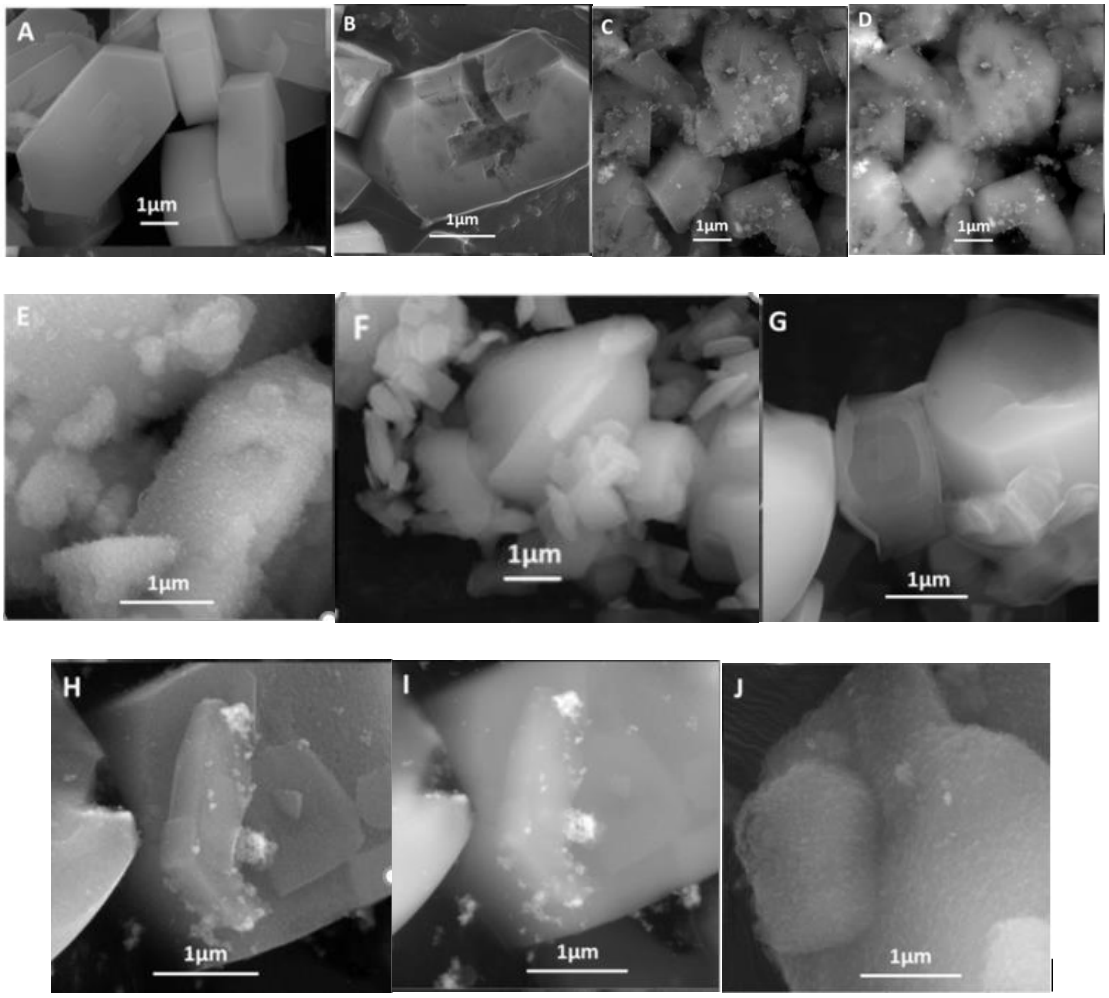

Figure 4.1. SEM images of the ZSM-5/Ru/ZSM-5 (A−E) and ZSM-5/ Ru/S-1 (F−J) in the course of the synthesis: parent ZSM-5 (A), S-1 (F); fluoride etched ZSM-5 (C) and S-1 (G); Ru/ZSM-5 and Ru/S-1 after insertion of Ru nanoparticles and calcination in the view of secondary electron (conventional) detector (C, H) and BSE detector (D, I); final overgrown ZSM-5/Ru/ZSM-5 (E) and ZSM-5/Ru/S-1 (J).

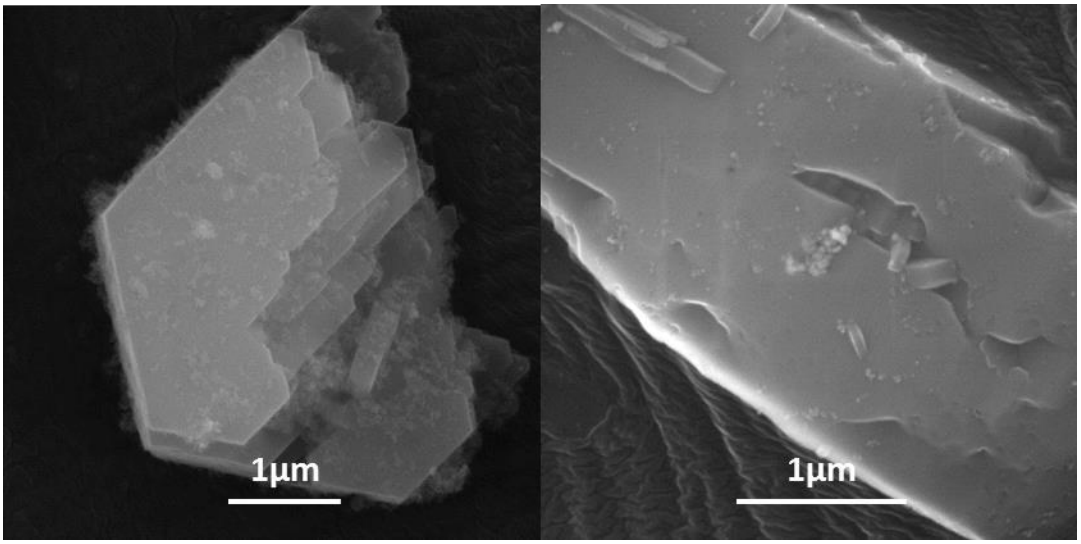

Figure 4.2. SEM images of ZSM-5/Ru/S-1 (S-126, left) and S-1/Ru/S-1 (S-137, right).

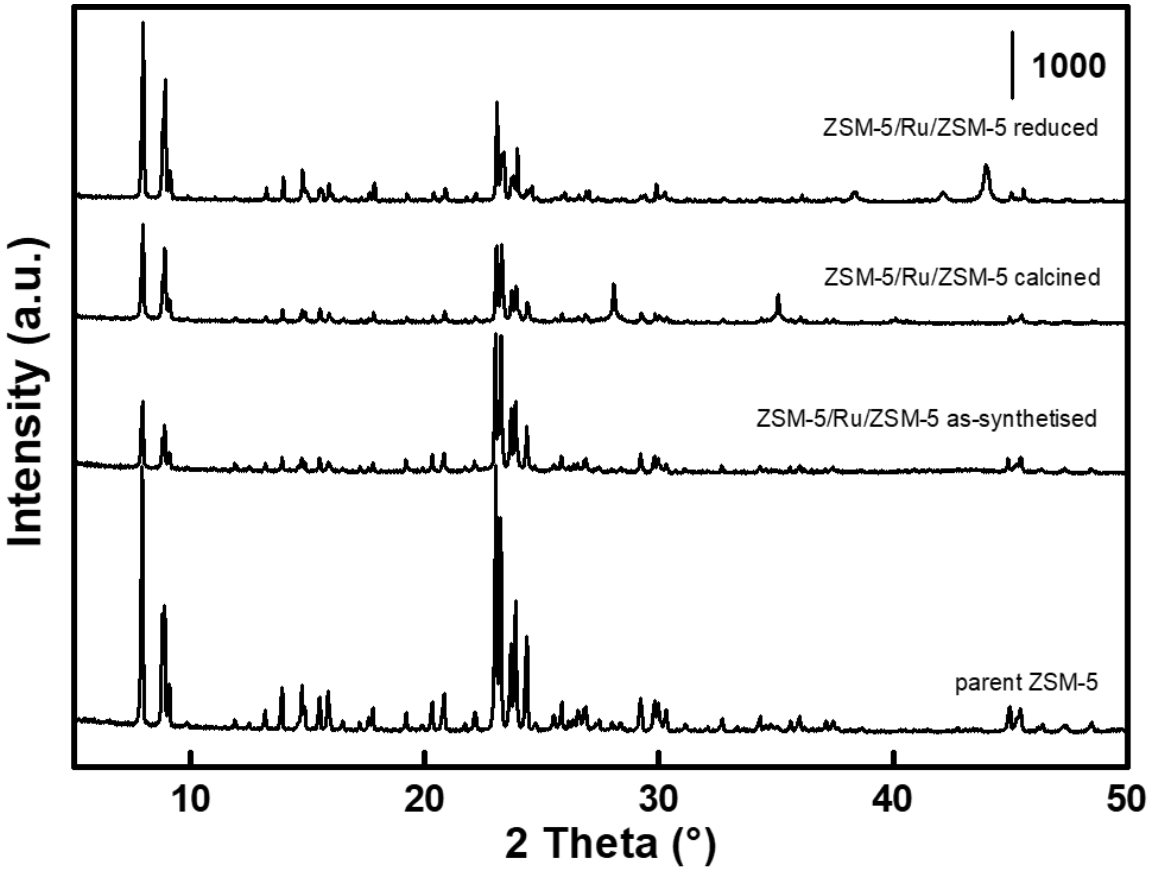

Figure 4.3. Powder XRD patterns for the ZSM-5/Ru/ZSM-5 at different stages of the synthesis.

No XRD peaks attributed to the ruthenium phases were observed. This is an indirect proof that the Ru nanoparticles are too small to be detected by XRD. The size of Co nanoparticles prepared according to the method described by Subramanian *et al*. [29] was approximately 5 nm. We expect, therefore, the Ru nanoparticles formed in microemulsion to be of a similar size. After calcination, broad reflections of the RuO_2 phase appear in the XRD pattern at ($2\theta = 28.05°$ and $35.1°$) because the metallic ruthenium quickly oxidize to the oxide, when exposed to oxygen at elevated temperature (during calcination). The appearance of the lines points to the increase in the particle size due to some sintering during the calcination and oxidation of the metal. The RuO_2 particle size in the final catalysts is about 20 nm (see below). Nevertheless, the RuO_2 can be easily reduced back to Ru in hydrogen atmosphere, exhibiting broad XRD lines at $2\theta = 38.5°$, $42.3°$, and $44.2°$. The reduction of the catalysts was performed in situ after charging into the reactor. SEM (Figure 4.1) and TEM images (Figure 4.4) suggest that the Ru diffraction lines are mostly relevant to the Ru agglomerates, which can sinter to form larger Ru crystals. XRD patterns of all the discussed catalysts are also presented in Figures S1 and S2, Supporting Information (SI). Note that all the XRD patterns exhibit a straight baseline, which (together with the textural properties analysis, vide infra) proves the crystallinity of the coating shell. For comparison, the XRD pattern of a catalyst with amorphous silica shell is shown in Figure S3, SI. In this image, a baseline elevation between $2\Theta = 15°–30°$ can be observed, which is characteristic of amorphous silica.

Figure 4.4 presents TEM images of the catalysts with a shell on the surface of the parent (core) crystals and a fragment of parent crystal having no shell (Ru/ZSM-5). The TEM image of the Ru/ZSM-5 catalyst (Figure 4.4c) shows the presence of small mesopores formed

by the fluoride etching. Previously, we showed that the mesopores created by fluoride etching might have rectangular shape [28]. The histogram of particle size distribution has shown that in Ru/ZSM-5 mostly contains the particles smaller than 25 nm (Figure S4, SI). It also reveals Ru nanoparticles in these small mesopores where, in some cases, they adopt their size and shape. In the images of the coated catalysts, particularly those with the ZSM-5 shell (Figure 4.4a, d), the nanoparticles are covered with the small ZSM-5 crystals formed during the coating. The inset in Figure 4.4d illustrates typical Ru nanoparticles (darker round spots in middle bottom of the image) size of about 10−20 nm, but even smaller nanoparticles can be found (e.g., in Figure 4.4a).

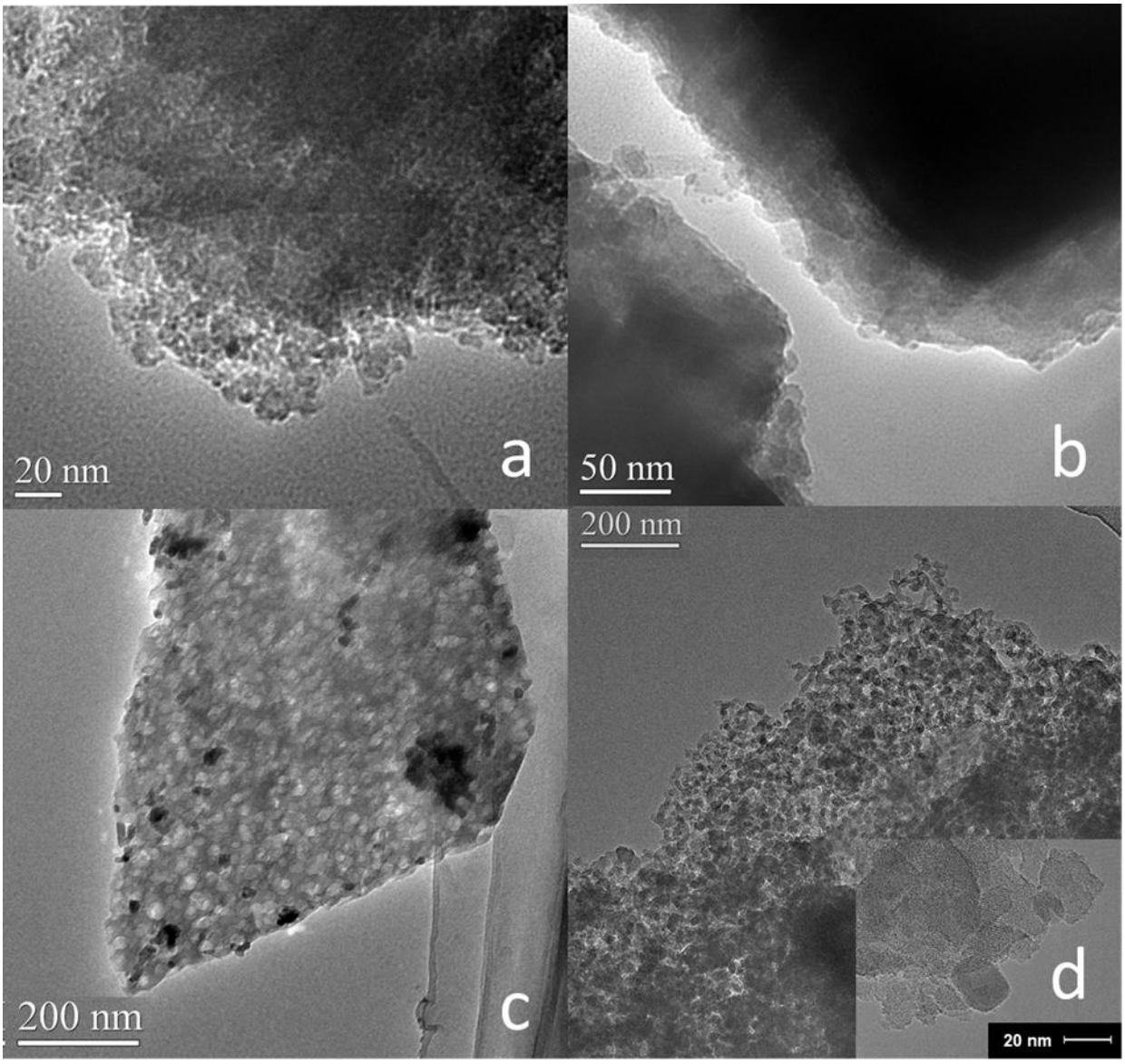

Figure 4.4. TEM images of the composite catalysts: (a) ZSM-5/Ru/ZSM-5, (b) ZSM-5/Ru/S-1, (c) Ru/ZSM-5, (d) S-1/Ru/ZSM-5.

Thus, we conclude the size of Ru nanoparticles inside the zeolite crystals ranges between about 3 and 20 nm. The TEM image of S-1/Ru/ZSM-5 (Figure 4.4b) confirms that the S-1 shell is more uniform in comparison with the ZSM-5 overgrown catalysts, and as a result, the nanoparticles are more difficult to be observed.

The characterization data are summarized in Table 4.1. In general, all the catalysts exhibit similar textural properties, since their structure is essentially the same. S-1/Ru/ZSM-5 and S-1/Ru/S-1 (the two with S-1 shell) have slightly lower BET surface area and micropore volume in comparison with their ZSM-5 shell analogues (e.g., BET = 320 m^2/g vs 400 m^2/g and 346 m^2/g vs 404 m^2/g, respectively). This probably points to a lower crystallinity of the S-1 shell in comparison with ZSM-5. The Ru content varies between 6 and 8.4 wt.% for all the catalysts, except for the pair Ru/S-1 and Ru/ZSM-5 (11.2 wt.% and 10.9 wt.%, respectively), because these two catalysts contain the mesopores to accommodate the Ru nanoparticles, but their Ru content is not decreased by the subsequent coating. The Si/Al ratio (and the Al content of the catalyst) depends on the synthesis procedure. The parent ZSM-5, as well as the etched ZSM-5, has Si/Al = 21. The ZSM-5/Ru/ZSM-5 catalyst was prepared by coating with a sol having Si/Al ratio of 30 thus causing the decrease in the Si/Al ratio to Si/Al = 27. Similarly, coating with pure silica sol (giving S-1 shell) resulted in further increase to Si/Al = 51. Coating of the initially pure silicalite-1 Ru/S-1 with Al containing sol (Si/Al = 30) provided a catalyst with overall Si/Al = 168. Note that these values represent an average over all the catalysts; the Si/Al ratio in the core part is preserved (that means Si/Al = 21 and Si/Al = ∞ for ZSM-5 and S-1 core, respectively).

Table 4.1. Composition, Textural Properties, and Concentration of Acid Sites in Metal Zeolite Composite Catalysts.

Catalyst **Shell/Me/Core**	**Ru[a],** **wt.%**	**Si/Al[b]**	**BET[c]** **m^2/g**	**V_{mic}[c],** **cm^3/g**	**V_{tot}[c],** **cm^3/g**	**S_{ext},** **m^2/g**	**Brønsted sites[d],** **mmol/g**	**Lewis sites[d],** **mmol/g**
Ru/non etched S-1	5.9	∞	361	0.127	0.20	23	0	0
Ru/etched S-1	11.2	∞	371	0.131	0.20	21	0	0
S-1/Ru/S-1	5.2	∞	346	0.116	0.21	68	0	0
Ru/non-etched ZSM-5	8.4	21	375	0.130	0.19	22	0.487	0.042
Ru/ZSM-5	10.9	21	365	0.121	0.22	46	0.32	0.036
S-1/Ru/ZSM-5	5.9	51	320	0.104	0.23	49	0.168	0.03
ZSM-5/Ru/S-1	6.7	168	404	0.133	0.24	41	0.049	0.018
ZSM-5/Ru/ZSM-5	7.8	27	400	0.138	0.25	59	0.465	0.057

[a]Ru content was determined from integral H_2 consumption in a TPR experiment: [b] Si/Al ratio determined by ICP-OES;[c] Textural properties were determined from nitrogen sorption isotherms collected at -196°C; [d] concentration of acid sites was determined from pyridine adsorption/desorption at 150°C with FT-IR quantification of pyridinium species.

The acid sites are of the Brønsted character (approximately 90%), except for ZSM-5/Ru/S-1, where the share of Lewis acid sites reaches 27%. Figure S5, SI shows IR spectra used for calculation of the acid site concentration. In the spectra of silanol region after activation, the band at 3610 cm^{-1} evidences the presence of bridging Al-(OH)-Si groups (Brønsted acid sites). Only in the case of ZSM-5/Ru/S-1, its intensity is not sufficiently high

to be visible. Nevertheless, the bands at 1545 and 1455 cm^{-1}, observed after pyridine adsorption/desorption at 150 °C, shows the presence of both Brønsted and Lewis acid sites, respectively, like in all other Al-containing catalysts.

Figures 4.5 and 4.6 present the nitrogen sorption isotherms, which served for the calculation of textural properties displayed in Table 4.1. The isotherm of Ru/nonetched ZSM-5 is very similar to the one of parent ZSM-5 before etching (not presented). The slight increase in the N_2 uptake at high p/p_0 results from interparticle adsorption in the agglomerates of Ru nanoparticles. Ru/ZSM-5 takes more N_2 into the etched mesopores at high p/p_0 (cf. TEM images). The coated ZSM-5/Ru/ZSM-5 and S-1/Ru/ZSM-5 show a hysteresis because of intercrystalline adsorption in the shell, which is composed of small ZSM-5 crystals. The high uptake above $p/p_0 = 0.9$ exhibited by S-1/Ru/ZSM-5 confirms that the shell is not 100% crystalline but there is no baseline elevation around $2\theta = 20°–25°$ in the XRD pattern of this catalyst, which was observed for catalysts with completely amorphous shell (Figure S3, SI).

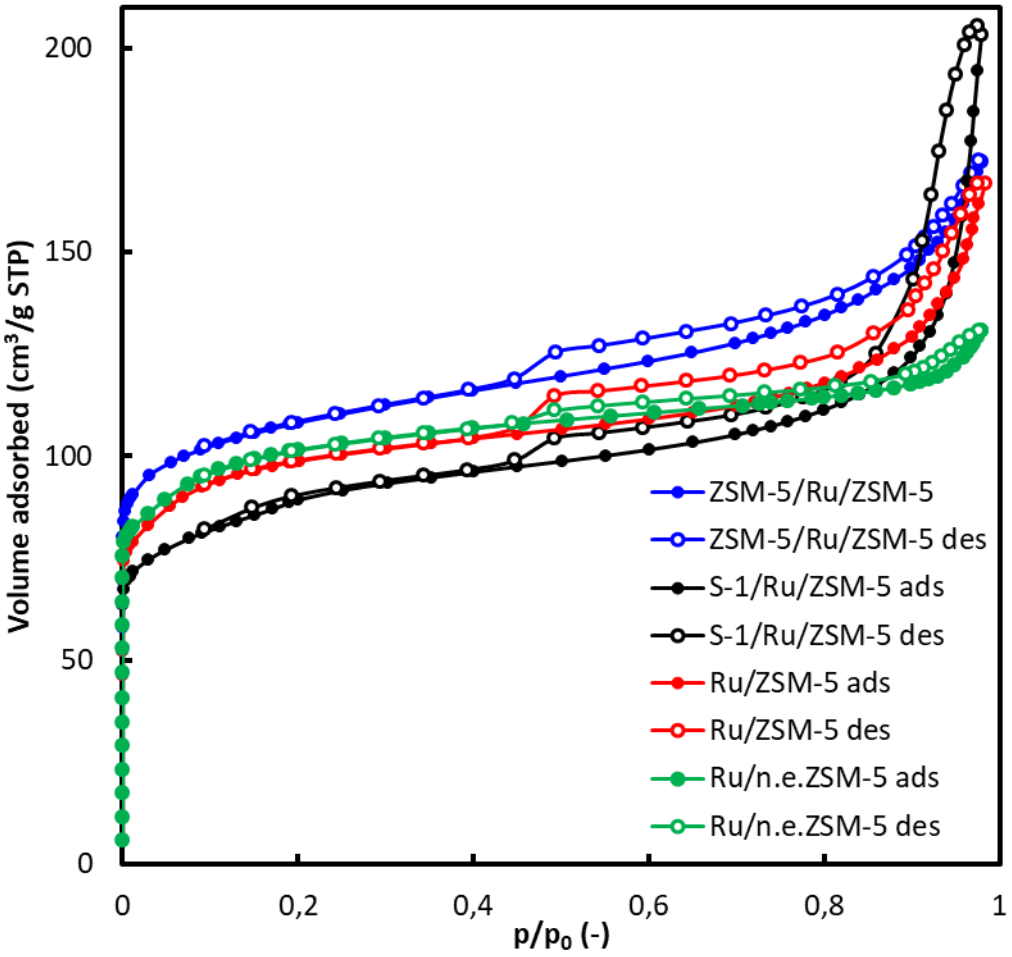

Figure 4.5. N_2 sorption isotherms of the catalysts with ZSM-5 core: ZSM-5/Ru/ZSM-5 (blue), S-1/Ru/ZSM-5 (black), Ru/ZSM-5 (red), Ru/n.e.ZSM-5 (green); empty points denote desorption.

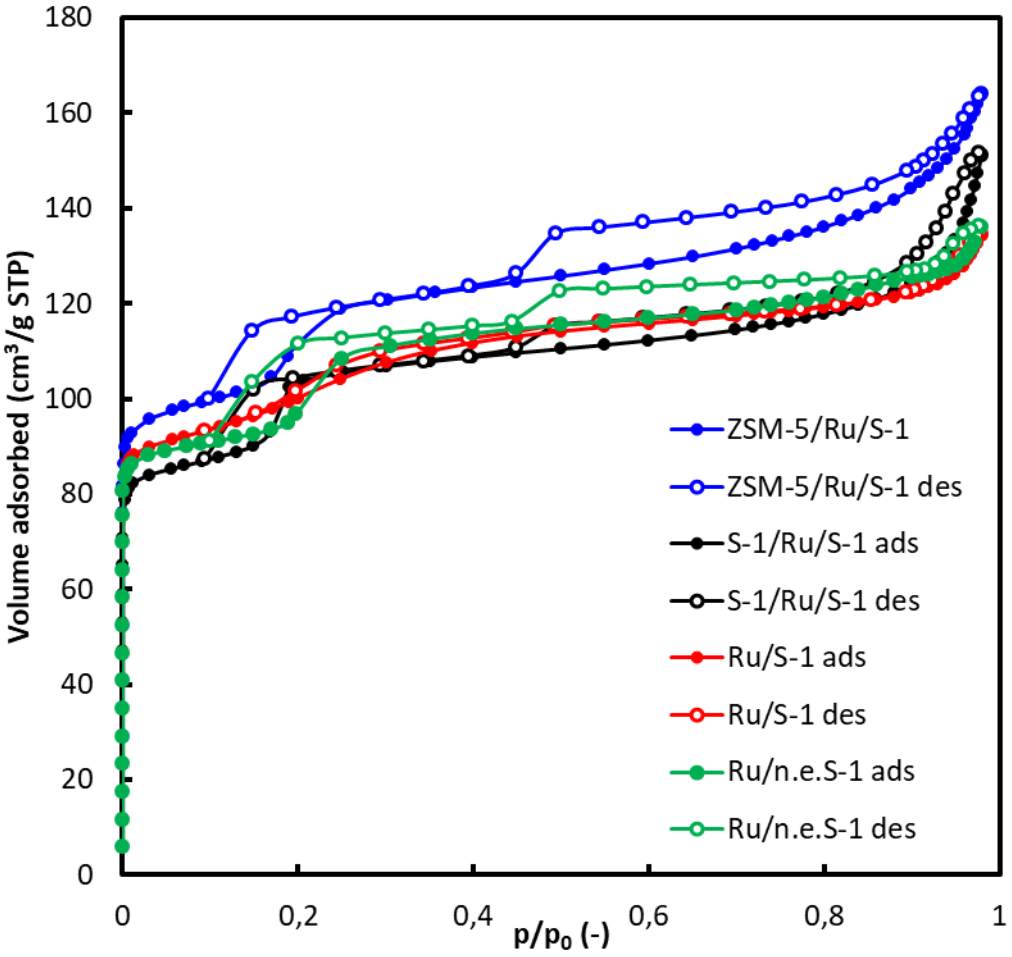

Figure 4.6. N_2 sorption isotherms of the catalysts with S-1 core: ZSM-5/Ru/S-1 (blue), S-1/Ru/S-1 (black), Ru/S-1 (red), Ru/n.e.S-1 (green); empty points denote desorption.

The catalysts prepared from S-1 parent exhibit an additional hysteresis at p/p_0 = 0.1−0.3 (Figure 4.6). The difference of the isotherm of S-1 based catalysts with the parent nonetched S-1 and etched S-1 (Figure S6, SI) is most probably due to the presence of Ru nanoparticles. This additional hysteresis (with another one at $p/p_0 = 10^{-4} - 10^{-2}$) has been observed before for high silica MFI zeolites, and it is not related to adsorption in mesopores (which occurs above relative pressure of 0.35) [32, 33]. The origin of these hystereses is still

under debate. So far, a possible explanation can be related to the occurrence of a phase transition between monoclinic and orthorhombic form of the MFI framework [34, 35].

The shape of the hysteresis above p/p_0 = 0.45 for ZSM-5/Ru/S-1 together with the shape of the isotherm points to a well crystalline shell composed of small MFI crystals. For the Ru/S-1, the high relative pressure hysteresis is missing, and in the Ru/nonetched S-1, it is significantly smaller resulting from interparticle adsorption in Ru agglomerates. The BJH pore size distribution curves are shown in Figure S7, SI. The BJH curves clearly illustrate the formation of mesopores upon fluoride etching and reconstruction of the material upon overgrowing. The presence of mesoporosity in S-1 crystallized on the surface of the parent crystals (S1−Ru-ZSM-5) also observed by SEM is possibly due to very fast crystallization so that the voids inside the crystals were not fully reconstructed. The peak at 3.7 nm present in the BJH curves of all samples is an artifact caused by breaking of meniscus of the liquid nitrogen at p/p_0 = 0.43.

In summary, the prepared Ru-MFI composite catalysts are composed of Ru nanoparticles of 3−20 nm (depending on preparation procedure), which are present on the surface of nonetched parent zeolite (Ru/nonetched S-1 and Ru/nonetchedZSM-5) or in the mesopores created by the ammonium fluoride etching (Ru/S-1 and Ru/ZSM-5). These zeolites can be covered by a layer, which is composed of small secondary ZSM-5 or S-1 crystals formed during coating either with a ZSM-5 or a S-1 shell (four catalysts having a zeolite shell). The present set of catalysts enables to study the influence of the Ru location and influence of the acidic character of the parent (core) zeolite and coating shell on the catalytic performance in the hydrocarbon synthesis from syngas.

4.2.3 Catalytic Performance in FT Synthesis

The results of the FT catalytic evaluation of the materials are shown in Table 4.2, Figure 4.7, Table S1 and Figures S8−S10, SI. The reaction results in the production of hydrocarbons and water. Mostly C_1−C_{12} hydrocarbons were produced for metal-ZSM-5 catalysts. Only negligible amounts of carbon dioxide were detected. The dependence of carbon monoxide conversion over the studied catalysts as a function of time on stream is displayed in Figure S8, SI. No visible deactivation was observed for all catalysts. This also suggests that no significant metal sintering or carbon deposition occur over the studied catalysts.

The catalytic performance is a function of ruthenium content in the samples; higher Ru content leads to high FT reaction rate (Figure S9, SI). Interestingly, the FT reaction rate does not correlate with the catalyst Brönsted acidity. The catalytic performance was also compared using ruthenium time-yield (RuTY), which was calculated as FT reaction rate normalized by the amount of Ru atoms in the catalyst. Figure 4.7 shows that etching of either silicalite-1 or ZSM-5 results in a significant increase in the RuTY (e.g., S-1:123.10^{-6} s^{-1} vs 212.10^{-6} s^{-1}). Etching generates a complementary mesoporous structure in the zeolite support, where the Ru nanoparticles are subsequently deposited. Higher FT reaction rate over the etched catalysts can be, therefore, explained by the better dispersion of Ru nanoparticles over external surface and mesopores of zeolite. Ru deposited on the etched support showed lower sintering ability during the catalyst calcination and reduction even in cases when it is not coated.

Table 4.2. Catalytic performance data of metal-zeolite composite catalysts. Conditions: GHSV = 6500 $cm^3/g \cdot h$, $H_2/CO = 2$, P = 20 bar, T = 250 °C.

Catalyst Shell/Me/Core	**Ru wt. %**	**X_{CO}, %**	**R_{CO}, mol/g s**	**S_{CH4}, %**	**S_{C1-C12}, %**	**S_{C5-C12}, %**	**S_{C5+}, %**	**C_5-C_{12} iso/para ratio**
Ru/ nonetched S-1	5.9	9.0	7.25	4.2	36.8	22.7	85.9	1.6
Ru/S-1	11.2	29.5	23.79	12.0	51.7	29.9	78.2	1.8
Ru/non-etched ZSM-5	8.4	30.0	24.20	10.7	69.8	46.1	76.3	2.7
Ru/ZSM-5	10.9	49.1	39.60	12.1	88.8	62.2	73.4	3.2
S-1/Ru/S-1	4.7	8.0	6.45	10.0	47.6	26.6	79.0	1.9
S-1/Ru/ZSM-5	5.9	23.2	18.71	12.4	61.5	36.8	75.3	1.9
ZSM-5/Ru/S-1	6.7	20.9	16.85	11.5	78.3	50.6	72.3	3.4
ZSM-5/Ru/ZSM-5	7.8	36.8	29.68	11.7	87.2	60.6	73.4	3.5

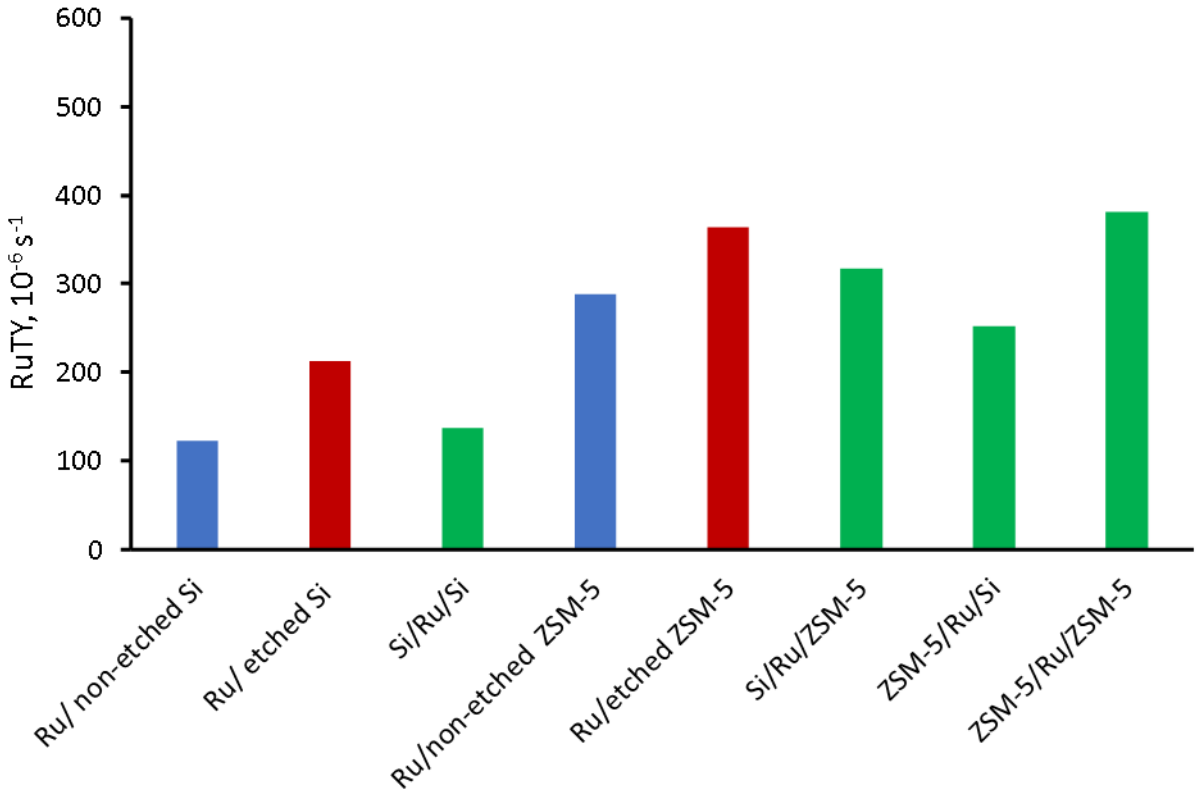

Figure 4.7. RuTY for ruthenium zeolite nanocomposite catalysts.

The selectivity of FT synthesis over Ru zeolite composite catalysts depends on both porosity, concentration and localization of acid sites within the catalyst. The Ru catalysts supported on S-1 (Ru/nonetched S-1, Ru/S-1, S-1/Ru/S-1) showed the highest selectivity to the C_{5+} hydrocarbons (85.9%, 78.2% and 79%, respectively) and lowest ratio of iso- to normal hydrocarbons among all the studied samples (1.6, 1.8, 1.9, respectively, Table 4.2). At the same time, the silicalite-1 etching and coating of the etched sample with a silicalite-1 layer (S-1/Ru/S-1) result in higher selectivity to methane and lighter hydrocarbons, some decrease in the C_{5+} selectivity and higher CO conversion in comparison with Ru/non etched S-1. The effect can be again due to the localization of smaller Ru nanoparticles within the mesopores in Ru/S-1. In addition, the S-1/Ru/S-1 provided lower CO conversion in

comparison with Ru/S-1 not only because of lower Ru content (Ru/S-1 11.2 wt % vs S-1/Ru/S-1 4.7 wt % = ratio 2.4:1) but also because of creating additional diffusional limitation due the catalyst coating with silicalite-1 layer in the S-1/Ru/S-1 sample (CO conversion 29.6% vs 8% = ratio 3.7:1). These results are consistent with previous reports [8, 36, 37]. The hydrocarbon distribution curves for coated S-1/Ru/S1, S-1/Ru/ZSM-5, ZSM/Ru/S-1, and ZSM-5/Ru/ZSM-5 catalyst are displayed in Figure S10, SI. They also clearly show a high fraction of isoparaffins in the catalysts containing ZSM-5 in the shell (ZSM-5/Ru/S-1 and ZSM-5/Ru/ZSM-5).

The Ru catalysts supported on both nonetched and etched ZSM-5 zeolite exhibit higher selectivity to shorter hydrocarbons in comparison with their S-1 based counterparts (e.g., $S_{C5–C12}$ over Ru/S-1 29.9% vs Ru/ZSM-5 62.2%) and at the same time higher ratio of iso- to normal hydrocarbons in the C_5−C_{12} hydrocarbons range is observed for these pairs (e.g., Ru/S-1 1.8 vs Ru/ZSM-5 3.2, Table 4.2). The observed phenomena are due to the isomerization and cracking of the hydrocarbons, produced during FT synthesis, over the ZSM-5 zeolite acid sites.

Interesting results are observed for the Ru-zeolite catalysts coated with a layer of silicalite-1 or ZSM-5 zeolite. Coating of ZSM-5 zeolites containing Ru nanoparticles with silicalite-1 (S-1/Ru/ZSM-5) results in the selectivity patterns similar to that observed over the silicalite-1 based samples such as Ru/S-1, Ru/nonetched S-1, or S-1/Ru/S-1 catalysts. This suggests that the presence of the silicalite-1 shell on the top of any of the Ru zeolite catalysts significantly reduces the isomerization activity. Coating with silicalite results in the decrease in the concentration of the Brønsted acid sites in the proximity to Ru nanoparticles and thus results in lower selectivity to isoparaffins.

Somewhat different results were obtained over the catalysts containing the shell constituted by the ZSM-5 zeolite (regardless the core). Both ZSM-5/Ru/ZSM-5 and ZSM-5/Ru/S-1 catalysts exhibited rather similar selectivity to methane (S_{CH4} = 11.5%), to C_5 and longer hydrocarbons (S_{C5+} = 72.3%) and iso/n ratio (3.4), and together with Ru/ZSM-5 without shell, they provided the highest selectivity for the gasoline hydrocarbons of all the investigated catalysts ($S_{C5–C12}$ 60.6%, 50.6% and 62.2%, respectively). Thus, the catalysts which contain the ZSM-5 zeolite in the shell, showed the highest isomerization activity and respectively highest ratio of the iso- to normal hydrocarbons. This is indicative of the important and probably determining role of the acid sites located in the shell on the selectivity patterns.

The catalytic data were also measured at higher temperature (270 °C, Table S1, SI). They show slightly lower selectivity to C_{5+} hydrocarbons and further increase in the ratio of iso- to normal paraffins over the catalysts containing the acid ZSM-5 zeolite in the catalyst shell.

4.2.4 Roles of Core, Shell, and Porosity in the Ru-Zeolite Nanocomposite Catalysts in the Synthesis of Iso-Paraffins from Syngas

Our results indicate that the zeolite mesoporosity has an essential influence on the performance of ruthenium zeolite composite catalysts. The most noticeable effect is higher FT reaction rate observed at the same Ru content over the mesoporous samples (Figure 4.7). In agreement with previous reports, the presence of mesopores facilitates diffusion of carbon monoxide and hydrocarbons within the catalyst pellets [13, 18]. The presence of mesopores reduces the effective H_2/CO ratio in the proximity to the active sites and lowers methane

selectivity. Note that synthesis of iso-paraffins from syngas over Ru zeolite composite catalysts involves both metal and acid sites. First, the metal sites are required for CO hydrogenation to hydrocarbons via FT reaction. FT reaction involves adsorption and dissociation of carbon monoxide and hydrogen on the metal sites followed by surface polymerization of adsorbed CH_x fragments, their hydrogenation, and desorption [1, 18]. FT synthesis results in the production of mostly linear hydrocarbons. Formation of iso-paraffins under FT reaction conditions demands hydrocarbon isomerization. Isomerization of paraffins on zeolite in the absence of metals requires high temperatures and often coincides with major cracking. It is not likely, therefore, that paraffin isomerization solely catalyzed by zeolite acid sites may occur under the conditions of FT synthesis. Taking into account the temperatures typically used for low temperature FT synthesis (190−240 °C), the hydrocarbon isomerization under these conditions should also involve metal sites. Thus, the role of ruthenium metal sites could also be related to dehydrogenation of FT hydrocarbons providing olefins for isomerization. In this case, olefin isomerization occur on the acid sites associated with the zeolite. Both paraffins and olefins are the primary products of FT synthesis over Ru catalysts. While olefin isomerization does not require metal sites, paraffin isomerization takes place on both metal and acid sites. It can be favored therefore by their proximity.

The catalysts in this paper were prepared by insertion of Ru nanoparticles on and into ZSM-5 or silicalite-1 zeolites. The inserted nanoparticles are preferentially located on the outer surface of the zeolite particles. Generation of additional mesoporosity by etching results in partial encapsulation of these nanoparticles and their localization in the mesopores in the subsurface layer of the zeolite. Subsequent coating (overgrowing) introduces the silicalite-1 or ZSM-5 zeolite shell in direct interaction with Ru nanoparticles. Our characterization

results are indicative of the stability of Ru/ZSM-5 and Ru/S-1 during the coating process. Indeed, the textural properties of the zeolite (apparent surface area, microporous volume) are only slightly affected by the coating (Table 4.1, Figures 4.5 and 4.6). The XRD patterns of ZSM-5 and S-1 remain unchanged after the coating (see Figure 4.2).

The catalytic results suggest that in the coated samples, ruthenium nanoparticles interact more strongly with the coating materials (silicalite-1 or ZSM-5) than with the catalyst core. In addition, any formed hydrocarbons are forced to pass through the layer of zeolite phase, where they undergo isomerization/cracking. This explains the observed determining effect of the catalyst shell on the reaction selectivity. The isomerization activity of the catalyst is much more significantly affected by the shell of the composite catalysts than by the core. The isomerization of olefins takes place mostly in the very close proximity of the ruthenium nanoparticles, which are preferentially localized on the outer surface of the core crystals or in the subsurface layer (in the case of etched samples).

Our results suggest that the presence of Brønsted acid sites in the proximity to ruthenium nanoparticles is indispensable in order to attain a higher ratio of olefin to paraffins. A higher concentration of Brønsted acid sites in the proximity of ruthenium nanoparticles can be attained by creating core−shell structure with the shell formed by ZSM-5 zeolite. The presence of Brønsted acid sites in this shell is extremely important for higher selectivity to iso-paraffins. This shell is even more important than the catalyst core. For example, the catalysts, which are composed of silica core (without acid sites) and zeolite shell formed by ZSM-5 zeolite, have shown good performance in the synthesis of iso-paraffins from syngas. The conclusion about the inference of the shell and its acidity on the reaction selectivity has a fundamental significance for the design of bifunctional catalysts.

4.2.5 Strategy for the Synthesis of Highly Dispersed Ru Catalysts

The analysis of the catalytic activity of the Ru catalysts after coating of the shell leads to an increase of the activity of Ru in the catalyst (Figure 4.7). The presence of the shell should increase the transport limitations and the activity should be lower in comparison with the parent catalyst. The possible explanation of this effect could be related to the partial decomposition of Ru nanoparticles during crystallization of the shell (Figure 4.8).

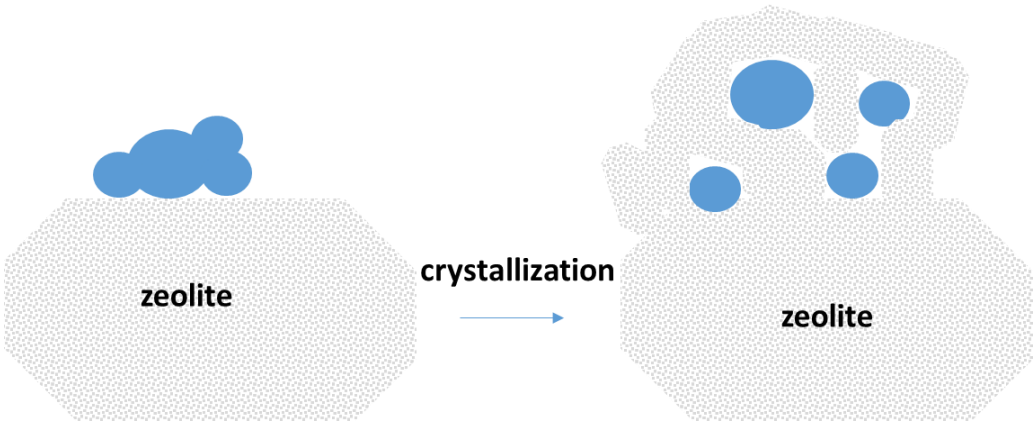

Figure 4.8. Scheme of the decomposition of Ru supported over zeolite during recrystallization.

Four ruthenium zeolite composite catalysts were prepared, i. e. Ru/ZSM-5-ME, ZSM-5/Ru/ZSM-5-ME, Ru/ZSM-5 and ZSM-5/Ru/ZSM-5. The suffix ME indicates that the sample was prepared by microemulsion. Ru nanoparticles created by micro-emulsion system were inserted into the parent zeolite and subsequently, the zeolite was overgrowing to trap the nanoparticles inside the zeolite phase. In addition, impregnation of Ru over zeolite was carried out without microemulsion, and submitted to overgrowing.

The crystallinity of the catalysts was evaluated by XRD, as shown in Figure 4.9. All the samples presented the diffraction peaks of ZSM-5 (7.8º, 8.7º, 22.94º, 23.6º, 24.26º, 45º).

The detected diffraction peaks match well with the characteristic peaks of RuO_2 [8]. The size of RuO_2 nanoparticles were evaluated by the Scherer equation [9]. The size of metal nanoparticles in the catalyst Ru/ZSM-5 is in the range 10-50 nm according to TEM analysis (Figure 4.10). XRD analysis of calcined Ru/ZSM-5 catalyst demonstrates the presence of the patterns of RuO_2 and ZSM-5 (Figure 4.9). The average size of RuO_2 nanoparticles according to Scherrer equation is equal to 15 nm and correlates with TEM analysis. Ru/ZSM-5-ME contains significantly larger Ru nanoparticles with sizes in the range 10-100 nm, which can be observed by a sharp peak in XRD patterns. The size of the RuO_2 nanoparticles was 15.3 nm for Ru/ZSM-5, 10.8 nm for the encapsulated ZSM-5/Ru/ZSM-5, 47.2 nm for Ru/ZSM-5-ME and 15.2 nm for the encapsulated ZSM-5/Ru/ZSM-5-ME (Table 4.3). Note that larger sizes of nanoparticles were observed in the samples prepared by microemulsion. However, this fact did not imply the reduction of surface areas and total pore volume compared with the catalysts prepared by conventional impregnation. This may be due to a higher dispersion of the metallic particles prepared by microemulsion on the zeolite, what is confirmed by TEM images of the encapsulated Ru/ZSM-5-ME (Figure 4.10).

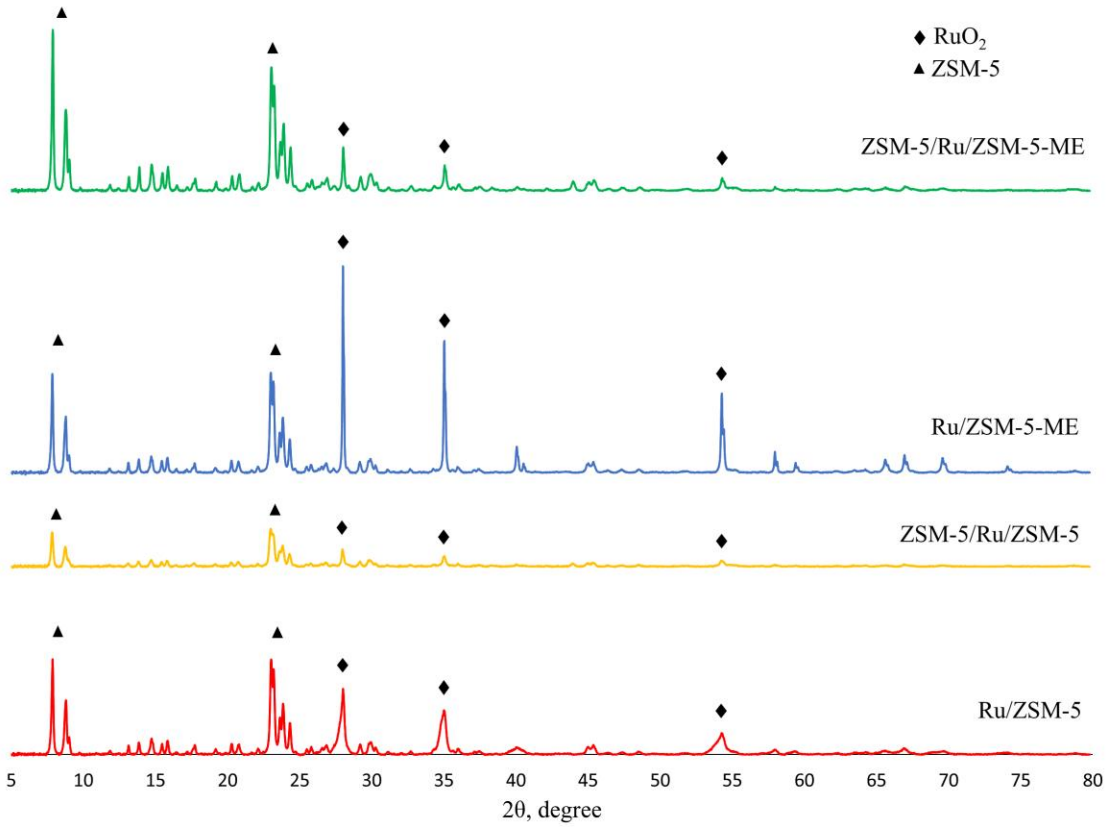

Figure 4.9. XRD patterns of ruthenium catalysts.

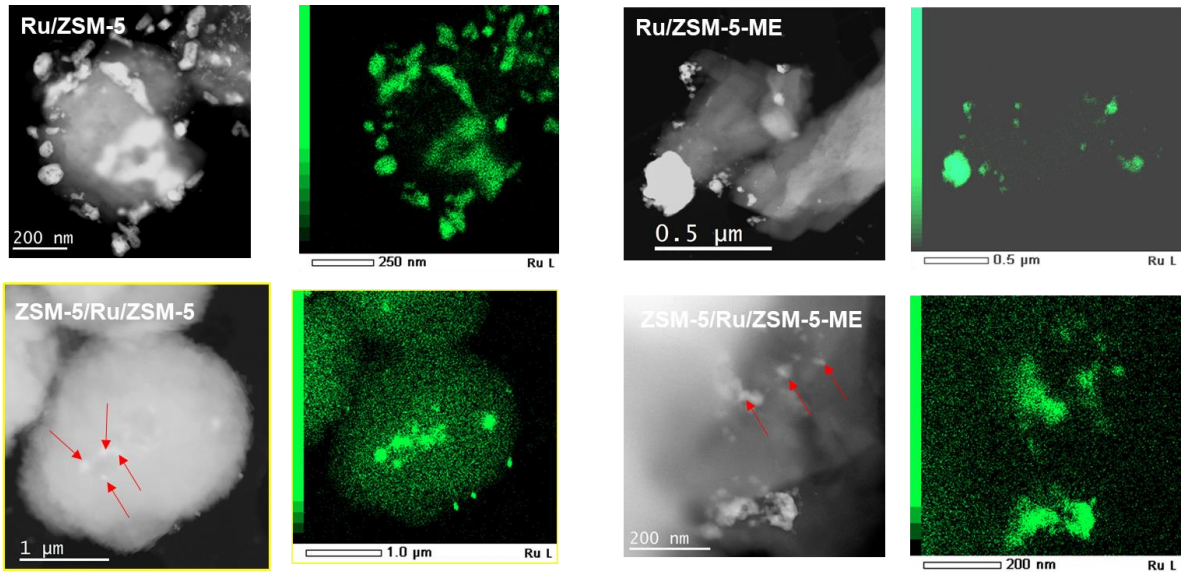

Figure 4.10. STEM-HAADF and TEM-EDX analysis for prepared Ru/ZSM-5 and Ru/ZSM-5-ME before and after re-crystallization.

Table 4.3. Textural properties.

Sample	N_2 Adsorption				Particle size (nm)	Metal content (wt.%)	SiO_2/ Al_2O_3
	S_{BET} (m^2g^{-1})	Vtotal (cm^3g^{-1})	Vmic (cm^3g^{-1})	Vmeso (cm^3g^{-1})			
Ru-ZSM-5	389	0.20	0.12	0.08	15.3	2.2	20.8
ZSM-5/Ru/ZSM-5	202	0.09	0.07	0.02	10.8	1.6	30.9
Ru/ZSM-5-ME	384	0.20	0.12	0.08	47.2	1.7	20.7
ZSM-5/Ru/ZSM-5-ME	368	0.16	0.13	0.04	15.2	1.3	29.2

The ZSM-5 samples with Ru display a Type-I isotherm, which exhibits a sharp uptake at low relative pressure followed by plateau with a hardly visible hysteresis at $P/P_0>0.5$ (Figure 4.11). The samples show similar BET surface area and N_2 adsorption. TPR analysis of Ru/ZSM-5-ME catalysts after calcination demonstrates intensive peak at 175 ^oC with a shoulder at 150 ^oC (Figure 4.11). The sample containing smaller Ru nanoparticles in Ru/ZSM-5 demonstrates an additional peak at 130 ^oC, which can be assigned to the reduction of small size RuO_2 species.

Crystallization of ZSM-5 in the presence of Ru/ZSM-5 samples leads to additional growth of ZSM-5 which can be confirmed by a decrease of the Ru content in the catalyst (Table 4.3). STEM-HAADF analysis demonstrates encapsulation of Ru nanoparticles inside of ZSM-5 crystals, which can be explained by the growth of ZSM-5 over the crystals (Figure 4.10). It can be observed that besides encapsulation of Ru inside of zeolite, the nanoparticles decompose in smaller nanoparticles close to each other. This effect is observed for small-size nanoparticles in Ru/ZSM-5 and large nanoparticles prepared by microemulsion technique in Ru/ZSM-5-ME.

Analysis of XRD patterns of the prepared samples demonstrates significant broadening of the peaks related to RuO_2 which confirms a decrease in the size of Ru nanoparticles. According to Scherrer size of nanoparticles significantly decreases from 15 to 10 nm for Ru/ZSM-5 and from 47 to 15 nm for Ru/ZSM-5-ME. Low temperature N_2 adsorption demonstrates a significant decrease of N_2 adsorption after zeolite crystallization in ZSM-5/Ru/ZSM-5 to 202 m^2/g, which can be explained by blocking access to zeolite pores by small size Ru nanoparticles. A less significant decrease of N_2 adsorption is also observed over for ZSM-5/Ru/ZSM-5-ME.

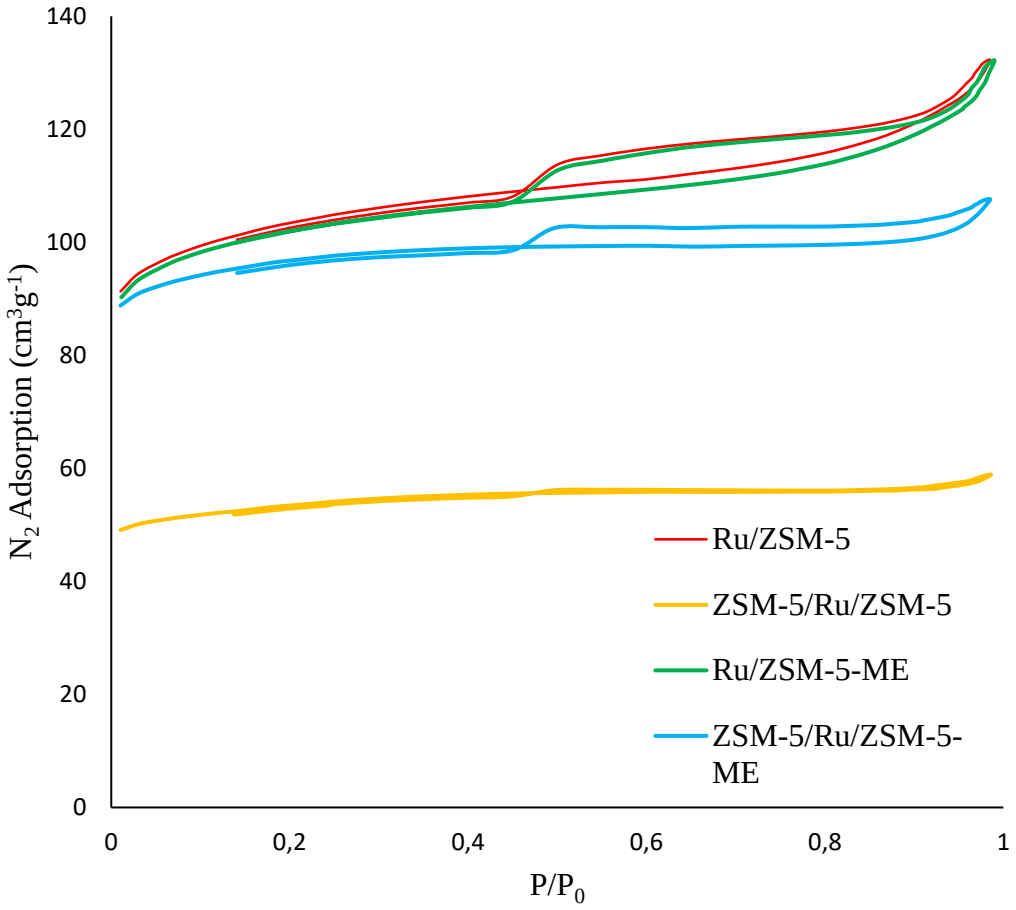

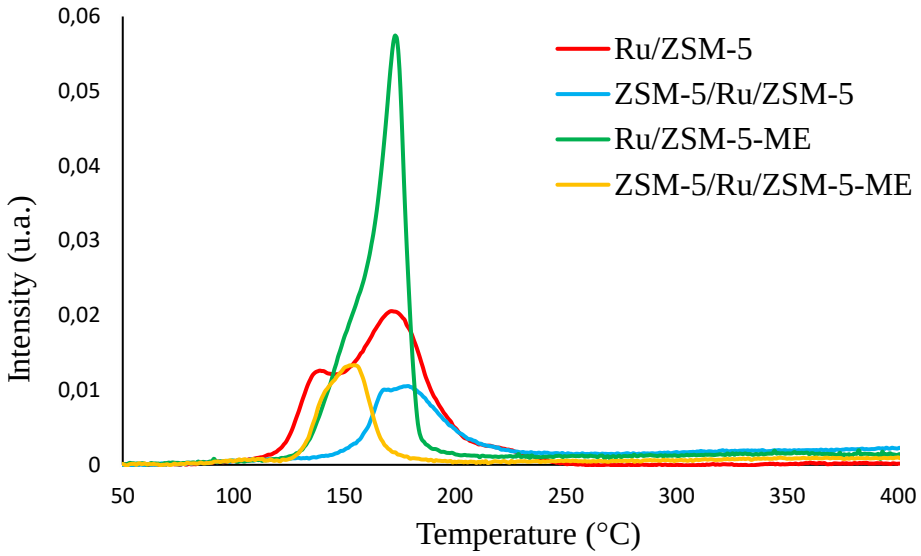

Figure 4.11. Low temperature N_2 adsorption (a) and TPR H_2 (b) of the catalysts before and after crystallization.

TPR analysis demonstrates significant changes after catalyst recrystallization. The intensity of Ru reduction peak in ZSM-5/Ru/ZSM-5 and ZSM-5/Ru/ZSM-5-ME significantly decreases due to the lower metal content after zeolite growth (Figure 11). ZSM-5/Ru/ZSM-5 demonstrates only high-temperature reduction peak at 175 ^{o}C in comparison with the parent catalyst which can be explained by the presence of highly dispersed Ru nanoparticles.

4.3 Conclusions

Ruthenium-zeolite composite catalysts for FT reaction have been prepared and studied with the aim to encapsulate the metallic nanoparticles inside the zeolite matrix to provide high “intimacy” between the metallic and acid active sites of the catalyst.

Efficient encapsulation of ruthenium nanoparticles within the zeolite crystals was successfully achieved by coating the ZSM-5 and silicalite-1 carriers containing Ru nanoparticles with a shell MFI-type material. The synthesis procedure involves three steps: (i) creation of mesopores in the parent zeolite by etching with ammonium fluoride, (ii) synthesis of ruthenium nanoparticles and their deposition over parent nonetched or etched zeolites, (iii) zeolite overgrowing (coating) of the Ru-zeolite catalysts. In these composite materials, ruthenium nanoparticles are covered a thin layer of a zeolite shell.

The catalytic performance of the synthesized materials primarily depends on the ruthenium content, the presence of secondary mesopores, and the composition and acidity of the catalyst shell. The reaction rates increase with higher Ru content. The diffusion limitations in the composite catalysts are reduced by using mesoporous ZSM-5 or silicalite-1 as core. Significantly increased relative amount of produced isoparaffins (with respect to n-paraffins) was observed over the catalysts containing the ZSM-5 zeolite in the shell. Isomerization of hydrocarbons produced via FT synthesis requires the presence of both metal and acid sites. The proximity between these sites in the zeolite shell is a crucial parameter for the design of efficient metal zeolite bifunctional catalysts for selective synthesis of gasoline type fuels via FT synthesis. The acidity of the catalyst core has only a limited impact on the catalytic performance.

The investigation of the size of Ru nanoparticles after shell crystallization indicates the increase of the dispersion of Ru in the catalyst. The effect could be related to decomposition of Ru metal oxide nanoparticles during crystallization of ZSM-5. The mechanism of the decomposition requires additional investigation.

4.4 References

[1] Khodakov, A. Y.; Chu, W.; Fongarland, P. Advances in the Development of Novel Cobalt Fischer−Tropsch Catalysts for Synthesis of Long-Chain Hydrocarbons and Clean Fuels. Chem. Rev. 2007, 107, 1692−1744.

[2] Zhou, W.; Cheng, K.; Kang, J.; Zhou, C.; Subramanian, V.; Zhang, Q.; Wang, Y. New Horizon in C1 Chemistry: Breaking the Selectivity Limitation in Transformation of Syngas and Hydrogenation of CO_2 into Hydrocarbon Chemicals and Fuels. Chem. Soc. Rev. 2019, 48, 3193−3228.

[3] Komvokis, V. G.; Karakoulia, S.; Iliopoulou, E. F.; Papapetrou, M. C.; Vasalos, I. A.; Lappas, A. A.; Triantafyllidis, K. S. Upgrading of Fischer−Tropsch Synthesis Bio-Waxes via Catalytic Cracking: Effect of Acidity, Porosity and Metal Modification of Zeolitic and Mesoporous Aluminosilicate Catalysts. Catal. Today 2012, 196, 42−55.

[4] Li, J.; He, Y.; Tan, L.; Zhang, P.; Peng, X.; Oruganti, A.; Yang, G.; Abe, H.; Wang, Y.; Tsubaki, N. Integrated Tuneable Synthesis of Liquid Fuels via Fischer−Tropsch Technology. Nat. Catal. 2018, 1, 787−793.

[5] Zhang, Q.; Kang, J.; Wang, Y. Development of Novel Catalysts for Fischer−Tropsch Synthesis: Tuning the Product Selectivity. ChemCatChem 2010, 2, 1030−1058.

[6] Weisz, P. B. Polyfunctional Heterogeneous Catalysis. Adv. Catal. 1962, 13, 137−190.

[7] Martínez, A.; Valencia, S.; Murciano, R.; Cerqueira, H. S.; Costa, A. F.; S.-Aguiar, E. F. Catalytic Behavior of Hybrid Co/SiO_2- (Medium-Pore) Zeolite Catalysts during the One-Stage Conversion of Syngas to Gasoline. Appl. Catal., A 2008, 346, 117−125.

[8] Cheng, K.; Kang, J.; Huang, S.; You, Z.; Zhang, Q.; Ding, J.; Hua, W.; Lou, Y.; Deng, W.; Wang, Y. Mesoporous Beta Zeolite- Supported Ruthenium Nanoparticles for Selective Conversion of Synthesis Gas to C_5−C_{11} Isoparaffins. ACS Catal. 2012, 2, 441−449.

[9] Sartipi, S.; Makkee, M.; Kapteijn, F.; Gascon, J. Catalysis Engineering of Bifunctional Solids for the One-Step Synthesis of Liquid Fuels from Syngas: A Review. Catal. Sci. Technol. 2014, 4, 893−907.

[10] Sartipi, S.; Van Dijk, J. E.; Gascon, J.; Kapteijn, F. Toward Bifunctional Catalysts for the Direct Conversion of Syngas to Gasoline Range Hydrocarbons: H-ZSM-5 Coated Co versus HZSM-5 Supported Co. Appl. Catal., A 2013, 456, 11−22.

[11] Martínez-Vargas, D. X.; Sandoval-Rangel, L.; Campuzano-Calderon, O.; Romero-Flores, M.; Lozano, F. J.; Nigam, K. D. P.; Mendoza, A.; Montesinos-Castellanos, A. Recent Advances in Bifunctional Catalysts for the Fischer−Tropsch Process: One-Stage Production of Liquid Hydrocarbons from Syngas. Ind. Eng. Chem. Res. 2019, 58, 15872−15901.

[12] Flores, C.; Batalha, N.; Marcilio, N. R.; Ordomsky, V. V.; Khodakov, A. Y. Influence of Impregnation and Ion Exchange Sequence on Metal Localization, Acidity and Catalytic Performance of Cobalt BEA Zeolite Catalysts in Fischer−Tropsch Synthesis. ChemCatChem 2019, 11, 568−574.

[13] Kim, J.-C.; Lee, S.; Cho, K.; Na, K.; Lee, C.; Ryoo, R. Mesoporous MFI Zeolite Nanosponge Supporting Cobalt Nanoparticles as a Fischer−Tropsch Catalyst with High Yield of Branched Hydrocarbons in the Gasoline Range. ACS Catal. 2014, 4, 3919−3927.

[14] Fraenkel, D.; Gates, B. C. Shape-Selective Fischer−Tropsch Synthesis Catalyzed by Zeolite-Entrapped Cobalt Clusters. J. Am. Chem. Soc. 1980, 102, 2478−2480.

[15] Bao, J.; He, J.; Zhang, Y.; Yoneyama, Y.; Tsubaki, N. A Core/Shell Catalyst Produces a Spatially Confined Effect and Shape Selectivity in a Consecutive Reaction. Angew. Chem., Int. Ed. 2008, 47, 353−356.

[16] Subramanian, V.; Zholobenko, V. L.; Cheng, K.; Lancelot, C.; Heyte, S.; Thuriot, J.; Paul, S.; Ordomsky, V. V.; Khodakov, A. Y. The Role of Steric Effects and Acidity in the Direct Synthesis of Iso-Paraffins from Syngas on Cobalt Zeolite Catalysts. ChemCatChem 2016, 8, 380−389.

[17] Carvalho, A.; Marinova, M.; Batalha, N.; Marcilio, N. R.; Khodakov, A. Y.; Ordomsky, V. V. Design of Nanocomposites with Cobalt Encapsulated in the Zeolite Micropores for Selective Synthesis of Isoparaffins in Fischer−Tropsch Reaction. Catal. Sci. Technol. 2017, 7, 5019−5027.

[18] Iglesia, E.; Reyes, S. C.; Madon, R. J.; Soled, S. L. Selectivity Control and Catalyst Design in the Fischer−Tropsch Synthesis: Sites, Pellets, and Reactors. Adv. Catal. 1993, 39, 221−302.

[19] He, J.; Liu, Z.; Yoneyama, Y.; Nishiyama, N.; Tsubaki, N. Multiple-Functional Capsule Catalysts: A Tailor-Made Confined Reaction Environment for the Direct Synthesis of Middle Isoparaffins from Syngas. Chem. - Eur. J. 2006, 12, 8296−8304.

[20] He, J.; Yoneyama, Y.; Xu, B.; Nishiyama, N.; Tsubaki, N. Designing a Capsule Catalyst and Its Application for Direct Synthesis of Middle Isoparaffins. Langmuir 2005, 21, 1699−1702.

[21] Zhu, C.; Bollas, G. M. Gasoline Selective Fischer−Tropsch Synthesis in Structured Bifunctional Catalysts. Appl. Catal., B 2018, 235, 92−102.

[22] Liu, J.-Y.; Chen, J.-F.; Zhang, Y. Cobalt-Imbedded Zeolite Catalyst for Direct Syntheses of Gasoline via Fischer−Tropsch Synthesis. Catal. Sci. Technol. 2013, 3, 2559−2564.

[23] Mazonde, B.; Cheng, S.; Zhang, G.; Javed, M.; Gao, W.; Zhang, Y.; Tao, M.; Lu, C.; Xing, C. A Solvent-Free: In Situ Synthesis of a Hierarchical Co-Based Zeolite Catalyst and Its Application to Tuning Fischer−Tropsch Product Selectivity. Catal. Sci. Technol. 2018, 8, 2802−2808.

[24] Liu, J.; Wang, D.; Chen, J.-F.; Zhang, Y. Cobalt Nanoparticles Imbedded into Zeolite Crystals: A Tailor-Made Catalyst for One-Step Synthesis of Gasoline from Syngas. Int. J. Hydrogen Energy 2016, 41, 21965−21978.

[25] Cheng, S.; Mazonde, B.; Zhang, G.; Javed, M.; Dai, P.; Cao, Y.; Tu, S.; Wu, J.; Lu, C.; Xing, C.; et al. Co-Based MOR/ZSM-5 Composite Zeolites over a Solvent-Free Synthesis Strategy for Improving Gasoline Selectivity. Fuel 2018, 223, 354−359.

[26] Flores, C.; Batalha, N.; Ordomsky, V. V.; Zholobenko, V. L.; Baaziz, W.; Marcilio, N. R.; Khodakov, A. Y. Direct Production of Iso-Paraffins from Syngas over Hierarchical Cobalt-ZSM-5 Nanocomposites Synthetized by Using Carbon Nanotubes as Sacrificial Templates. ChemCatChem 2018, 10, 2291−2299.

[27] Flores, C.; Zholobenko, V. L.; Gu, B.; Batalha, N.; Valtchev, V.; Baaziz, W.; Ersen, O.; Marcilio, N. R.; Ordomsky, V. V.; Khodakov, A. Y. Versatile Roles of Metal Species in Carbon Nanotube Templates for the Synthesis of Metal−Zeolite Nanocomposite Catalysts. ACS Appl. Nano Mater. 2019, 2, 4507−4517.

[28] Qin, Z.; Melinte, G.; Gilson, J.-P.; Jaber, M.; Bozhilov, K.; Boullay, P.; Mintova, S.; Ersen, O.; Valtchev, V. The Mosaic Structure of Zeolite Crystals. Angew. Chem. 2016, 128, 15273−15276.

[29] Subramanian, V.; Cheng, K.; Lancelot, C.; Heyte, S.; Paul, S.; Moldovan, S.; Ersen, O.; Marinova, M.; Ordomsky, V. V.; Khodakov, A. Y. Nanoreactors: An Efficient Tool to Control the Chain-Length Distribution in Fischer−Tropsch Synthesis. ACS Catal. 2016, 6, 1785−1792.

[30] Lippens, B. Studies on Pore Systems in Catalysts V. The t Method. J. Catal. 1965, 4, 319−323.

[31] Ngoye, F.; Lakiss, L.; Qin, Z.; Laforge, S.; Canaff, C.; Tarighi, M.; Valtchev, V.; Thomas, K.; Vicente, A.; Gilson, J. P.; et al. Mitigating Coking during Methylcyclohexane Transformation on HZSM-5 Zeolites with Additional Porosity. J. Catal. 2014, 320, 118−126.

[32] Müller, U.; Unger, K. K. Sorption Studies on Large ZSM-5 Crystals: The Influence of Aluminium Content, The Type of Exchangeable Cations and the Temperature on Nitrogen Hysteresis Effects. Stud. Surf. Sci. Catal. 1988, 39, 101−108.

[33] Nakai, K.; Sonoda, J.; Yoshida, M.; Hakuman, M.; Naono, H. High Resolution Adsorption Isotherms of N2 and Ar for Nonporous Silicas and MFI Zeolites. Adsorption 2007, 13, 351−356.

[34] Parra, J. B.; Ania, C. O.; Dubbeldam, D.; Vlugt, T. J. H.; Castillo, J. M.; Merkling, P. J.; Calero, S. Unraveling the Argon Adsorption Processes in MFI-Type Zeolite. J. Phys. Chem. C 2008, 112, 9976−9979.

[35] Cychosz, K. A.; Guillet-Nicolas, R.; García-Martínez, J.; Thommes, M. Recent Advances in the Textural Characterization of Hierarchically Structured Nanoporous Materials. Chem. Soc. Rev. 2017, 46, 389−414.

[36] Kang, J.; Cheng, K.; Zhang, L.; Zhang, Q.; Ding, J.; Hua, W.; Lou, Y.; Zhai, Q.; Wang, Y. Mesoporous Zeolite-Supported Ruthenium Nanoparticles as Highly Selective Fischer−Tropsch Catalysts for the Production of C5-C11 Isoparaffins. Angew. Chem., Int. Ed. 2011, 50, 5200−5203.

[37] Zhang, Q.; Cheng, K.; Kang, J.; Deng, W.; Wang, Y. Fischer−Tropsch Catalysts for the Production of Hydrocarbon Fuels with High Selectivity. ChemSusChem 2014, 7, 1251−1264.

5. General Conclusions and Perspectives

The actual interest in FT synthesis has grown up in consequence of environmental demands, technological developments and changes in fossil energy reserves. This process is an alternative source environmentally-sound production of chemicals and fuels from biomass, coal and natural gas to supply the world energy demand, as petroleum reserves are depleting. Selectivity control and catalyst stability are among the most important challenges in FT synthesis.

The conducted research work in the frame of this thesis has provided new approaches for the design of bifunctional zeolites catalysts containing highly dispersed metal particles. These approaches involve (i) using hard templates for the introduction of Ru into different zeolites; (ii) using an intermediate synthesis of mesopores for encapsulation of metal nanoparticles and (ii) using zeolite recrystallization for redispersion of Ru nanoparticles inside ZSM-5 zeolite crystallites.

5.1 General Conclusion

In chapter 3 highly dispersed ruthenium metallic species in the hierarchical BEA zeolite were synthesized. Ruthenium is a noble metal; it has easier reducibility and does not tend to form inert and barely reducible aluminates and silicates compared to cobalt. The 12-member ring BEA zeolite has larger micropores (0.76×0.64 nm) compared to 10-membered ring ZSM-5 zeolite (dp~0.55 nm). In addition to mesoporosity, larger micropores of the BEA zeolite may facilitate the localization of metal nanoparticles within the zeolite and the diffusion of reacting molecules. Using both ruthenium and BEA zeolite may allow, therefore,

achieving all benefits of metal zeolite hierarchical nanocomposites prepared using metal-CNT as templates and producing much more active catalysts for FT synthesis. The synthesis of BEA and ZSM-5 zeolites in the presence of CNT containing ruthenium generates a complementary mesoporous structure and results in the nanocomposites built of ruthenium nanoparticles and hierarchical zeolites. In the BEA zeolite prepared by both impregnation and synthesis in the presence of metal-CNT templates, a major fraction of metals species is located inside zeolite micropores. Ruthenium species exhibit much easier reducibility compared to cobalt, when introduced to the BEA and ZSM-5 zeolite with metal-CNT secondary templates. In Co/BEA, a significant amount of barely reducible cobalt silicate inactive in FT synthesis was observed, when cobalt was added with CNT to the BEA zeolite synthesis. The FT reaction rates were twice higher over the catalysts prepared using ruthenium CNT as secondary templates compared to the Ru zeolite catalyst prepared by impregnation or to cobalt counterparts. The synthesis of hierarchical zeolites using ruthenium CNT hard template leads to a uniform distribution of metal nanoparticles within the zeolite mesoporous structure, facilitates the diffusion and strongly enhances the catalytic performance in FT reaction.

Chapter 4 a new strategy for the synthesis of efficient metal zeolite bifunctional catalysts for the direct synthesis of branched gasoline-type hydrocarbons from syngas was proposed. This strategy addresses nanocasting of preformed ruthenium metallic nanoparticles in a secondary pore system of a mesoporous zeolite. The metal nanoparticles located in the mesopores of the zeolite are then entirely encapsulated by secondary grown zeolite structure. The nanoparticles are stabilized in the encapsulated systems, thus suppressing the particle migration and sintering. The proximity between metal and zeolite active sites provides an

unraveled synergy between the two types of the sites in the catalyst. The zeolite performance in hydrocarbon isomerization is mostly affected by the composition of the zeolite shell. Efficient encapsulation of ruthenium nanoparticles within the zeolite crystals was successfully achieved by coating the ZSM-5 and silicalite-1 carriers containing Ru nanoparticles with a shell MFI-type material. Isomerization of hydrocarbons produced via FT synthesis requires the presence of both metal and acid sites. The proximity between these sites in the zeolite shell is a crucial parameter for the design of efficient metal zeolite bifunctional catalysts for selective synthesis of gasoline-type fuels via FT synthesis. The acidity of the catalyst core has only a limited impact on the catalytic performance.

We also discovered that re-crystallization process for shell synthesis results in encapsulation of Ru nanoparticles inside of ZSM-5 crystal with a decrease of the sizes of nanoparticles from 50-100 nm to 5 - 10 nm. This process could be used for the increase of the dispersion of noble metals in the catalyst.

5.2 Perspectives

Although we have synthesized a lot of metal-zeolite bifunctional catalysts using different strategies there are still a lot of problems that have to be solved:

1. It would be possible to prepare more structured metal-zeolite catalysts using different types of sacrificial templates besides metal-CNT such as polymers, salts… for higher distribution of the metal through the zeolite with spatial intimate metal-acid active sites for a broad range of catalytic reactions such as hydrogenation-etherification, hydrogenation-deoxygenation etc.

2. It is still hard to achieve localization of the metal nanoparticles in the mesopores by the engineering of core-shell catalyst. The increase of the affinity of the nanoparticles to the pores could be achieved by a coating of the nanoparticles by organic ligands attaching to the active sites in the mesopores. It would provide significantly more selective localization of the nanoparticles in the mesopores.
3. The decomposition of Ru nanoparticles during zeolite crystallization requires further investigation of the mechanism using model Ru surface and zeolite crystallization procedure. The identification of the mechanism could help in the development of the procedure of increase of the dispersion of noble metal catalysts which would be highly desirable in catalysis.